2011

Design and Operation of Stationary Distributed Battery Micro-storage Systems

Ala R. Al-Haj Hussein
University of Central Florida

DESIGN AND OPERATION OF STATIONARY DISTRIBUTED BATTERY MICRO-STORAGE SYSTEMS

By

ALA R. AL-HAJ HUSSEIN
B.S. Jordan University of Science and Technology, 2005
M.S. University of Central Florida, 2008

A dissertation submitted in partial fulfillment of the requirements
for the degree of Doctor of Philosophy
in the Department of Electrical Engineering and Computer Science
in the College of Engineering and Computer Science
at the University of Central Florida
Orlando, Florida

Summer Term
2011

Major Professor: Issa Batarseh

ABSTRACT

Due to some technical and environmental constraints, expanding the current electric power generation and transmission system is being challenged by even increasing the deployment of distributed renewable generation and storage systems. Energy storage can be used to store energy from utility during low-demand (off-peak) hours and deliver this energy back to the utility during high-demand (on-peak) hours. Furthermore, energy storage can be used with renewable sources to overcome some of their limitations such as their strong dependence on the weather conditions, which cannot be perfectly predicted, and their unmatched or out-of-synchronization generation peaks with the demand peaks. Generally, energy storage enhances the performance of distributed renewable sources and increases the efficiency of the entire power system. Moreover, energy storage allows for leveling the load, shaving peak demands, and furthermore, transacting power with the utility grid.

This research proposes an energy management system (EMS) to manage the operation of distributed grid-tied battery micro-storage systems for stationary applications when operated with and without renewable sources. The term “micro” refers to the capacity of the energy storage compared to the grid capacity. The proposed management system employs four dynamic models; economic model, battery model, and load and weather forecasting models. These models, which are the main contribution of this research, are used in order to optimally control the operation of the micro-storage system (MSS) to maximize the economic return for the end-user when operated in an electricity spot market system.

Chapter 1 presents an introduction to the drawbacks of the current power system, the role of energy storage in deregulated electricity markets, limitations of renewable sources, ways for participating in spot electricity markets, and an outline of the main contributions in this dissertation. In Chapter 2, some hardware design considerations for distributed micro-storage systems as well as some economic analyses are presented. Chapters 3 and 4 propose a battery management system (BMS) that handles three main functions: battery charging, state-of-charge (SOC) estimation and state-of-health (SOH) estimation. Chapter 5 proposes load and weather forecasting models using artificial neural networks (ANNs) to develop an energy management strategy to control the operation of the MSS in a spot market system when incorporated with other renewable energy sources. Finally, conclusions and future work are presented in Chapter 6.

ACKNOWLEDGMENTS

I would like to express my deepest gratitude to my advisor, Dr. Issa Batarseh, for his guidance and unlimited support during my graduate studies. His directing experience and critical thinking were a key success of this work. I would like also to express my deep thanks to Dr. Nasser Kutkut for introducing me to the field of battery systems. I appreciate his encouragement, guidance and our fruitful discussions. Many thanks go to my committee members: Dr. Linan An, Dr. Wasfy Mikhael, Dr. John Shen and Dr. Jiann-shiun Yuan for serving in my committee and for their guidance.

I would like to thank my former professor at Jordan University of Science and Technology and later my friend, Dr. Ahmad Harb, for his encouragement all times. I am indebted to Dr. Harb for encouraging me to be always productive and optimistic in life.

Many thanks go to all my friends from the Florida Power Electronics Center at the University of Central Florida. I will never forget the nice times we spent together.

Finally, I would like to thank my family for their love and support. Thanks to my soul mate, my beloved wife Rawan, for her patience, understanding and love. Thanks to my little princess, my lovely daughter Mira, for being a high motivation for me to be a hard worker. Thanks to my first teachers, my mother Entisar and father Raef, for their support. Thanks for everything they sacrificed for me. Simply put, without my parent's love and support, I would never be the person I am today. Last but not least, thanks to my siblings: my brother Adi and sisters Oula and Areen and to my all other family members and friends for their support.

TABLE OF CONTENTS

LIST OF FIGURES

LIST OF TABLES

LIST OF ACRONYMS

AC	Alternating current
A.h.	Ampere-hour
ANNs	Artificial neural networks
BMS	Battery management system
CFD	Cash flow diagram
CC	Constant current
CV	Constant voltage
DC	Direct current
DG	Distributed generation
DOD	Depth-of-discharge
EDLC	Electric double layer capacitor
EIA	Energy information administration
EMP	Electromagnetic pulse protection
EMS	Energy management system
E.P.	Effective price
ES	Energy storage
EKF	Extended Kalman filter
HF	High frequency
ICC	Interrupted charge control
kWh	kilowatt-hour
LF	Line frequency
Li-ion	Lithium-ion
LIC	Lithium-ion capacitor
MSS	Micro-storage system
NiCd	Nickel-cadmium
NiMH	Nickel-metal-hydride
NaS	Sodium-sulfur

OCV	Open-circuit voltage
PLC	Power line communication
PV	Photovoltaic
RMSE	Root mean square error
ROI	Return of investment
SCADA	Supervisory control and data acquisition
SOC	State-of-charge
SOH	State-of-health
SP	Spot price
UPS	Uninterruptable power supply
VRLA	Valve-regulated lead-acid

CHAPTER ONE: INTRODUCTION

1.1 Background and Motivations

For more than one hundred years, utilities have supplied reliable power to the globe with a relatively high quality of service. Today, as electricity demand and customers' expectations grow, utilities are struggling to fulfill these needs. According to the Energy Information Administration (EIA) in the U.S., the world electricity consumption will increase from 15.2 trillion kilowatt-hours in 2010 to 21.7 trillion kilowatt-hours in 2035 at an average annual rate of 1.4% [1]. As a fact, the power outages and interruptions cost the U.S. at least $150 billion each year although the reliability of today's electricity system is around 99.6% [2]. In addition to the rapidly increasing electricity demand and customer expectations, the dramatically skyrocketing and unpredictable oil and gas prices, the aging of the grid infrastructure, and the need to reduce CO_2 emissions, are factors that add more burdens on utilities to fulfill future demand.

Distributed renewable sources are rapidly becoming an integral part of utility grids throughout the world. Among all renewable sources, solar and wind power are the most matured and adapted sources worldwide. These sources are becoming more popular due to their unique characteristics, such as being environmentally friendly and free sources of energy (excluding initial costs). Figures 1.1 and 1.2 show recent cumulative installed capacity of solar photovoltaic (PV) and wind power in some countries, respectively [3], [4].

However, the integration of distributed renewable energy into the utility grid is performed in a so called "feed and forget" fashion [5]. Yet, large scale integration of renewable sources into

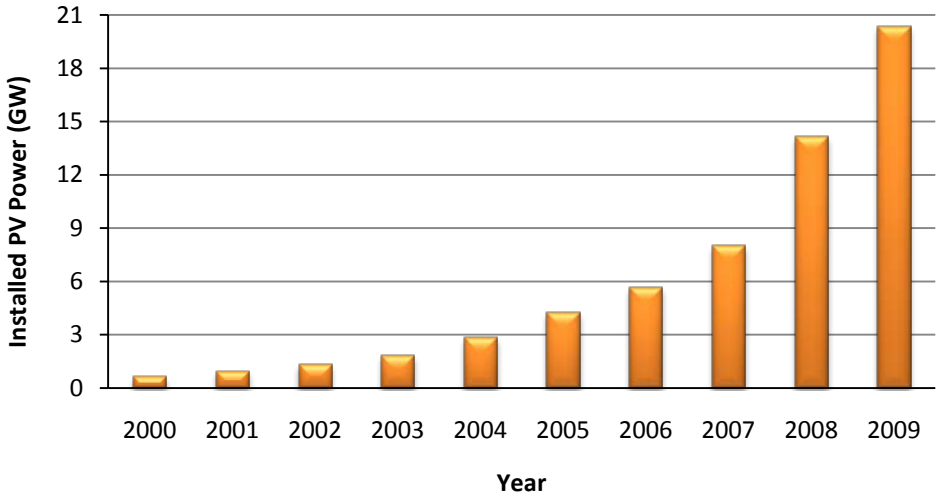

Figure 1.1: Cumulative installed PV power in IEA PVPS countries [3].

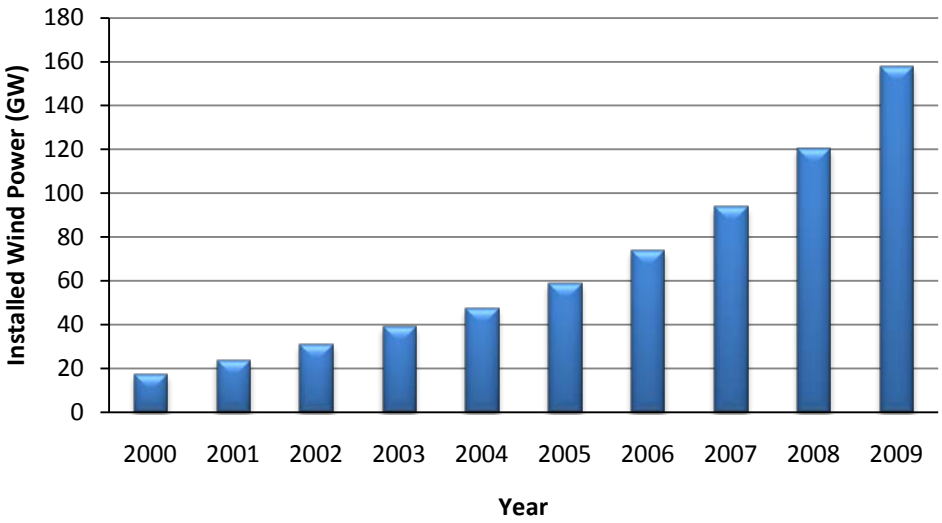

Figure 1.2: Cumulative global installed wind power [4].

the grid can be problematic due to the intermittency of these sources which can impact the quality and security of energy supply. Also, these sources are mostly out-of-synchronization with demand, which means that generation peaks and demand peaks don't match most times. Thus, energy storage can be used to mitigate the intermittency of supply and inject power to the grid to alleviate peak demands. A typical load profile for a residential application is shown in Figure 1.3.

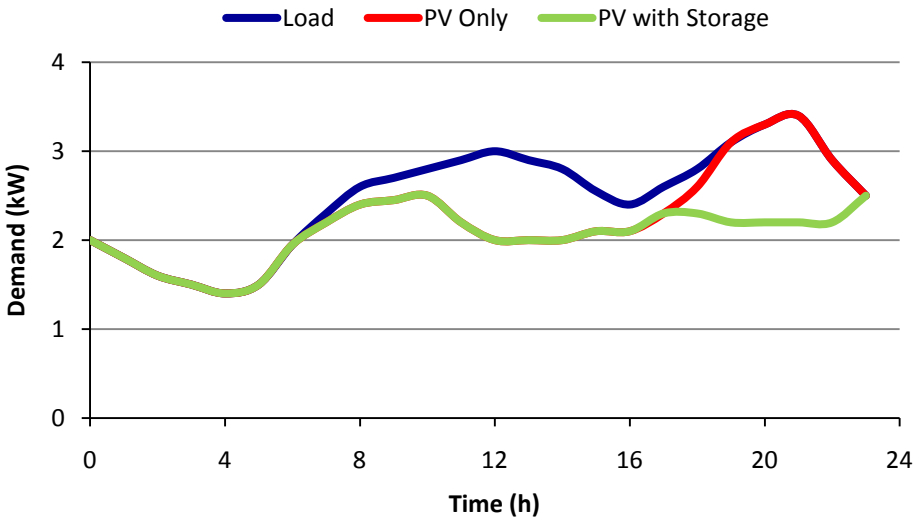

Figure 1.3: Typical load profiles with the effects of PV and storage.

As shown in Figure 1.3, there are two peak demand periods; a mid-day peak demand and an evening peak demand. If a PV distributed generation (DG) is employed, the morning peak demand can be partly covered, while the evening peak demand, which can be higher, remains. If a storage system is employed, both the morning and evening energy peaks can be partly or completely covered depending on the size of the MSS.

Apparently, there is a global trend towards restructuring the electricity market generation and transmission system from centralized to decentralized than expanding the current system [5], [6]. In a spot market electricity system (a deregulated electricity market where the electric power is exchanged between the utilities and customers through bids to buy and offers to sell based on the supply and demand), the spot prices of electricity vary during day hours. For example, they are low during off-peak hours when the demand is low, and are high during on-peak hours when the demand is high. A typical solution to reduce the load peaks during the day, and thus saving costs of building new high-power generators by the grid utilities, is to store energy in storage

devices during off-peak hours and push this energy back to the utility grid during on-peak hours [7].

In addition to reducing the demand peaks, energy storage can increase the reliability and feasibility of renewable energy sources by storing excess generated power, reducing the swing in the power generated by those sources, and compensate for the forecasting errors between the forecasted and actual exchange plan with a spot electricity market.

Thus, there are three main advantages of installing distributed energy storage systems in deregulated electricity markets:

- They increase the efficiency of the entire power system by allowing leveling the load, shaving the peak demands, and reducing losses in the transmission lines.
- They allow transacting power with the utility grid.
- They support the operation of distributed renewable energy sources.

In a spot market system, the power exchange plan with the utility grid must be provided to the market in advance. For example, in the Nordic spot market, participants must announce their daily bids at least 12 hours before the scheduling day [8]. In the presence of renewable sources, it is impossible to match the scheduled exchange plan with the market due to the uncertainties in the weather prediction (solar radiation, wind velocity, etc.). Therefore, energy storage can be used to supply or sink any difference between the forecasted and actual generated power to avoid penalties due to violating the forecasted (scheduled) plan.

In fact, there are two common approaches to participate in a market system which are feed-in tariff and demand response programs. Feed-in tariffs are simply defined as fixed payments per kilowatt-hour for electricity generated by a renewable source. On the other hand, demand

response refers to short-term changes by customers in their accustomed electric consumption patterns to reduce or shift electric load over time. These changes are made in response to incentive payments designed to induce lower electricity use, or in response to load reduction request signals sent by utilities when the wholesale price becomes high or when system reliability is jeopardized [10]. Demand response programs offer a variety of options, some of which are summarized as follows:

1. Incentive-based Programs:
    - *Direct Load Control*: The program operator remotely shuts down or cycles a customer's electrical equipment (e.g. air conditioner, water heater, etc.) on short notice. This option is normally offered to residential or small commercial customers.
    - *Demand Bidding/Buyback Programs*: Customers offer bids to curtail based on wholesale electricity market prices. This option is offered to large customers (one megawatt and over).
    - *Emergency Programs*: Incentive payments are offered to customers for load reductions during periods when reserve shortfalls arise.
2. Price-based Programs:
    - *Time-of-Use*: Different hourly rates are defined for a 24 hour day. These rates reflect the average cost of power generation and delivery during those time periods.
    - *Real-time Pricing*: A rate in which the electricity price fluctuates hourly reflecting changes in the wholesale electricity price. A day-ahead or an hour-ahead notice is usually given to customers.

- *Critical-peak Pricing*: This program is a combination between the time-of-use and real-time pricing programs. In this program, the basic prices are the time-of-use prices. Under certain conditions, such as when the system reliability is compromised or supply prices are very high, the normal peak prices are replaced with higher (critical) peak prices.

1.2 Objectives and Contributions

The main objective of this dissertation is to design a complete EMS to control the operation of a MSS when operated in a dynamic market system. The following is a brief description of the main contributions:

In Chapter 2, some design considerations of the MSS are discussed:

- Some system architectures are evaluated and compared. The system including the energy storage unit and the power converter (charger or inverter) must allow a high degree of flexibility and must be upgradeable. This will have a great advantage when upgrading the MSS, which can be achieved by connecting more MSS modules together.
- A system sizing procedure derived from a residential case study is given. The system's size must be selected properly to achieve the highest economic benefit. To design the size for both the energy storage and the power converter, some practical load behaviors must be analyzed. That is, the demand peaks at the end user side must be analyzed and the results of the duration and energy of those peaks are then used to determine the optimum size.

- Some grid-tied inverter design aspects are presented. Grid-tied inverters require advanced features to insure a high-quality power pumped to the grid. Some of the techniques used in grid-tied inverters depend on the size of the inverter. For example, systems with DC input voltage above 50 volts require grounding while those below 50 volts do not. Moreover, the DC-current injected to the grid must be limited to 0.5% of the rated inverter current to avoid saturating the distribution transformer. Other design issues of the inverter include the number of stages, which can be either a single stage inverter with a high efficiency and low cost, or a multi-stage inverter with a lower efficiency and higher cost. In addition, the power stage architecture can be either bidirectional (inverter and charger), or two separate unidirectional inverter and charger.
- Some economic analyses are presented. Since the economic benefit is the most important goal for both utilities and end users, all economic aspects of the system are addressed. Two economic models are developed; a static economic model and a dynamic economic model. The static model handles all issues related to initial costs and hourly and daily costs and returns. On the other hand, the dynamic model is used to determine whether to exchange power with the utility grid or not depending on the predicted return.

In Chapter 3, some charging methods are discussed:

- Some recent charging algorithms for single and multiple battery chargers are presented and evaluated through some experimental tests data.
- Directions for charging improvement are given.

In Chapter 4, a battery model with SOC and SOH estimation techniques are proposed:

- A battery model with the capability to predict the voltage across the battery in real-time is proposed. This model is fairly accurate and can be easily implemented and derived.
- The proposed battery model is used to estimate the battery SOC in real-time. The SOC is an indication of the amount of energy in the battery compared to the battery's full capacity. The SOC must be estimated continuously to avoid over (dis)charging the battery.
- The proposed battery model is also used to estimate the SOH of the battery in real-time by estimating either its discharge capacity or internal resistance. The SOH is an indication of the current battery's condition compared to its new condition. The SOH must be estimated periodically to predict the remaining lifetime of the battery and to calculate the expected return or the cost of exchanging power with the grid.

In Chapter 5, an EMS is proposed:

- A load forecasting model is developed using artificial neural networks (ANNs). This model is used to predict the demand for a certain time horizon in order to schedule a future operation.
- A weather forecasting model using ANNs is developed to predict the solar radiation and wind velocity. This model is used to predict the amount of power that can be generated from solar and wind power plants for a certain time horizon and schedule an exchange plan with the market accordingly.
- An EMS is proposed to manage the operation of the MSS. The developed models (economic model, battery model and load/weather forecasting models) are combined together in order to manage the operation of the MSS in such a way to maximize the

economic return by optimally scheduling the power exchange plan with the spot electricity market.

CHAPTER TWO: DESIGN CONSIDERATIONS OF DISTRIBUTED GRID-TIED MICRO-STORAGE SYSTEMS

2.1 Introduction

It is extremely important to properly design the MSS for a maximum benefit. For example, the system must have minimized power losses, flexible and robust design, and must deliver a high-quality power to the grid economically. The economic benefit of the system can be increased by properly sizing the system and operating it at its rated power. More details regarding the design of micro-storage systems are provided in the following sections.

2.2 System Architecture

The architecture for the proposed MSS can be inline, DC-coupled or AC-coupled [14]. The inline configuration is also known as series configuration since all the blocks are connected in series, whereas the parallel connection is referred to the method in which the blocks are connected to a common DC or AC bus. All these architectures are discussed in this section where the reference DG source is solar PV, but other DG sources can be used.

2.2.1 Inline Systems

With an inline configuration, the energy storage bank is inline with the PV generation system as shown in Figure 2.1. In these systems, all DGs (in case of multiple DG systems) feed DC power to the battery bank. For most systems of this type, all the generated power is processed through the battery resulting in an increased cycling of the battery and reduced system efficiency.

In addition, these systems suffer from inflexibility since the storage bank size is dictated by the PV system size.

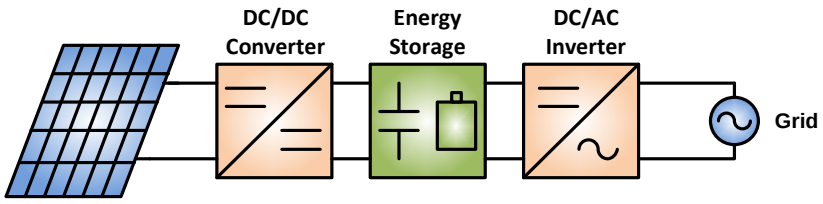

Figure 2.1: Inline system architecture.

2.2.2 DC-coupled Systems

In a DC-coupled configuration, an intermediate DC bus couples the PV system and the storage system as shown in Figure 2.2. The advantage of this approach is that the PV and storage systems work independently, which increases the system's robustness. However, this approach suffers from inflexibility since the PV system and the energy storage share the same inverter making the storage system prone to single point failures and limiting the size of the storage system.

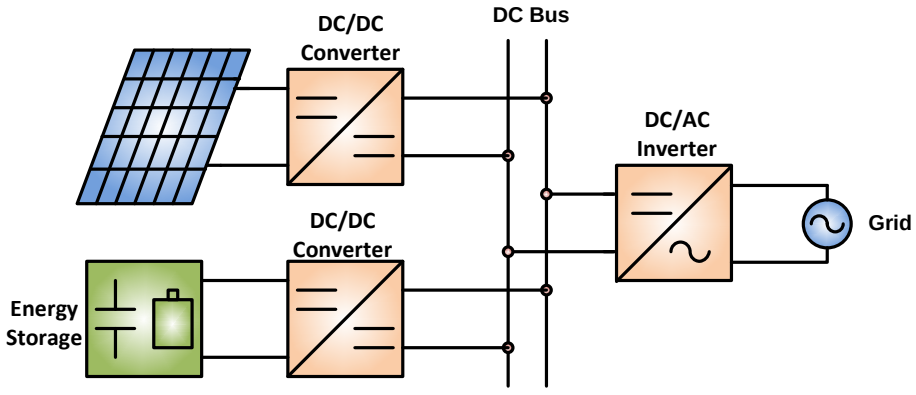

Figure 2.2: DC-coupled system architecture.

2.2.3 AC-coupled Systems

In an AC-coupled system, both the PV system and the storage system are completely independent and do not share any common blocks as shown in Figure 2.3. The advantage of an AC-coupled system is that the MSS can be sized independently and can be easily modularized.

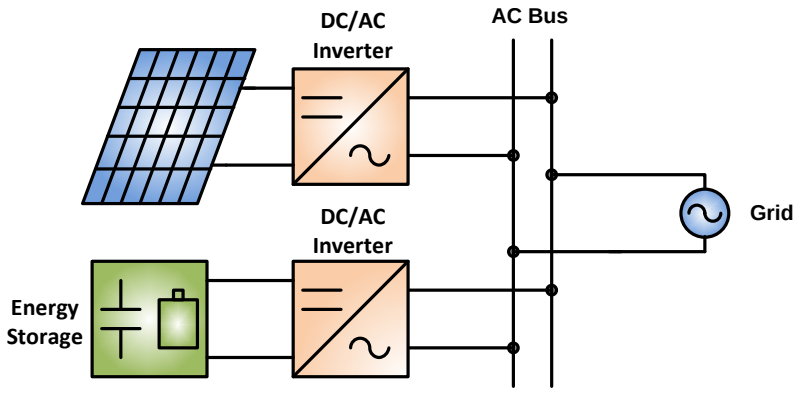

Figure 2.3: AC-coupled system architecture.

In fact, most DG systems are either DC- or AC-coupled. Compared to DC-coupling, AC-coupling allows modularity and scalability of the system, which is quite advantageous since it allows upgrading the whole system including the DG and the MSS independently. Also, AC-coupling allows combining multiple power generation sources, which would be harder or inefficient to achieve with traditional DC-coupling. Finally, AC-coupled systems are more robust than inline and DC-coupled systems since each of the DGs and the storage has an independent path to the grid.

2.3 Inverter Design Considerations

Cost effectiveness and reliable performance are key issues in the inverter design. To optimize the design of the inverter, many aspects must be considered. Some of these aspects are discussed below.

2.3.1 Grounding

According to [11], ungrounded PV systems provide the best fire hazard reduction, where grounded PV systems provide the best personnel protection from electrical shock. Generally, for systems with relatively high voltages, grounding is important for safety, electromagnetic coupling suppression, and electromagnetic pulse protection (EMP) [12]. As a requirement for electrical systems in the U.S., all systems with voltages greater than 50 volts must be grounded according to the IEEE 1547 [13]. Grounding can be achieved by either grounding the PV source itself and monitoring for ground faults or by grounding the equipment including the PV and storage sources, which can be achieved by connecting the frames and all other metallic parts to ground. Since the utility has one grounded terminal (neutral-N), the grid-connected inverter has to support the dual ground operation where both the DC and AC sides are grounded. Consequently, the inverter also has to prevent any DC current from passing to the grid. This can be accomplished by using isolated or non-isolated inverter topologies.

2.3.2 Galvanic Isolation

Transformers are commonly used in grid-tie inverters since they provide galvanic isolation and prevent DC current injection. For grid-tie inverters, it is very important to limit the DC

current injection to the grid to prevent disturbing the regular operation of the upstream distribution transformer, which can shift the operating point of the transformer and cause saturation. As a requirement in the US, the DC current injected into the grid must not contain a DC value of more than 0.5% of the rated inverter current [13]. According to the operating frequency of the transformer, the transformer can be a line-frequency (LF) or high frequency (HF) transformer. Although a LF transformer can limit the DC current injection more than a HF transformer, it suffers from large volume and weight, high cost, low efficiency and low power factor especially under light load conditions. HF transformers, on the other hand, employ a transformer in the DC-DC stage with a high operating frequency. This leads to a reduction in weight, volume, and increased efficiency. For both LF and HF transformers, the efficiency of the whole system is decreased due to the losses in the transformer windings and core. In addition to providing galvanic isolation, the transformer also provides voltage amplification, which is needed to boost the voltage of the DC input source.

Occasionally, non-isolated (transformerless) inverters are preferred due to their light weight, small volume and low cost as well as their high efficiency (1-2% efficiency improvement compared to HF isolated inverters). However, transformerless inverters must be able to eliminate or minimize the leakage current in order to meet the safety standards. This can be achieved by either keeping the common-mode voltage across the DC source (PV module or storage unit) constant or by disconnecting the DC side from the ac-side [15].

2.3.3 Power Conversion Architecture

There are two possible ways to achieve the two-way power conversion for charging or discharging the energy storage units. The power conversion stage can have a bidirectional single path inverter/charger or two unidirectional separate paths for the inverter and the charger. Although the bidirectional inverter/charger offers low component count, most likely it will have a complex and high-cost controller. Also, it requires bidirectional switches, which is a challenge for bidirectional power converters [16]. These switches are implemented by using two MOSFETs or IGBTs in series, which leads to higher losses and lower overall efficiency. Also, the bidirectional inverter/charger must be sized to the highest peak power in charging and discharging operations. If separate inverter and charger are employed, unidirectional switches can be used. In this case, the inverter and the charger can be sized independently to accommodate the requirements during (dis)charging the storage unit. That is, the inverter can have a higher power than the charger since the system will pump power to the grid during peak hours over short intervals, while it can be charged during off-peak hours over relatively long intervals.

2.3.4 Number of Stages

According to [12], single-stage inverters offer simple structure and low cost, but suffer from a limited range of input voltage variations and are often characterized by compromised system performance. On the other hand, multiple-stage inverters operate over a wide range of input voltage variations, but suffer from high cost, complicated structure and lower efficiencies. Since the battery voltage varies with respect to its SOC, and since the DC voltage will most likely need to be stepped up, a multi-stage inverter is more suitable in this application.

2.4 System Sizing: A Residential Case Study

The MSS can be sized based on the average power consumption of a typical house. Although each house has a unique load profile that is dependent on the residents' behavior and the number and nature of the appliances connected to the grid, studying the load nature of a typical house can be somehow useful in properly sizing the MSS.

In a comprehensive study conducted by the Florida Solar Energy Center (FSEC), the load profile of ten houses was monitored for an entire year and the energy consumption was continuously recorded [17]. The average energy consumption for these houses was 42.8 kWh/day, which is close to the average energy consumption of the residential sector in Florida namely 38.2 kWh/day in 2007 according to the EIA [18]. In this study, the maximum and minimum energy consumption curves for the monitored houses were approximated and drawn as shown in Figures 2.4 and 2.5, respectively.

Assuming the peak consumption periods are defined as the intervals during which the power consumption is above its mean value, that is, from 6:00 am to 7:45 am (first peak) and 10:00 am to 10:00 pm (second peak) in Figure 2.4, and from 6:25 am to 7:55 am (first peak) and 6:00 pm to 12:00 am (second peak) in Figure 2.5. Based on the definition of the peaks, the duration and the power of each peak as well as the total energy of both peaks (total area) for each house are calculated as shown in the Table 2.1.

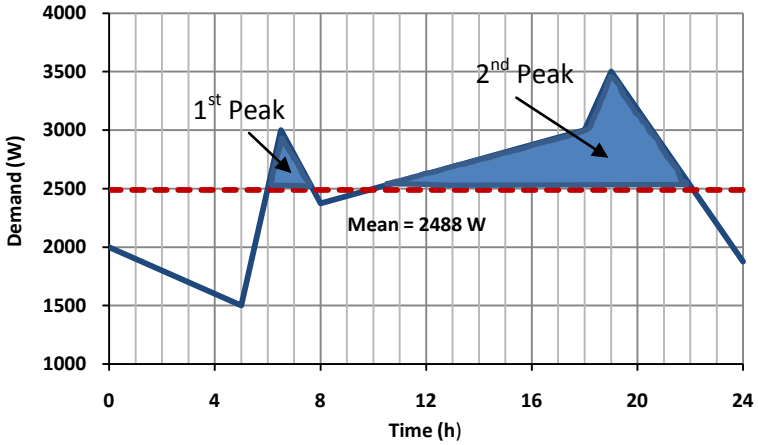

Figure 2.4: Linearized average load profile for the maximum energy consumption house in [17].

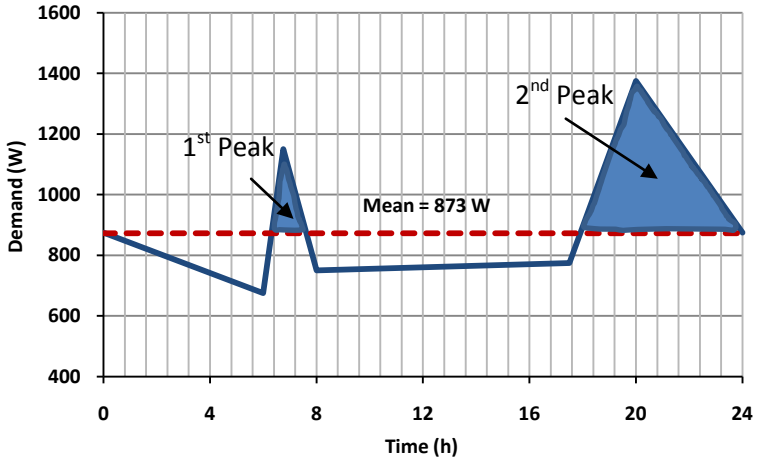

Figure 2.5: Linearized average load profile for the minimum energy consumption house in [17].

Table 2.1: The duration and power of each peak and the total energy of both peaks.

	1st Peak	*2nd Peak*	*Total Energy*
Maximum House	105 min 0.51 kW	720 min 0.10 kW	13.0 kWh
Minimum House	90 min 0.28 kW	360 min 0.50 kW	3.4 kWh

Two parameters dictate the size of the storage system; namely the peak power capability and the maximum duration of operation. The peak power capability is important in sizing the DC-AC inverter while the maximum duration of operation is important in sizing the ES bank. The storage system can be oversized to further reduce peak demands and inject power into the grid

when energy prices are relatively high. In this case, end users can leverage pricing differentials between night and day hours, where the MSS can be charged from the utility grid during the night when the electricity rates are low and the stored energy can then be pumped back into the grid during daily peak demand hours when the electricity rates are relatively high. This should also accelerate the payback of these systems.

Referring to Table 2.1, to completely cover the peak demand interval for the maximum and minimum houses, an energy storage with a size of 13.0 kWh (maximum house) and 3.4 kWh (minimum house) are required. Since the sizing discussion here is generic and is intended to meet the average demand of typical houses, the average of the two storage sizes, which is 8.2 kWh, can be assumed for a typical system. However, the size and cost of such a system can be quite high. Practically, the ES size can be reduced by reducing the peak coverage ratio. If, for example, the ES was chosen to cover 30% of the total peak energy demand, then the size can be reduced to 30% of the average size, i.e. 2.5 kWh. Table 2.2 summarizes practical system sizing based on these assumptions.

Table 2.2: The system components' sizes.

	Typical Size	*Nominal Size*
Inverter	0.5 kW - 1 kW	0.75 kW
Energy Storage	2 kWh - 3 kWh	3 kWh

Furthermore, the size of the converter with respect to the energy storage can be verified from an economic point of view. In Table 2.3, the four highest and lowest spot market electricity prices for four different days [19]-[20] were normalized, where h_1, …, h_4 are the four hours at which the spot prices are the lowest (off-peak) or highest (on-peak), and SP_{n1}, …, SP_{n4} indicate

the normalized spot price (SP) [spot prices divided by the lowest *SP* (values ≥ 1) and highest *SP* (values ≤ 1) for the four different days].

Table 2.3: Normalized on-peak and off-peak spot electricity prices.

	Off-peak				*On-peak*			
	h_1	h_2	h_3	h_4	h_1	h_2	h_3	h_4
SP_{n1}	1	1.05	1.05	1.05	0.98	0.98	0.98	1
SP_{n2}	1	1.04	1.04	1.04	0.95	0.95	0.98	1
SP_{n3}	1.03	1.05	1.03	1	0.94	1	0.95	0.9
SP_{n4}	1.1	1	1	1.06	0.99	1	0.94	0.98

From the above table, it can be seen that the off-peak and on-peak prices are almost constant within a four-hour period. In the extreme case, the price changed by 10% (3rd case). This concludes that either the charging or discharging can be performed in a relatively long time (i.e. four hours) which again emphasizes that the inverter (charger) size is around 0.75 kW for a 3 kWh energy storage capacity, or in general terms, the inverter (charger) size (in kW) is 25% of the energy storage capacity size (in kWh) divided by one hour (h).

Since customers' demands can widely vary, increasing the system size can be achieved by paralleling more storage modules especially if the MSS is AC-coupled. By oversizing the system, the excess energy can be sold back to the utility during peak demand periods.

2.5 Energy Storage Technologies

Different battery technologies can be employed to realize the ES bank. Table 2.4 compares some of these technologies in terms of cost and cycle-life [21]-[25]. In order to properly evaluate the different technologies, the cost per kWh and the cycle-life must be considered. Therefore, to express the cost in a more practical way, the effective price (E.P.) is defined as the

ratio between the cost ($/kWh) and the cycle-life divided by the recommended depth-of-discharge (DOD). The E.P. is used to evaluate the economics of those storage technologies.

Table 2.4: Characteristics of some energy storage technologies.

	Energy Density (Wh/kg)	*Cost (kWh)*	*Recommended DOD*	*Cycle Life*	*E.P. (DOD=100% is assumed)*
Flooded Lead-Acid	25	$150	70%	1,500	0.14
VRLA	30-50	$200	80%	200-300	0.83-1.25
Li-ion	90-190	$1,333	80%	2,000	0.83
NiMH	30-80	$800	100%	1,000	0.8
NiCd	40-60	$600	100%	2,000	0.3
NaS	100	$450	100%	2,500	0.18
Zinc Bromine	70	$500	100%	1,000	0.5
EDLC SuperCap.	6-10	$44,070	100%	1,000,000	0.044
LIC SuperCap.	15	$61,600	100%	100,000	0.616

Battery technologies differ widely in terms of their energy and power densities, cost, cycle-life, availability, and operating conditions. For example, flooded lead-acid batteries are quite inexpensive and have high cycle-life, but they have low energy densities (25 Wh/kg) and require periodic maintenance. On the other hand, valve regulated lead-acid (VRLA) batteries are also inexpensive and widely available, but they have low cycle-life and low energy densities (30-50 Wh/kg). In contrast, Li-ion batteries have very high energy densities (90-190 Wh/kg) and relatively high cycle-life, but are expensive and require advanced circuitry to protect the cells during charging. A compromise solution between VRLA and Li-ion batteries is the nickel-metal-hydride (NiMH) batteries, which offer higher energy densities and higher cycle-life in comparison to VRLA batteries at a lower price compared to Li-ion batteries. Nickel-cadmium (NiCd) batteries have good characteristics in terms of E.P., but they have two drawbacks; they suffer from memory effect, which is a term used to describe the degradation in the battery capacity when it is partly charged and discharged, and they are not environmentally friendly. Regarding NaS and Zinc

Bromine batteries, they have good characteristics in terms of cost and cycle-life, but these technologies are not fully mature and are not widely available as other batteries. Other technologies such as Supercapacitors or ultracapacitors have their advantages and drawbacks; for example, they have higher power densities and much higher cycle-life in comparison with batteries, but, they are still under research and will not be commercially available until their prices drop significantly in order to compete with other technologies. Depending on the budget and the operating conditions, the storage technology of the MSS can be chosen.

In fact, lithium-ion (Li-ion) batteries are one of the most promising technologies. In addition to the projected long-term declining cost of Li-ion batteries, the rapid adoption of Li-ion batteries by the automotive industry could further reduce battery costs. Since in electric vehicle (EV) applications, the battery must be replaced when its capacity drops to 80% of initial capacity, fully used EV batteries can be reused as micro-storage batteries. If these batteries are recalibrated and retested, they can be resold as stationary batteries for micro-storage applications, which can result in a dramatically reduced cost [26].

Regardless what battery technology is used, a BMS that is capable of managing the operation of the battery in real-time is needed. The BMS must insure proper (dis)charge cycles by preventing the battery from over (dis)charge to extend its lifetime. Also, the BMS must predict the amount of energy available in the battery compared to its maximum capacity (SOC) and the battery's current condition compared to its new condition (SOH). Further details are included in Chapter 4.

2.6 Communication and Smart Grid Integration

Establishing an external communication channel between the utility and end users allows both utilities and end users to monitor and control power demand resulting in an increased security and quality of service. An MSS must incorporate advanced communications and controls functionality to allow for seamless integration with future smart grids while allowing utilities to easily dispatch stored energy. In fact, the MSS should be controlled remotely by the utility or locally by the end user. To perform data gathering and control, the MSS must incorporate internal communication links with other devices, such as power meters, to monitor the power consumed by the house or the power generated by the renewable sources (solar panels or wind turbines). Once the critical power system data is gathered and manipulated, the MSS can be properly controlled. Depending on the desired data communication rate and the amount of data, the communication medium can be selected.

There are many ways to establish communication between the utility and end users. These vary in terms of data rates, reliability, and cost. Some of these possible communication options include:

- *Power Line Communication* (*PLC*): PLC can be used to perform communication with the utility. It offers a very low cost solution since the power lines already exist, but it suffers from interference problems as well as range due to their limited ability to bypass distribution transformers.
- *Ethernet*: End users can be connected to a common server (utility server) through an Ethernet connection. The MSS can be connected to an online personal computer or is assigned an internet protocol (IP) address to allow communication with the utility server

through an Ethernet cable. However, in areas where a dedicated Ethernet connection or IP address is unavailable, this may not necessarily be a universal solution.

- *Wireless*: The main advantages of a wireless communication link are its high accessibility and extended range. A popular example of wireless communication is the ZigBee standard, which is used widely in home control and automation applications. ZigBee communication has a promising future due to its low cost and low power consumption.

- *Optical Fiber*: Besides the high initial cost of creating an optical fiber infrastructure, this option offers unique advantages in terms of the very high speeds (light speed) and high data rates (up to 100 Mbps).

The MSS will typically be integrated into the smart grid through the smart metering infrastructure, which will include an EMS. Figure 2.6 shows a typical smart grid network with integrated distributed micro-storage systems. The single arrow line indicates a unidirectional power flow, the double arrow discrete line indicates a two way communication link, and the double arrow continuous line indicates a bidirectional power flow and two way communication link.

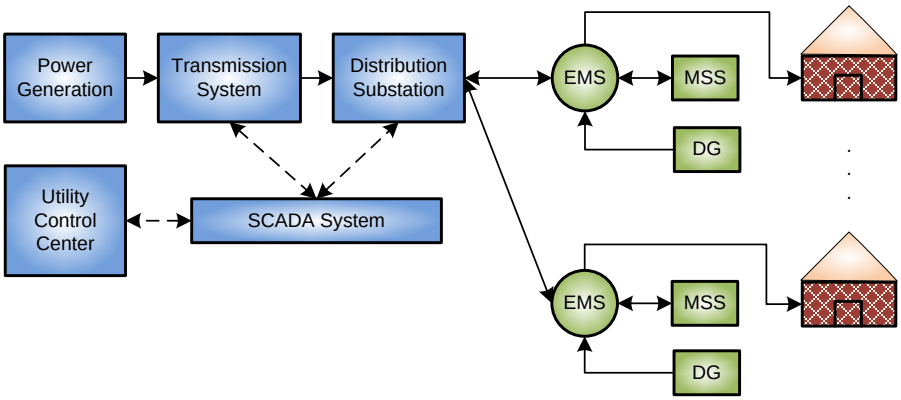

Figure 2.6: A diagram shows the integration of the MSS with the smart grid.

The MSS must operate in such a way to maximize the expected return. In fact, there are two different scenarios to operate the MSS in a market system. If the distributed system is made of a MSS only, the operation will be simply to charge the system during off-peak hours and discharge it during on-peak hours provided a minimum expected return is achieved (more details in section 2.7). On the other hand, if renewable DGs were incorporated with the MSS, then, the operation will be basically to compensate any difference between the forecasted power exchange plan with the market and the actual generated power for a given time horizon to avoid penalties of violating the forecasted plan. The operation of the MSS when integrated with other distributed renewable sources is achieved through an EMS, which will be covered in Chapter 5.

2.7 Economic Analysis

The benefits of understanding the economics involved in the system are to determine the economic feasibility of the system (static model) and to design an economic-based operation strategy that maximizes the return (dynamic model). This section discusses these aspects for the MSS.

2.7.1 Static Economic Model

The system capital cost, or the total investment, refers to the cost of the entire system including costs of the battery storage, power converters, controllers, BMS, packaging, etc. The daily profit of the system is calculated by subtracting the off-peak charging cost from the on-peak discharging return.

Simply, the daily return equation can be written as:

$$\text{Daily Return} = \sum_{i=0}^{23} SP_H(i).E(i) \tag{2.1}$$

And the daily profit is:

$$\text{Daily Profit} = \sum_{i=0}^{23} SP_H(i).E(i) - \sum_{i=0}^{23} SP_L(i).E(i) \tag{2.2}$$

where SP_H and SP_L are the on-peak and off-peak spot prices (in \$/kWh), respectively, and E is the energy exchanged between the MSS and the utility (in kWh).

To evaluate the economic feasibility of the system in terms of its capital cost and operational return, two well-known economic evaluation tools can be used. Purposefully, the analyses in this section are generalized and can be used to evaluate any system.

2.7.1.1 Return of Investment (ROI)

One way to determine the overall economic feasibility of an investment is through the ROI. The ROI is defined as follows:

$$\text{ROI} = \frac{\text{Overall Net Profit} - \text{Total Investment}}{\text{Total Investment}} \times 100\% \tag{2.3}$$

The overall net profit can be estimated by calculating the predicted profit at the end of the energy storage life based on average calculations. The overall profit is:

$$\text{Overall Net Profit} = \left(\frac{L_\infty}{\text{DOD}} \right) \times \bar{C} \times \bar{p}_{diff} - f_M \tag{2.4}$$

where L_∞ is the datasheet cycle-life at DOD=100%, DOD is the desired depth-of-discharge, $\bar{C}$ is the average usable capacity over the ES life (kWh), $\bar{p}_{diff}$ is the predicted average differential price (\$/kWh), and f_M is the maintenance cost. Substituting (2.4) in (2.3) yields:

$$\mathrm{ROI} = \frac{\left(\frac{L_\infty}{\mathrm{DOD}}\right) \times \bar{C} \times \bar{p}_{diff} - f_M - f_C}{f_C} \times 100\% \tag{2.5}$$

where f_C is the total cost or investment. Dividing the numerator and denominator by L_∞ yields:

$$\mathrm{ROI} = \frac{\left(\frac{1}{\mathrm{DOD}}\right) \times \bar{C} \times \bar{p}_{diff} - \frac{f_M}{L_\infty} - \frac{f_C}{L_\infty}}{\frac{f_C}{L_\infty}} \times 100\% \tag{2.6}$$

Defining the ratio between the cycle-life and the capital cost as the normalized cycle-life per dollar of capital cost, L_N:

$$L_N = \frac{L_\infty}{f_C} \tag{2.7}$$

By substituting (2.7) in (2.6) and neglecting the maintenance cost over cycle-life term yields:

$$\mathrm{ROI} \approx \frac{\left(\frac{1}{\mathrm{DOD}}\right) \times \bar{C} \times \bar{p}_{diff} - L_N^{-1}}{L_N^{-1}} \times 100\%$$

Or,

$$\mathrm{ROI} \approx \left(\left(\frac{1}{\mathrm{DOD}}\right) \times \bar{C} \times L_N \times \bar{p}_{diff} - 1\right) \times 100\% \tag{2.8}$$

Assuming a DOD=100% and an average capacity of 1 kWh, the ROI vs. L_N curves for this case are plotted at four differential electricity prices, as shown in Figure 2.7. Note that the horizontal axis, L_N, reflects the number of cycles achieved for every dollar of capital cost invested in the MSS.

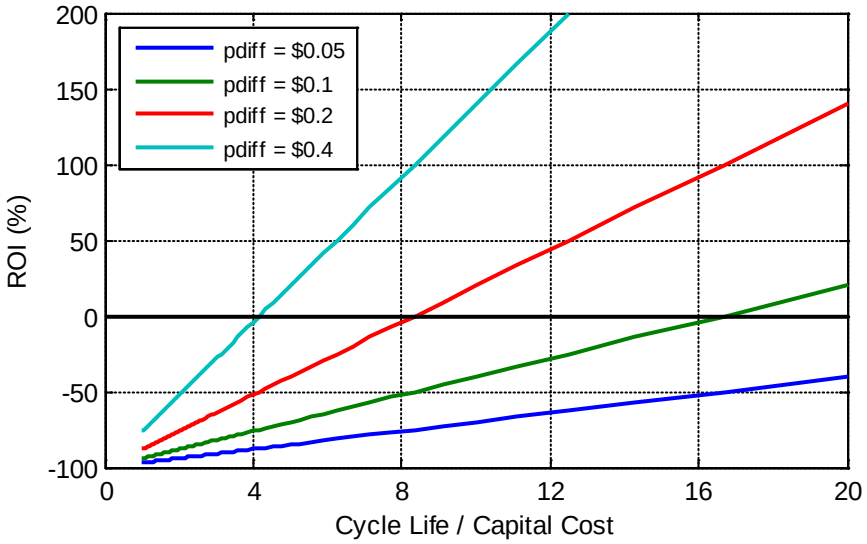

Figure 2.7: ROI curves as a function of the (cycle life/capital cost) at different differential prices.

2.7.1.2 Cash Flow Diagram (CFD)

Another way to evaluate the economic feasibility of the system is the cash flow diagram. This tool is usually used in engineering projects to find the costs and benefits of projects over time. In contrast to the ROI where only the overall benefit is calculated at the end of the last year, the CFD calculates the benefit and cost at every year.

Assuming a regular operation and fixed number of cycles every year, the number of the years of operation is:

$$\text{No. of years} = \frac{\text{Cycles}}{\text{Cycles/year}} = k$$

If the battery will be used until its capacity drops to 50%, the relative discharge capacity, *D*, at the end of year *j* is:

$$D_j = \frac{C_j}{C_0} = 1 - \frac{j}{2 \times k} \tag{2.9}$$

where j = 1, 2, … k, C_j is the discharge capacity at the end of year j, and C_0 is the initial discharge capacity.

The average relative discharge capacity of year j is:

$$\overline{D}_j = \frac{D_j + D_{j+1}}{2} = \frac{\left(1-\frac{j}{2k}\right)+\left(1-\frac{j+1}{2k}\right)}{2} = 1-\left(\frac{2j-1}{4k}\right) \tag{2.10}$$

The profit at the end of each year is calculated from (2.11):

$$\left(Profit\right)_j = L_j \times \mathrm{DOD} \times \left(1-\left(\frac{2j-1}{4k}\right)\right) \times C_0 \times \left(\overline{SP_H} - \overline{SP_L}\right) \tag{2.11}$$

For examples, at the end of years 1 and 2, we have:

$$\left(Profit\right)_1 = L_1 \times \mathrm{DOD} \times \left(1-\frac{1}{4k}\right) \times C_0 \times \left(\overline{SP_H} - \overline{SP_L}\right)$$

$$\left(Profit\right)_2 = L_2 \times \mathrm{DOD} \times \left(1-\frac{3}{4k}\right) \times C_0 \times \left(\overline{SP_H} - \overline{SP_L}\right)$$

where L_j is the cycles completed in year j. At j=k:

$$\left(Profit\right)_k = L_k \times \mathrm{DOD} \times \left(\frac{1}{2}\right) \times C_0 \times \left(\overline{SP_H} - \overline{SP_L}\right)$$

The CFD is shown in Figure 2.8.

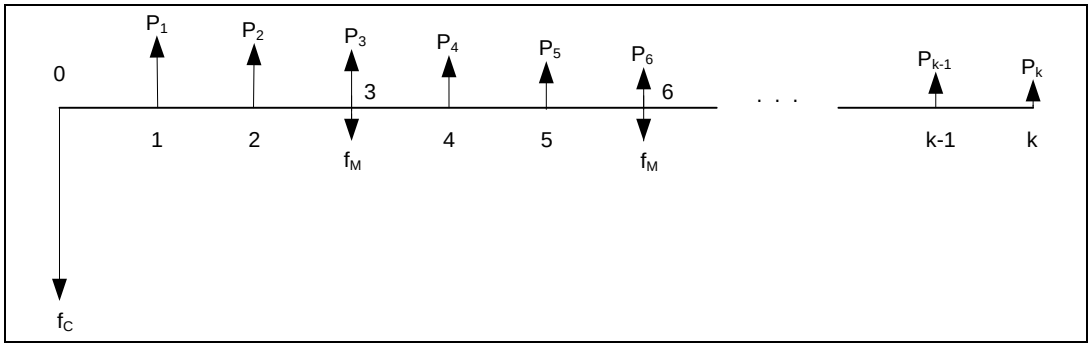

Figure 2.8: A generalized CFD of the MSS.

From the ROI and the CFD analyses, it can be concluded that: firstly, the system's economic feasibility is directly proportional to the battery cycle-life and differential electricity price, and inversely proportional to the system cost, and secondly, the expected profit decreases as the battery ages due to the degradation in the battery capacity.

2.7.2 Dynamic Economic Model

The dynamic economic-based decisions can be implemented in the EMS. Economic-based decisions can be performed for operating or not operating the MSS after the expected return is calculated from the given input data. Figure 2.9 shows the operation of the system. There are three possible states for the system; charge, discharge, or idle. The scheduling operation strategy shown in Figure 2.9 is summarized as follows:

- The operation scheduling is initiated on daily basis at a specific hour (t_{sch}).
- The initial SOC and SOH for the scheduled day are imported from the BMS.
- The hourly spot prices for the scheduled day are communicated from the utility provider.
- If SP is between SP_{min} and SP_{max}, the system turns to "idle" state.
- If SP is below SP_{min}, then, if the system is not fully charged, the system will go to "charge" state, otherwise, if the system is fully charged, it will go to "idle" state.
- If SP is greater than SP_{max}, and the system SOC is above 20%, then, if the predicted return is above R_{min} (R_{min} is a function of electricity prices and SOH), the system will "discharge" state, and otherwise, if the system SOC is at 20%, the system will go to "idle" state.
- The timer (t) is incremented until it reaches 23 (last hour in the scheduled day).

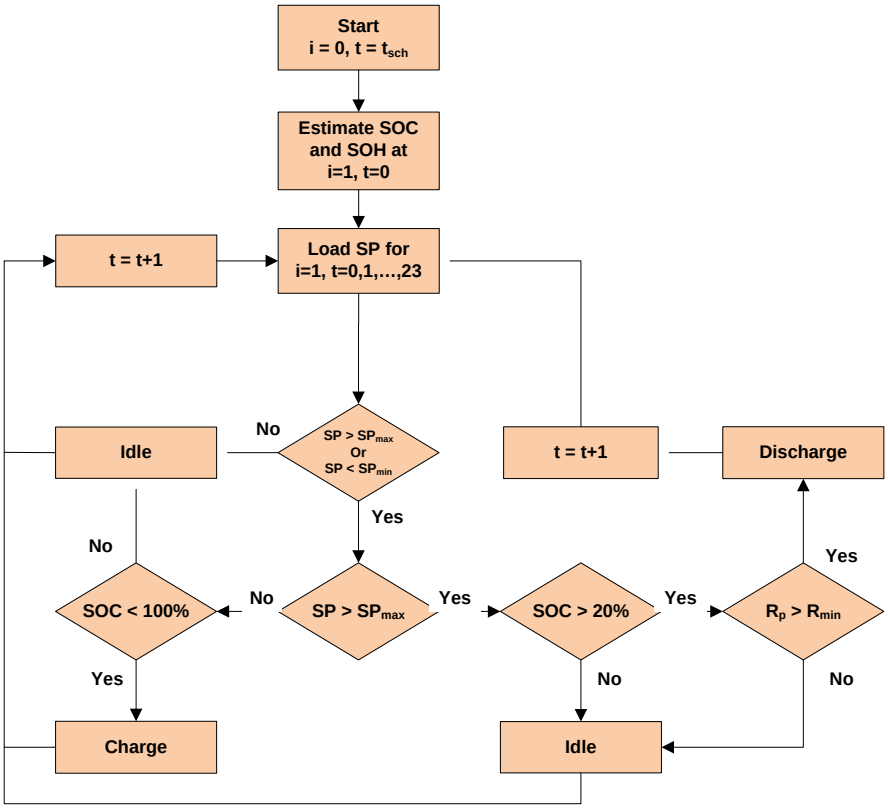

Figure 2.9: Flowchart of the economic-based scheduling operation strategy of the MSS.

The lower and upper cutoffs ($SP_{\min}$ and $SP_{\max}$) of the spot market electricity prices can be calculated on daily basis as given in (2.12) and (2.13).

$$SP_{\min}(k) = \text{Max}\left(\overline{SP_{\text{L}}}(k)\right)\Big|_{i=k-6,\ldots,k} \tag{2.12}$$

$$SP_{\max}(k) = (p_{\text{diff}})_{\min} + SP_{\min}(k) \tag{2.13}$$

$$(p_{\text{diff}})_{\min} = (L_N{}^{-1}).(1 \text{ cycle}) \tag{2.14}$$

where k refers to the day, $\overline{SP_{\text{L}}}$ is the average off-peak price between 12:00 AM and 6:00 AM ($SP_{\text{L}} \leq SP_{\min}$) and $(p_{\text{diff}})_{\min}$ is the minimum differential price at which the system starts paying back (ROI = 0%). During online operation, the goal is to match the scheduled plan for power exchange, i.e. $P_E(t) = \hat{P}_S(t)$, where P_E is the power delivered to the grid, and $\hat{P}_S$ is the estimated

(forecasted) power supplied by the MSS. The operation of the MSS can be explained through an example. Considering a 3kWh, 750W MSS with a total cost of $1,000 and a cycle-life of 5,000 cycles at DOD = 80%. Assume $SP_{\min}$ = 0.09 $/kWh, $SP_{\max}$ is obtained from Equation (2.13).

$$SP_{\max}(k) = L_N^{-1} + SP_{\min}(k) = \frac{1{,}000}{5{,}000} + 0.09 = 0.29 \text{ ($/kWh)}$$

Assume further that the system's discharge capacity is 70% of its initial value (D = 0.7), where D is given in Equation (2.9). Since the discharge capacity is at 70% of its initial value, then, the effective capacity is (0.7)(3kWh) = 2.1 kWh.

If the on-peak and off-peak electricity prices of $0.351/kWh and $0.079/kWh were adopted from [27], where the prices at other hours were logically assumed based on price curves from [19] and [20], the operation of the system (efficiency of (dis)charge is assumed to be 100%) will be as summarized in Table 2.5, where E is the energy exchanged with the utility, and R_p is the predicted return which is calculated as follows:

$$R_p = SP_H(i)\,E(i)$$

where SP_H is the on-peak spot price ($SP_H \geq SP_{\max}$).

Table 2.5: An example of the operation of the system.

Hour	*SP*	*E*	R_p	*State*	*Hour*	*SP*	*E*	R_p	*State*
00	8.8	−0.42	N/A	Charge	12	24.9	0	N/A	Idle
01	8.3	−0.42	N/A	Charge	13	27.2	0	N/A	Idle
02	8.2	−0.42	N/A	Charge	14	30.9	+0.42	0.13	Discharge
03	7.9	−0.21	N/A	Charge	15	33.2	+0.42	0.139	Discharge
04	8.0	−0.07	N/A	Charge	16	35.1	+0.42	0.147	Discharge
05	8.2	−0.07	N/A	Charge	17	33.2	+0.42	0.139	Discharge
06	8.8	0	N/A	Idle	18	28.1	0	N/A	Idle
07	9.3	0	N/A	Idle	19	25.1	0	N/A	Idle
08	11.4	0	N/A	Idle	20	23.3	0	N/A	Idle
09	14.6	0	N/A	Idle	21	21.3	0	N/A	Idle
10	17.1	0	N/A	Idle	22	14.6	0	N/A	Idle
11	21.3	0	N/A	Idle	23	11.4	0	N/A	idle

Note that in Table 2.5 a negative E indicates charging operation, while a positive E indicates a discharging operation. To find an expression for $R_{\min}$, the charging cost as well as the battery cycling (degradation) cost must be considered. Since the discharging time is constant, which is four hours based on our previous analysis, the return in one hour must be greater than a minimum threshold. To meet these constraints, the average of the total charging cost and the normalized cycle-life, L_{N}, including the SOH factor over four hours are considered. Accordingly, the minimum hourly return, $R_{\min}$, is:

$$R_{\min} = \frac{1}{4}\left(\sum_{i=0}^{6} SP_{\mathrm{L}}(i)E(i) + 2 \times D \times \frac{1}{L_{\mathrm{N}}} \right) \tag{2.15}$$

$$= \frac{1}{4}\left(0.134 + 2 \times 0.7 \times \left(\frac{1{,}000}{5{,}000} \right) \right)$$

$$= \$\ 0.1035$$

If $R_p \geq R_{min}$, the system will initiate a discharge cycle, otherwise, the system will be in the idle state. When the battery is new (D = 1), the expected profit will be high and hence R_{min} will be high (second term inside the brackets is equal to $2/L_{\mathrm{N}}$). As the battery ages, the expected return decreases until the battery reaches its end of life (D = 0.5) where the return will be low (second term inside the brackets is equal to $1/L_{\mathrm{N}}$).

2.8 Conclusions

This chapter covered some design aspects of distributed grid-tied micro-storage systems. These aspects included hardware design and economic aspects. The hardware design can be optimized by choosing a proper system architecture, operating the system at its rated power, and selecting a cost-effective storage technology. The economic aspects, on the other hand, were

discussed through the development of static and dynamic economic models. These economic models were developed for two reasons; to find the economic feasibility of any MSS in general, and to maximize the economic return of the system when operating in real-time.

The main obstacle for those systems is the high cost of the energy storage. However, since the cost of energy storage devices are expected to continuously decrease, and due to the continuously increasing demand and prices of electric power, distributed micro-storage is expected to gain more attention in the coming years.

CHAPTER THREE: BATTERY MANAGEMENT SYSTEM - PART 1: BATTERY CHARGING

3.1 Introduction

A basic task of a BMS is to offer a reliable and safe charging operation. The objective of this chapter is to introduce some charging techniques for nickel and lithium batteries. These techniques can be implemented in different battery chargers to accommodate a wide range of applications.

The scope of this chapter is to introduce battery charging in an unconventional way through a comprehensive analysis of some recent battery chargers' algorithms. These algorithms are compared in terms of their charging schemes and charge termination techniques. This work also presents some charging basics and challenges, and proposes ways to overcome some chargers' limitations, which can be indeed a useful guideline tool for practicing engineers.

3.2 Background

Rechargeable batteries were first introduced in 1859 when the first rechargeable lead-acid battery was invented by the French inventor Gaston Plante [28]. Lead-acid batteries are used in several applications where cost is more important than space and weight, typically preferred as backup batteries for uninterruptable power supply (UPS) and alarm systems, as well as automotive lighting and ignition applications. Almost four decades beyond this invention, the NiCd battery was invented and widely used in low-power applications. One major limitation of NiCd batteries is the "memory effect" phenomenon, which is a term used to describe the

degradation in the battery capacity when it is partly charged and discharged. In addition, because of the cadmium element, these batteries are not environmentally friendly. Then, in the 1990s, NiMH and Li-ion batteries were invented and commercialized. These batteries have higher energy and power densities compared with lead-acid and NiCd batteries and do not suffer from the memory effect. In particular, Li-ion batteries have the highest energy/power density, life-cycles, as well as the highest cost.

According to [29], battery charging is the most substantial issue in battery management systems. Basically, a charger has the following three functions: 1) delivering charge to the battery; 2) optimizing the charge rate; and 3) terminating the charge. The charge can be delivered to the battery through different charging schemes, depending on the battery chemistry. For example, nickel batteries require only constant current (CC), whereas Li-ion batteries require constant current/constant voltage (CC/CV). The charge rate can be optimized if the capacity and the SOC are given. As an example, a completely discharged or a fully charged battery must be trickle charged with a very low current (a fraction of the "capacity rate", or *C*-rate, which is defined as the maximum current that can be delivered by a fully charged battery in one hour) to extend the battery life. In addition to CC and CC/CV charging schemes, pulse charging, which uses a pulse current for up to one second, followed by a rest period and a discharge pulse for milliseconds, is claimed to be optimal, because it improves the charging speed and efficiency [30]. With regard to the charge termination, different techniques are used, such as the voltage drop and temperature rise in nickel batteries or the inflection* point in both nickel and lithium batteries. As a result of the diversity in battery systems and their applications, charging algorithms are, accordingly, also

*Inflection point: The point at which the sign of the second derivative of the voltage-time curve changes; or the point at which the first derivative of the voltage-time curve is zero.

found to be diverse. For example, some algorithms are suitable for solar chargers [33], [39]. Other algorithms are suitable for single-chemistry chargers [31]-[37], whereas other algorithms are suitable for multichemistry chargers [39]-[41]. All these algorithms are discussed and evaluated in the rest of this chapter.

3.3 Single-chemistry Algorithms

Single-chemistry chargers are very common and are used in most battery systems. In this section, some charging algorithms for single-battery chemistries are discussed.

3.3.1 NiCd/ NiMH Batteries

Because NiCd and NiMH single cells have the same cutoff voltages and the two battery types share almost the same performance during charging, they can be charged with the same charger. However, the charge termination method might be different for these batteries, which will be discussed later.

In [31], a NiCd/NiMH charging algorithm is proposed (see Figure 3.1). A CC is used during charging until an inflection point is detected. Once an inflection point is detected, the charger switches to trickle charging to prevent overcharging the battery. Other charge termination techniques are implemented in this algorithm, e.g., voltage drop, temperature rise, and timing, to improve the charger performance.

Another charging algorithm is proposed in [32], which offers three charging stages. The algorithm is constructed from multiple statements. First, the voltage across the battery is sensed, and based on its value, an action is taken. For NiCd and NiMH battery packs, the voltage of each

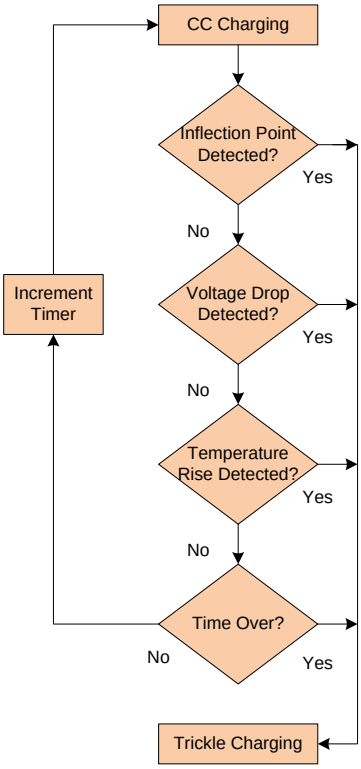

Figure 3.1: The algorithm proposed in [31].

individual cell is found to be between 0.2 V and 1.6 V; otherwise, the battery is over (dis)charged. Within this range, the battery is charged with a relatively high current (fast charging) or low current (trickle charging) based on its voltage and temperature. When the battery voltage approaches 1.6 V, a trickle current is applied to the battery until it is removed from the charger.

Another algorithm is proposed in [33] for solar NiCd/NiMH battery chargers (see Figure 3.2). The algorithm continuously tracks the maximum battery voltage and calculates the derivative of the voltage and the variation in the current in a sliding window of 5-10 min. The maximum voltage and the voltage drop will reset if at least the variation in the current or the derivative of the voltage exceeds some predefined threshold values. Otherwise, the charging continues until a significant voltage rise ($dV/dt > Thsld_3$), followed by a voltage drop above a certain threshold, occurs.

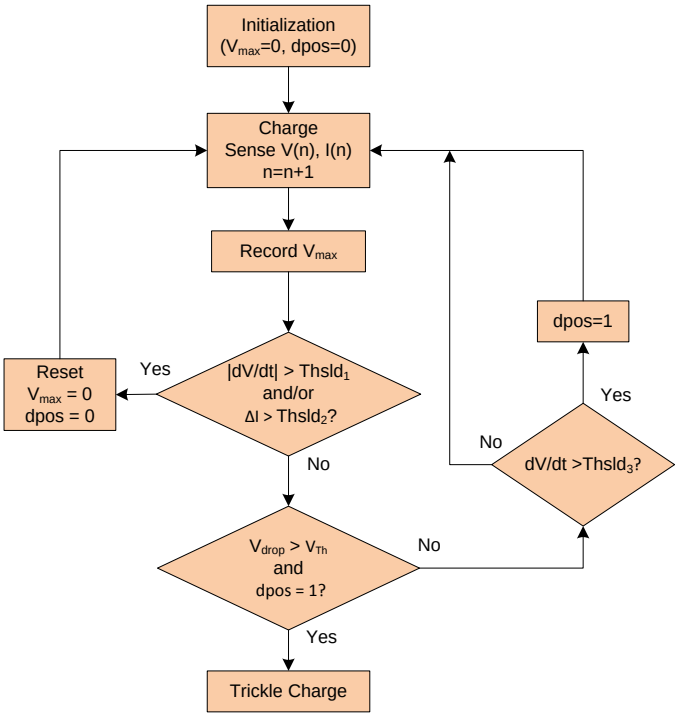

Figure 3.2: The "voltage-based" algorithm proposed in [33].

In the same work in [33], another algorithm is proposed (see Figure 3.3). The concept of this algorithm is to divide the battery into two legs inside the battery pack and individually monitor the temperature of each leg. Ideally, the difference in temperature between the two legs must be negligible during charging, regardless of whether the ambient temperature changed. If a high positive temperature derivative is detected in one of the legs, the charger will keep charging this leg, whereas it stops charging the other leg. After a certain time, if the temperature derivative reaches a predefined threshold, then the algorithm will detect overcharge in that leg.

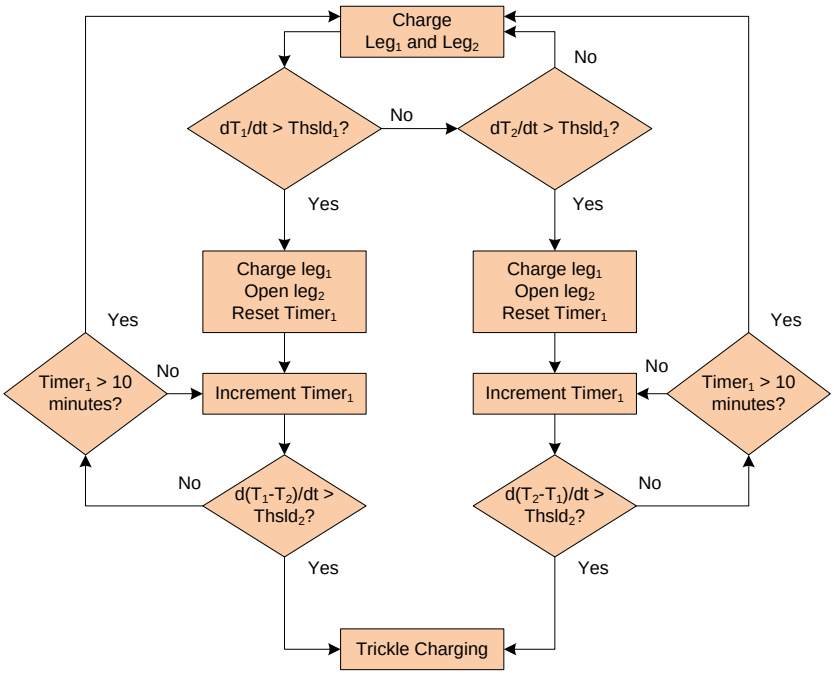

Figure 3.3: The "temperature-based" algorithm proposed in [33].

Another NiCd/NiMH charging algorithm is given in [34], in which the capacity of the battery must be provided. Charging starts by sensing the initial open-circuit voltage (OCV) to determine the battery SOC. In the first case, where the OCV is below 1 V/cell, the charger will inject a current of 0.1*C* (*C* represents the capacity of the battery in ampere-hours) to charge the battery for 5 min. After the injection of the 5-min 0.1*C* current, if the battery voltage was below 1.25 V/cell, this battery will be interpreted as damaged, and the charging will end. If the voltage was more than 1.25 V/cell after the 5-min 0.1*C* current injection, a fast charging current will charge the battery until it becomes fully charged. In the second case, if the OCV was more than 1 V/cell, then, depending on this value, the battery will be in one of the following three states: 1) fully charged; 2) half charged; or 3) discharged. If the battery was discharged, it will initially be trickle charged to avoid damaging it with a high current. If the battery was half charged, it will initially be discharged and then charged to protect the battery from memory effect.

A different algorithm is proposed in [35], which utilizes the pulse-charging technique to charge NiCd and NiMH batteries. First, the battery initial OCV is sensed to determine the SOC of the battery. Based on the measured OCV, the battery is defined as one of the following three states: 1) fully charged (SOC > 80%); 2) half charged (10% ≤ SOC ≤ 80%); or 3) discharged (SOC < 10%). The charger measures the battery voltage, current, and temperature during charging. This method can support NiCd and NiMH of (0.6-, 0.9-, 1.2-, and 2-Ah) capacities as reported and requires the user to provide the battery capacity to the charger. If the temperature exceeded a certain range three times, charging will be halted, and the battery is considered damaged.

3.3.2 Li-ion Batteries

Li-ion batteries have very critical charging requirements that must be met during charging to ensure preventing overheating and overcharging these batteries. Li-ion batteries are charged with a CV with a current limiter to prevent overheating in the initial stage of the charging. One special requirement for Li-ion chargers is to monitor the voltage across each cell when more than one cell is in a string (connected in series) to ensure charge balance and voltage equalization of the cells [43]. A protection circuit is usually added to the charger circuit to handle these functions.

A Li-ion battery-charging algorithm is proposed in [36] (see Figure 3.4). In this algorithm, the temperature is constantly monitored during charging. Charging starts by measuring the initial OCV of the battery. If the value lies between 2.9 V/cell and 4.2 V/cell, charging with a current of 0.7*C* will hold until the upper voltage limit or a timeout is reached. Then, the CV mode starts until either the current drops below a threshold value or a timeout is reached. If the initial OCV was below 2.9 V/cell, charging with a current that is as low as 0.1*C* will sustain until the OCV reaches

3 V/cell, at which fast charging current of 0.7*C* will be applied. If the temperature during charging deviates from a certain range, the battery will be disconnected until its temperature returns to the defined range. The charging will automatically be terminated after reaching a predefined time for safety.

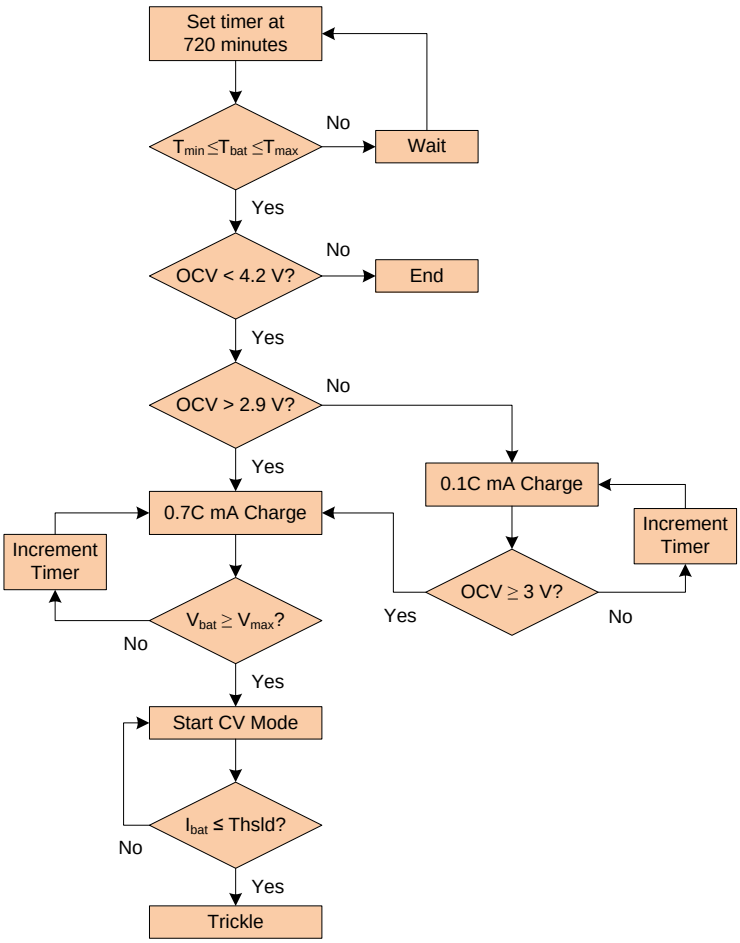

Figure 3.4: The algorithm proposed in [36].

A similar algorithm is proposed in [37]. First, the OCV of the battery pack is sensed to check whether the battery is fully charged. If the battery is not fully charged, then the OCV of each individual cell is measured to check if the cells are unbalanced. The algorithm detects the unbalanced cells and fixes them before charging starts by discharging the overcharged cells until

the difference in voltage between the highest and the lowest cell voltages returns to an acceptable value below 0.1 V. Charging with CC will start when all cells' voltages are balanced and the temperature is in a predefined range until the upper safety voltage limit is reached. Then, the CV mode will start until the current drops to a threshold value at which charging will be terminated. In this algorithm, the battery module must be provided. During charging, if the voltage or temperature escaped the normal range, charging will be interrupted, and this condition will be interpreted as an error.

3.4 Multi-chemistry Algorithms

Due to the wide variety of portable appliances, ranging from toys and pocket lights to cell phones and personal digital assistants (PDAs), several chargers that can accommodate these enormous differences in applications have recently been developed. In multichemistry chargers, the main challenge is to detect the battery type and size to select the charging scheme and cutoffs. Therefore, these chargers require some techniques implemented in the controller to identify the battery and to ensure reliability and safety during charging. The discussion in this section includes some algorithms for nickel and lithium batteries. Although these algorithms can charge lead-acid batteries as reported, these batteries will be excluded from the discussion.

In [39], a solar battery charger algorithm is proposed to charge different batteries (see Figure 3.5). The concept of interrupted charge control (ICC) used in [38] for standby applications was employed in [39] for bulk charging. The battery is charged with current pulses at a duty cycle of 50% to increase the accuracy of the voltage measurement at the end of each rest cycle. As reported, the charger speed can be improved when two batteries are simultaneously charged, because all the solar power is utilized to charge each battery in its charge cycle. The charger

charges the battery with the current that was obtained from the solar array for 3 min (charge cycle) and disconnects the battery for another 3 min (rest cycle). The voltage at the end of each rest cycle is monitored and compared with the previous value. If the voltage increases, the algorithm checks if the voltage is within a predefined Li-ion range. If the voltage is not in one of the predefined ranges, charging will continue. The voltage drop is also monitored at the end of each rest cycle. If a voltage drop that is greater than a threshold value is detected, charging will be terminated, and the battery will be either a NiCd or a NiMH battery. If no voltage drop was detected and the battery voltage at the end of a rest cycle was in the safety limit range of Li-ion battery, the CV mode will start, and the current will be monitored until it drops below a threshold value at which charging will be terminated, and the battery will be Li-ion.

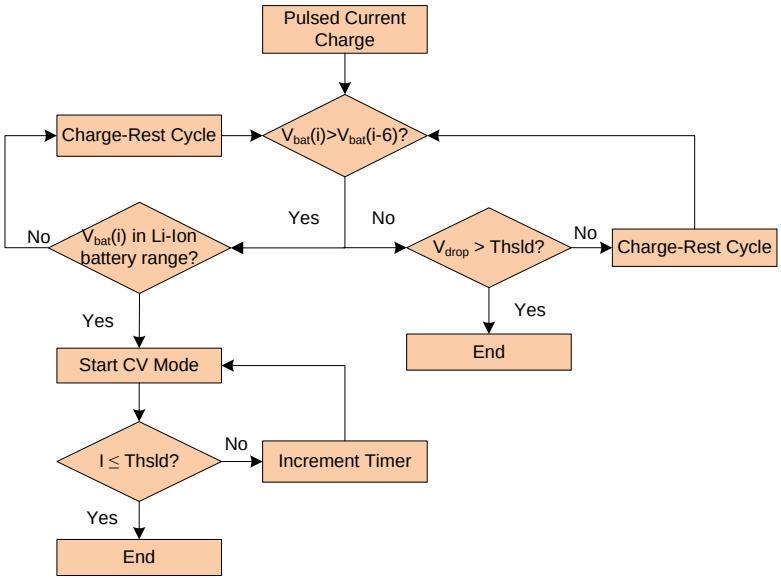

Figure 3.5: The algorithm proposed in [39].

In [40], another multichemistry charging algorithm is proposed. A lookup table of open-circuit voltages of different possibilities of battery cells was established. First, the charger senses the OCV of the battery and compares it with the values in the lookup table. A possible safety limit

voltage of a Li-ion battery is set to prevent damage in case of a Li-ion battery. Once the safety limit voltage is set, CC charging starts. During the CC mode, the “hysteresis measurement” test is performed to detect the battery chemistry. In this test, a discharge pulse of 2-A is applied to the battery for 30 s, and then, the battery is recharged with a 2-A pulse for another 30 s. If the difference in the OCV of the battery after the discharge pulse and the charge pulse was greater than a minimum threshold, then the battery will be either NiCd or NiMH. Therefore, if a nickel battery was detected, charging with a CC will proceed until a voltage drop occurs, at which time charging is terminated. If the battery chemistry was not detected from the hysteresis test, the charger will assume a Li-ion battery, and the CC mode will hold until the battery voltage reaches a predefined safety limit. If a voltage drop occurred before the safety limit is reached, charging will be terminated (a NiCd or a NiMH battery); otherwise, the CV mode will start and hold until the current drops below a threshold value.

Another multichemistry algorithm that uses the concept of the inflection point to identify the battery chemistry is proposed in [41] (see Figure 3.6). In this algorithm, the battery is charged with a CC. The battery voltage and its first derivative are recorded at each time step. As reported in this paper, for NiCd and NiMH batteries, the peak voltage before the voltage drops is 6%-7% above the inflection point, whereas for Li-ion batteries, the upper voltage limit is around 10% above the inflection point. Based on this concept, the algorithm was designed to charge with a CC until either a voltage drop is detected (at about 6%-7% above the inflection point) or the voltage goes 10% above the inflection point, with no voltage drop detected, at which the CV mode starts until a predefined current drop is reached.

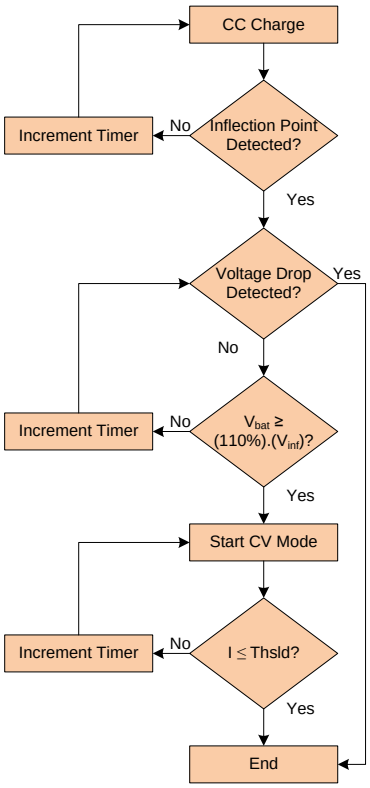

Figure 3.6: The algorithm proposed in [41].

3.5 Discussion on Reviewed Algorithms

The discussed charging algorithms incorporate simple techniques for managing the charging process, which may result in a possible overcharge or incomplete charge. This section discusses the capabilities of the reviewed algorithms through some test results. To compare and evaluate the discussed algorithms, some charging tests were performed on commercial NiCd, NiMH, and Li-ion single cells with capacities of 1200, 1000, and 1100 mAh, respectively. The cells were completely discharged and then completely charged. Figure 3.7 shows the results followed by a discussion (the horizontal axis represents the SOC, rather than time, for an in-depth evaluation).

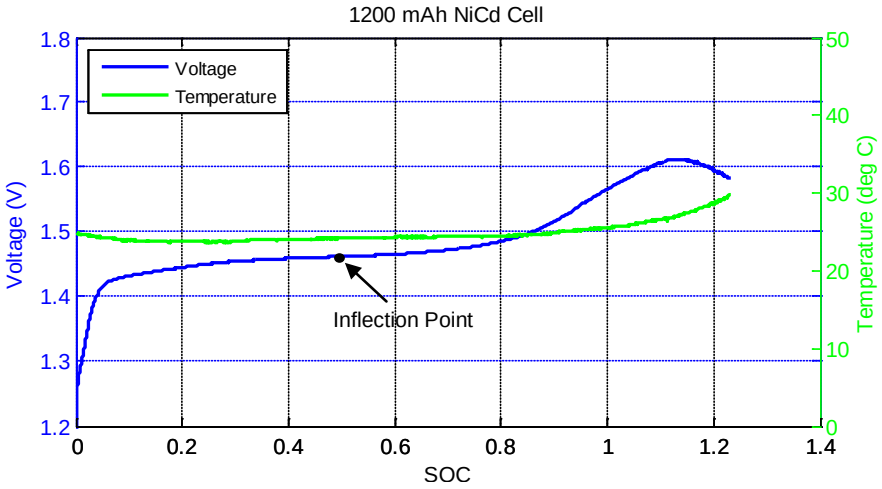

(a) NiCd battery cell charging profile

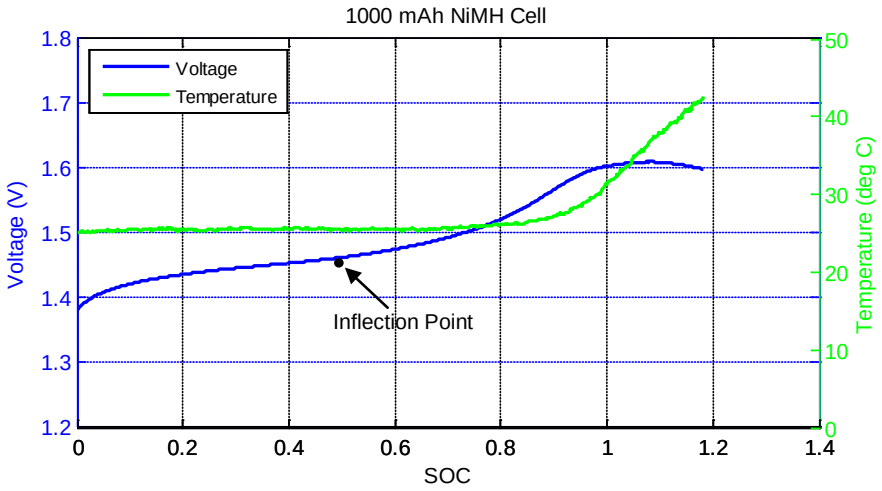

(b) NiMH battery cell charging profile

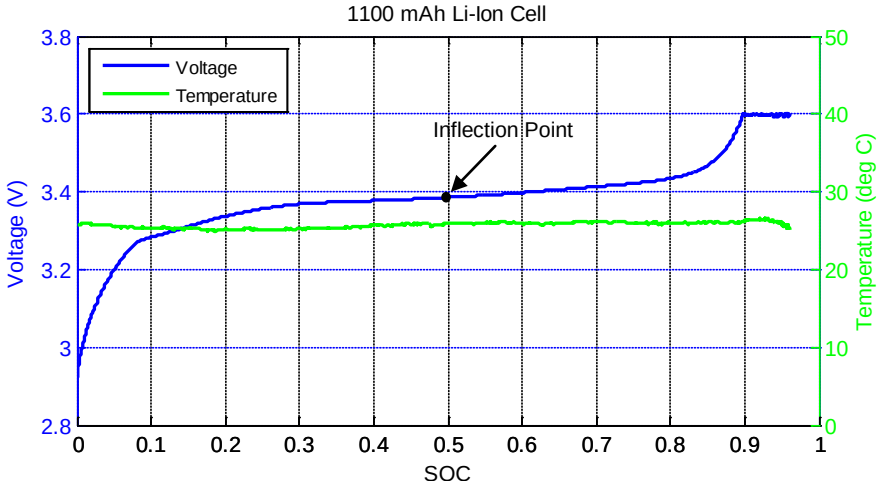

(c) Li-ion battery cell charging profile

Figure 3.7: Voltage and temperature profiles for charging (a) NiCd, (b) NiMH, and (c) Li-ion cells.

3.5.1 Charging Process

In the reviewed algorithms, different control and measurement techniques were used during charging. The following discussion compares these techniques and points out their advantages and limitations.

3.5.1.1 Charging Method

The charging methods employed in the discussed algorithms are mainly trickle, CC, and CC/CV. Trickle charging uses a very low current of a magnitude around 0.1 C to precharge a completely discharged battery (see [32] and [34]-[36]) or to sustain the charge in a fully charged battery (see [31] and [33]-[37]). A discharged battery is normally trickle charged for a short time to extend its life. On the other hand, CC and CC/CV are usually used for bulk charging. NiCd and NiMH batteries require only CC, whereas Li-ion batteries require CC until the battery voltage reaches a predefined safety limit at which CV begins. CV charging is used in Li-ion batteries to limit the current and thus prevent the battery from overcharge. Results in Figure 3.7 show CC charging [see Figure 3.7(a) and (b)] and CC/CV charging [see Figure 3.7(c)].

The concept of ICC was used in [39] for bulk charging with a duty cycle of $D = 0.5$ and ON time Ton = 3 min. The advantage of this method in solar chargers, where the battery voltage varies during charging according to the current (or illumination) variations, is simply to let the battery rest for some time to stabilize its voltage. The drawback of this method is the long time that it takes to charge the battery if only one battery is connected to the charger.

In addition, the pulse-charging method was used in [35]. In contrary to the ICC method (see Figure 3.8), where only positive pulses are injected, in pulse charging, positive and negative

current pulses are injected [35]. According to [30], pulse charging offers an optimum charging, because it was developed after the chemical reactions that occur inside the battery during CC charging were studied. The main obstacle of this method is that most chargers are unidirectional, i.e., the current can flow only in one direction. To implement this method, an advanced charger with bidirectional current flow capability must be used, which might significantly increase the charger cost.

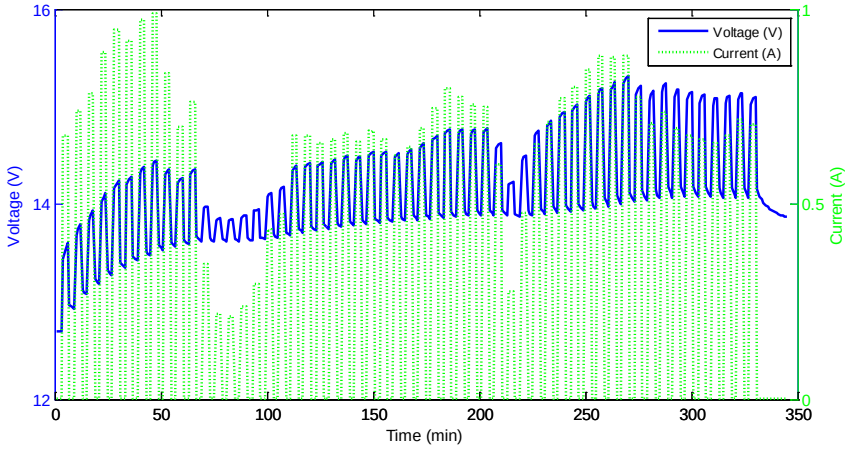

Figure 3.8: The ICC charging method in [39].

3.5.1.2 Temperature Control

The chemical reactions that occur inside the battery during charging produce heat. This heat increases the pressure and the temperature of the battery pack. If the battery temperature exceeds a certain value, this condition can be interpreted as a fully charged battery or a battery failure. In either case, the charger must switch to the trickle mode to protect the battery until the temperature drops to a predefined range. In [31], if a temperature rise is detected, the charger switches to the trickle charging mode until the battery is removed from the charger. This simple technique can save the battery life, at the cost of extending the charging time. In [32], the charger keeps monitoring the temperature during charging, and if the temperature deviates from a

predefined range, the charger will either switch from fast charging to trickle charging or show a "fault" statement until the normal temperature range resumes. The same concept was used in [35]-[37].

3.5.1.3 Battery Type Identification

The identification of the battery type is exclusive for multichemistry chargers. In [40], once the OCV is measured, the algorithm allocates a possible Li-ion battery and accordingly sets a safety limit voltage. Then, the "hysteresis measurement" is performed to determine whether the battery is a nickel-based battery. According to [40], the hysteresis phenomenon was reported as a distinct feature for nickel batteries. In fact, this phenomenon was also observed in Li-ion batteries. Figure 3.9 shows the hysteresis in a Li-ion cell over the entire SOC range, which was found by calculating the difference in voltage between charging and discharging voltages at *C*/30 rate (neglecting the voltage drop). Therefore, the "hysteresis measurement" proposed in [40] is insufficient to distinguish between nickel and lithium batteries.

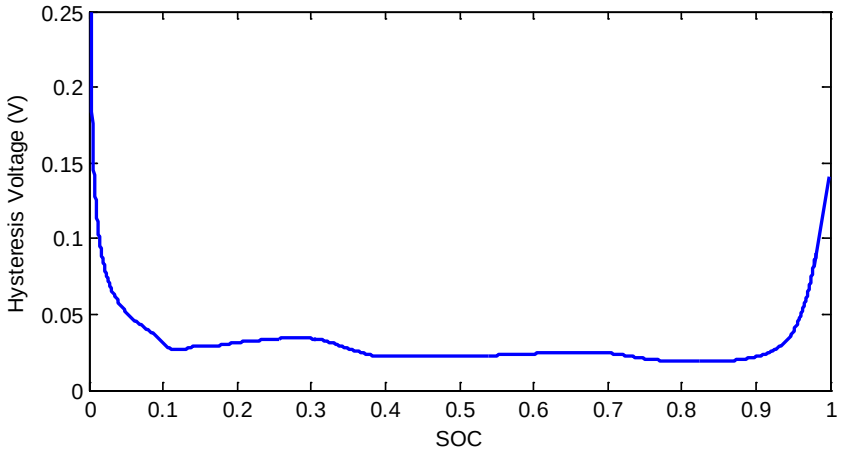

Figure 3.9: Hysteresis in a Li-ion cell over the entire SOC range.

In [41], the charger identifies the battery chemistry slightly after the inflection point is detected. That is, if a voltage drop occurs before the voltage reaches 110% of the inflection point voltage, the battery will be either NiCd or NiMH. Otherwise, the battery is determined as Li-ion. To verify this concept, different charging tests at different currents were performed on the cells. The results showed that this concept is valid only if low currents (i.e., below *C*/2) are used. For example, the Li-ion cell was charged at *C* and *C*/25 rates. In the first case [see Figure 3.7(c)], the inflection point was at 3.38 V, whereas in the latter case, it was 3.28 V [charging curve in Figure 3.9(b)]. According to this concept, the CV mode will start when the voltage reaches 3.718 V in the first case (overvoltage) and 3.608 V (correct voltage) in the second case. With regard to the

NiCd and NiMH cells, the same case was observed. At low charging rates, the peak voltage immediately before the voltage starts dropping was below 110% of the inflection point voltage, and in this case, the battery chemistry can be predicted. In practice, as the charging rates increase, the peak voltage accordingly increases due to increased internal voltage drop in the cell. In Figure 3.7(a) and (b), the inflection point voltage and the peak voltage were 1.463 and 1.61 V, respectively, in both cases (*C*/2 and 3*C*/4 rates were used). Based on this discussion, the inflection point concept can be applied to distinguish between nickel and lithium batteries, but to avoid overcharging a possible lithium battery, the charging rate must be low.

3.5.1.4 SOC Estimation

In [32], [34]-[37] and [40], the initial SOC was predicted based on the value of the OCV. If a good estimation of the initial SOC was obtained, the performance of the charger can be improved. In practice, the accuracy of the SOC estimation from the OCV value is not guaranteed, unless the battery relaxes for a long time. Furthermore, even if the battery relaxed for a long time,

its OCV will not converge to its true value (at a certain SOC) due to the hysteresis, which means that the cell voltage relaxes to a value greater than the OCV for a given SOC after charging, and relaxes to a value that is less than the OCV of that SOC after discharging. In advanced battery management systems, the estimation of the SOC is substantial and must be very accurate as opposed to portable appliances, for example. If an accurate SOC estimation is required by an application, some techniques such as extended Kalman filters (EKFs) can be used for this purpose if an accurate battery model is provided as will be shown in Chapter 4.

3.5.2 Termination Techniques

Different charge termination techniques were used in the discussed algorithms. These techniques are discussed and evaluated in the following discussion.

3.5.2.1 Voltage Drop

The voltage drop that occurs in nickel batteries, which is more obvious in NiCd, is due to the drop in the battery internal resistance when it becomes fully charged. In Figure 3.7(a) and (b), the charging was terminated when a voltage drop of 30 mV occurred in the NiCd cell and 10 mV in the NiMH cell.

In NiCd and NiMH batteries, the detection of a predefined voltage drop can be used as an indication to terminate charging, as shown in [31], [33], and [39]-[41]. In [33] and [39], the concept of voltage drop was used, but with a slight modification, to overcome the voltage drops when the solar power drops. The limitation of this method in solar chargers is the random variation in the power supplied to the charger, which affects the reliability of the charger if only

this technique is used. However, using this method alone is not recommended, because it will certainly overcharge the battery. Figure 3.7(a) and (b) shows that the SOC was around 120% when the voltage drop was detected. This case can significantly reduce the battery lifetime.

3.5.2.2 Inflection Point

The concept of the inflection point is sometimes used as an indication that the battery is almost half charged. In Figure 3.7(a)-(c), the inflection point occurred when the SOC approached 50%. In [31], the charger switches to trickle charging when the inflection point is detected. This method requires very stable charging conditions such as CC and temperature to very precisely allocate the inflection point to avoid overcharging or partially charging the battery.

3.5.2.3 Temperature Rise

In the tests in Figure 3.7, the temperature rise was 6^{o} C for the NiCd cell (from 24^{o} C to 30^{o} C) and 17^{o} C for the NiMH cell (from 25^{o} C to 42^{o} C). For the Li-ion cell, the results show almost a constant temperature during the entire range of SOC. The sudden rise in temperature, which is more obvious in NiMH cells, is a result of the undesired gases that were produced when the battery became fully charged. This unique phenomenon in NiMH batteries was employed to terminate charging (see [31] and [33]). In the temperature-based algorithm that was proposed in [33], the algorithm monitors the temperature rise of each leg and the differential temperature between the two legs. This method was proposed for solar NiMH chargers to overcome the swing in the ambient temperature under outdoor conditions.

3.5.2.4 Timing

As a safety procedure, some chargers add a timer to terminate charging if a predefined timeout is reached [31], [36]. This method is very simple but can be advantageous if the charger did not detect a full charge status. However, this method cannot be used without the support of other methods.

3.5.3 Summary of Reviewed Charging Algorithms

A good charger must extend the battery lifetime by properly charging it. In applications where a crude SOC prediction is acceptable, e.g., in portable electronics, a simple charger with the trickle-CC-CV charging scheme is sufficient to maintain a proper operation. In outdoor environments where the ambient temperature can widely change, the charger must accommodate these variations in temperature while ensuring a proper operation. In environments where temperatures and charging rates are unexpected and can considerably change in a short time, as for the MSS charging system, more advanced techniques must be used alongside with the discussed charging techniques. If a dynamic SOC estimation of an application is not urgent, the variation in temperature and charging rates can be overcome by employing techniques as proposed in [33] and [39]. If a dynamic tracking of the SOC is desired, which is the case for the proposed MSS, an advanced BMS must be designed. One very effective way of overcoming the challenges associated with the temperature and current variations is to design a BMS with a very accurate battery model (will be discussed in Chapter 4) to dynamically estimate the SOC. The battery model, regardless of how accurate it is, can be integrated with other charging algorithms to optimize the charger performance and reduce the possibility of overcharging the battery. As a summary, the capabilities of the reviewed algorithms are listed in Table 3.1.

Table 3.1: A summary of the reviewed algorithms.

Algorithm Reference	*Supported Batteries*	*Charging Profile*	*Strengths*	*Limitations*
31	NiCd, NiMH	CC-trickle	Different charge termination methods (very reliable)	Charge rate is not optimized
32	NiCd, NiMH	trickle-CC-trickle	Charge rate is optimized	Charge termination is based only on the cell voltage measurement
33 (Fig. 3.2)	NiCd, NiMH	CC*-trickle	Supports solar chargers	Temperature is uncontrolled
33 (Fig. 3.3)	NiCd, NiMH	CC*-trickle	Supports solar chargers	Battery pack must be separated into two legs
34	NiCd, NiMH	trickle-CC-trickle	Charge rate is optimized, memory effect is minimized	Temperature is uncontrolled
35	NiCd, NiMH	trickle-pulse-trickle	Charge rate is optimized, memory effect is minimized	Requires bidirectional charger for the (dis)charge pulses, support limited sizes
36	Li-ion	CC-CV-trickle	Charge rate is optimized	Temperature is uncontrolled
37	Li-ion	CC-CV-trickle	Cells are equalized	Charge rate is not optimized
39	NiCd, NiMH, Li-ion	ICC-CV**	Supports solar chargers, support multiple chemistries	Unreliable for small NiMH batteries, support limited battery sizes
40	NiCd, NiMH, Li-ion	CC-CV	Supports multiple chemistries	Battery detection is unreliable, temperature is uncontrolled
41	NiCd, NiMH, Li-ion	CC-CV	Supports multiple chemistries	Requires very stable current and temperature, currents must be low

3.6 Trend of Recent Developments

Reliability and ease of implementation are key issues in all battery management systems, regardless of the application for which they are designed. Some recent trends of battery chargers are discussed here.

3.6.1 Reliability

Reliability in battery chargers is referred to the capability of terminating charging once a

* Solar current is variable and is a function of illumination. However, it was considered as CC only for comparison with other algorithms.
** The CV mode in solar chargers is not guaranteed because solar power is variable.

SOC of 100% is detected. This condition can be achieved through different charge termination techniques or by implementing advanced techniques, e.g., the Kalman filter, to contentiously estimate the SOC. Preventing overcharging the battery has a great impact in extending the battery lifetime and utilizing the entire battery capacity.

3.6.2 High Efficiency

The large amount of heat that is generated inside the battery during charging is an indication of a poor charging efficiency, which can reduce the battery capacity and lifetime. The charging efficiency can be increased by addressing the chemical reactions inside the battery, e.g., the pulse charging method [30]. Hence, improving charging methods according to the thermochemical behavior of the battery results in an increased efficiency, which, as a result, improves the charging speed and extends the battery lifetime.

3.6.3 Universality

As a result of the wide diversification in battery types and sizes due to the wide range of applications, a recent trend toward universal chargers has been observed [42]. Universal chargers may or may not require previous information about the battery pack prior to charging. The capability of autodetecting the battery chemistry and the number of cells with no information provided is a desired feature. This feature can be achieved by addressing the different responses of the different battery chemistries when biased to some external signals.

3.7 Conclusions

Some charging techniques and challenges for nickel and lithium batteries were overviewed in this chapter. The algorithms reviewed in this chapter, which can accommodate a wide range of applications including the proposed MSS, were evaluated through some real tests on commercial battery cells. This evaluation showed the strengths and weaknesses of these algorithms, with an experimental verification, and proposed some directions for further improvement.

Depending on the battery chemistry, environment and application nature, the charging algorithm and termination technique are selected. However, all the discussed algorithms rely on the terminal measurements only such as the battery voltage and temperature to manage the battery charging, which can lead to some issues in certain applications. In the next chapter, some techniques that allow the BMS to better manage the battery by estimating its inner states are proposed.

CHAPTER FOUR: BATTERY MANAGEMENT SYSTEM - PART 2: BATTERY MODELING AND STATES ESTIMATION

4.1 Introduction

The BMS performance can be enhanced by implementing advanced techniques alongside with the battery charging algorithm especially when the battery cost is considerably high, or if the battery's environment is harsh (wide range of temperatures and/or wide range of dis/charge current rates). To enhance the performance of the BMS, an advanced battery model must be implemented to closely monitor the battery behavior. In this chapter, a battery model with improved output compared to some existent models is proposed. The model parameters are found at a wide range of temperatures ranging from -30^{o} C to 50^{o} C to validate the model at all possible temperatures. The model is then used to estimate the SOC and SOH of the battery in real-time using EKFs.

4.2 Available Battery Models

Many battery models were discussed in the literature, each of which has its advantages and drawbacks. For example, in [44], an electrochemical battery model is proposed. The main problem with such models is the difficulty to implement these models in dynamic systems since they require tedious measurements which can be performed only in the laboratory. The models in [45]-[52] rely on the concept of equivalent circuit, where the cell's dynamics are interpreted through an equivalent circuit model. Although many of these models are very precise, some require massive computations to extract their parameters as in [52], and others don't include the

cell's hysteresis and relaxation* effects [45]-[51]. Other mathematical models in [53] are simple models but are inaccurate and unsuitable for many applications. In this section, some existent models are reviewed.

4.2.1 Electrochemical Models

These models are usually used at the battery design level. Practically, these models are unsuitable to be used to simulate and predict the cell's behavior in a dynamic operation as in the MSS. Some of these models are given in [44] and [54].

4.2.2 Mathematical Models

Many mathematical models were discussed in the literature. Next, some of these models, [53], are derived and tested on real test data obtained from (dis)charge tests of a lithium-iron-phosphate (LFP) battery cell.

4.2.2.1 Shepherd Model

The general Shepherd equation is given by:

$$y_k = E_o + Ri_k - \frac{\mu}{\mathrm{SOC_k}} \tag{4.1}$$

where E_o is a dc voltage gain, R is the cell internal resistance, and μ is a constant factor for curve fitting.

*Relaxation effect: The transient response the battery shows after being charged or discharged before it completely settles to the final OCV.

For this model and for the next models, the SOC was calculated using ampere-hour counting (coulomb counting) as given in Equation (4.2):

$$\mathrm{SOC}(t) = \mathrm{SOC}(0) + \eta \int_0^t \frac{i(\tau)}{C_n} d\tau \tag{4.2}$$

where SOC(0) is the initial SOC which is "0" for charging and "1" for discharging, $i(\tau)$ is the current of the battery (positive for charging and negative for discharging), η is the (dis)charge efficiency, C_n is the total nominal capacity at room temperature, which is defined as the number of ampere-hours obtained from a fully charged cell at $C/30$ rate.

The output equation of Shepherd model can be written in a matrix form for an N equation as follows:

$$Y = \begin{bmatrix} y_1 \\ y_2 \\ \vdots \\ y_N \end{bmatrix} = \underbrace{\begin{bmatrix} 1 & i_1 & \mathrm{SOC}_1^{-1} \\ 1 & i_2 & \mathrm{SOC}_2^{-1} \\ \vdots & \vdots & \vdots \\ 1 & i_N & \mathrm{SOC}_N^{-1} \end{bmatrix}}_{H} \underbrace{\begin{bmatrix} E_o \\ R \\ \mu \end{bmatrix}}_{x} \tag{4.3}$$

Using least square estimation, the unknown vector x is found as follows:

$$x = \left(H^T H\right)^{-1} H^T Y$$

Again, assuming $i_k > 0$ for charging and $i_k < 0$ for discharging, then, from pulse charge and discharge tests data (pulsed 1-Amp), the vectors x_c and x_d for charge and discharge cases, respectively, are given by:

$$x_c = \begin{bmatrix} 3.3846 \\ 0.0095 \\ 0.0047 \end{bmatrix} \quad \text{and} \quad x_d = \begin{bmatrix} 3.2789 \\ 0.0881 \\ 0.0005 \end{bmatrix}$$

The results of the Shepherd model are shown in Figure 4.1.

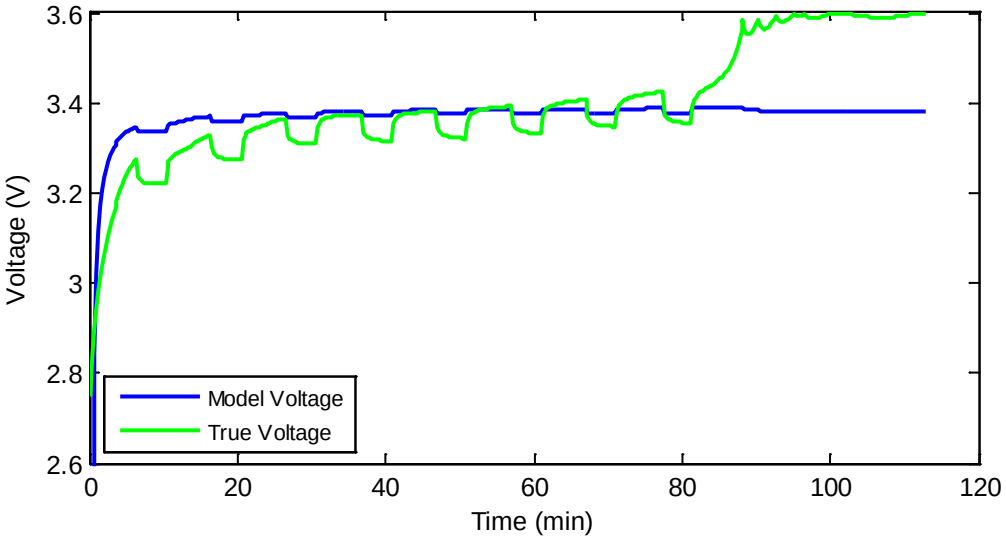

(a) Charge profile

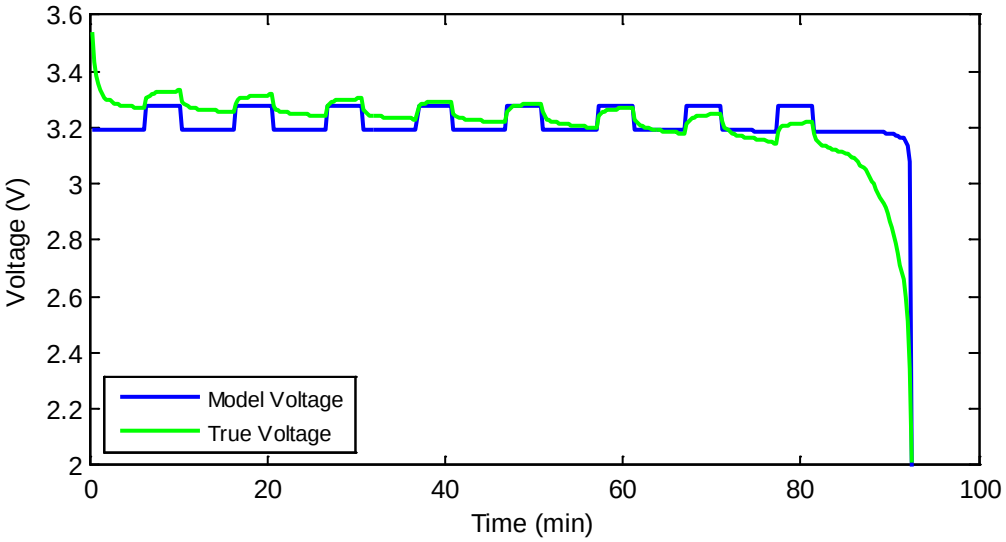

(b) Discharge profile

Figure 4.1: Shepherd model (a) charge and (b) discharge profiles.

4.2.2.2 Unnewehr Universal Model

The Unnewehr universal model is given by:

$$y_k = E_o + Ri_k - (\mu)(\mathrm{SOC_k}) \tag{4.4}$$

where E_o is a dc voltage gain, R is the internal resistance, and μ is a constant factor for curve fitting. In a matrix form for an N equation:

$$Y = \begin{bmatrix} y_1 \\ y_2 \\ \vdots \\ y_N \end{bmatrix} = \underbrace{\begin{bmatrix} 1 & i_1 & \mathrm{SOC}_1 \\ 1 & i_2 & \mathrm{SOC}_2 \\ \vdots & \vdots & \vdots \\ 1 & i_N & \mathrm{SOC}_N \end{bmatrix}}_{H} \underbrace{\begin{bmatrix} E_o \\ R \\ \mu \end{bmatrix}}_{x} \tag{4.5}$$

By applying least square estimation, the vectors x_c and x_d for charging and discharging are found as follows ($i_k > 0$ for charging and $i_k < 0$ for discharging):

$$x_c = \begin{bmatrix} 3.1798 \\ 0.0195 \\ -0.3375 \end{bmatrix} \text{ and } x_d = \begin{bmatrix} 3.1092 \\ 0.0810 \\ -0.3092 \end{bmatrix}$$

The results of the Unnewehr model are shown in Figure 4.2.

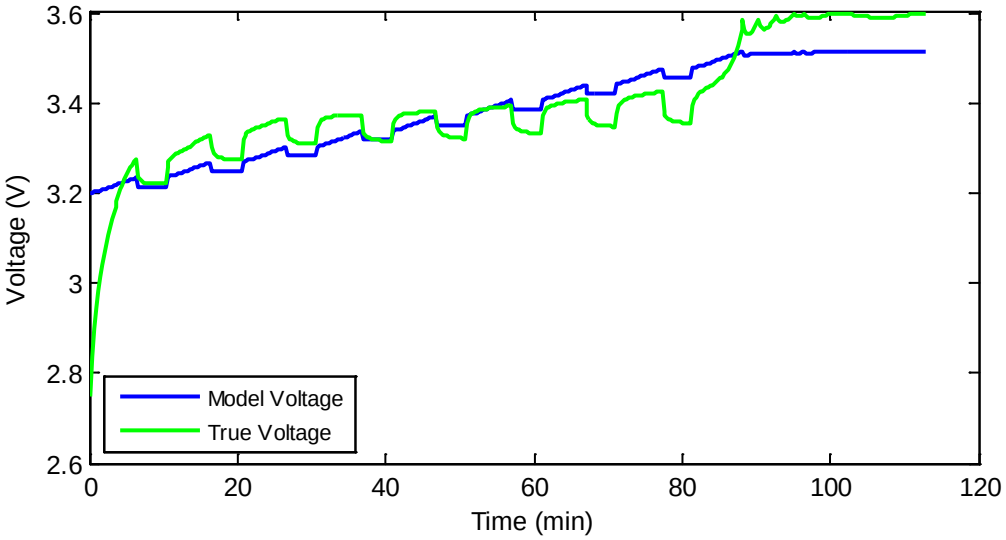

(a) Charge profile

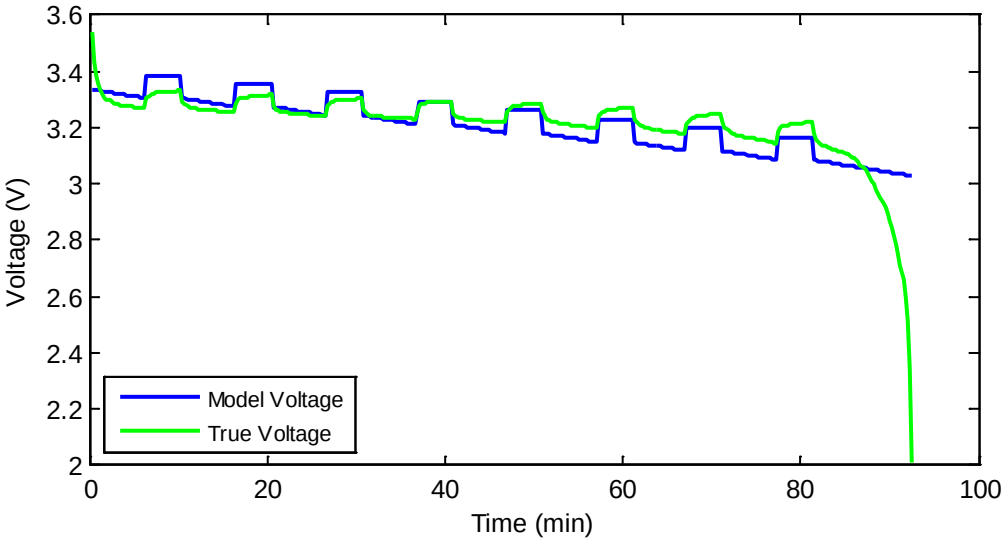

(b) Discharge profile

Figure 4.2: Unnewehr model (a) charge and (b) discharge profiles.

4.2.2.3 Nernst Model

The general Nernst equation is given by:

$$y_k = E_o + Ri_k + \mu_1 \ln\left(\mathrm{SOC_k}\right) + \mu_2 \ln\left(1 - \mathrm{SOC_k}\right) \tag{4.6}$$

where E_o is a dc voltage gain, R is the internal resistance, and μ_1 and μ_2 are constants for curve fitting. In a matrix form for an N equation:

$$Y = \begin{bmatrix} y_1 \\ y_2 \\ \vdots \\ y_N \end{bmatrix} = \underbrace{\begin{bmatrix} 1 & i_1 & \ln\left(\mathrm{SOC_1}\right) & \ln\left(1-\mathrm{SOC_1}\right) \\ 1 & i_2 & \ln\left(\mathrm{SOC_2}\right) & \ln\left(1-\mathrm{SOC_2}\right) \\ \vdots & \vdots & \vdots & \vdots \\ 1 & i_N & \ln\left(\mathrm{SOC_N}\right) & \ln\left(1-\mathrm{SOC_N}\right) \end{bmatrix}}_{H} \underbrace{\begin{bmatrix} E_o \\ R \\ \mu_1 \\ \mu_2 \end{bmatrix}}_{x} \tag{4.7}$$

Again, by applying least square estimation, the vectors x_c and x_d are ($i_\mathrm{k} > 0$ for charging and $i_\mathrm{k} < 0$ for discharging):

$$x_c = \begin{bmatrix} 3.3566 \\ 0.0343 \\ 0.0743 \\ -0.0535 \end{bmatrix} \quad \text{and} \quad x_d = \begin{bmatrix} 3.4018 \\ 0.0520 \\ 0.1446 \\ 0.0208 \end{bmatrix}$$

The results of the Nernst model are shown in Figure 4.3.

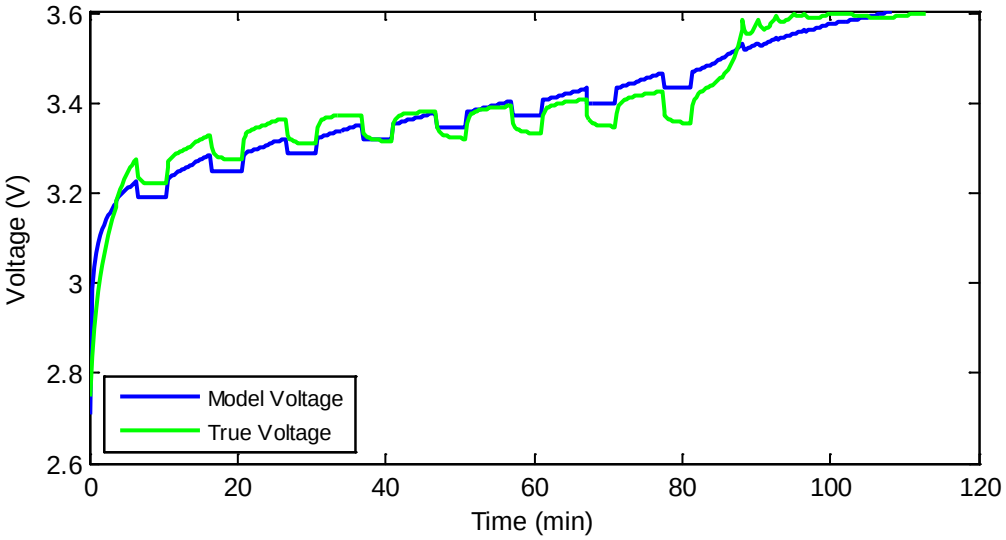

(a) Charge profile

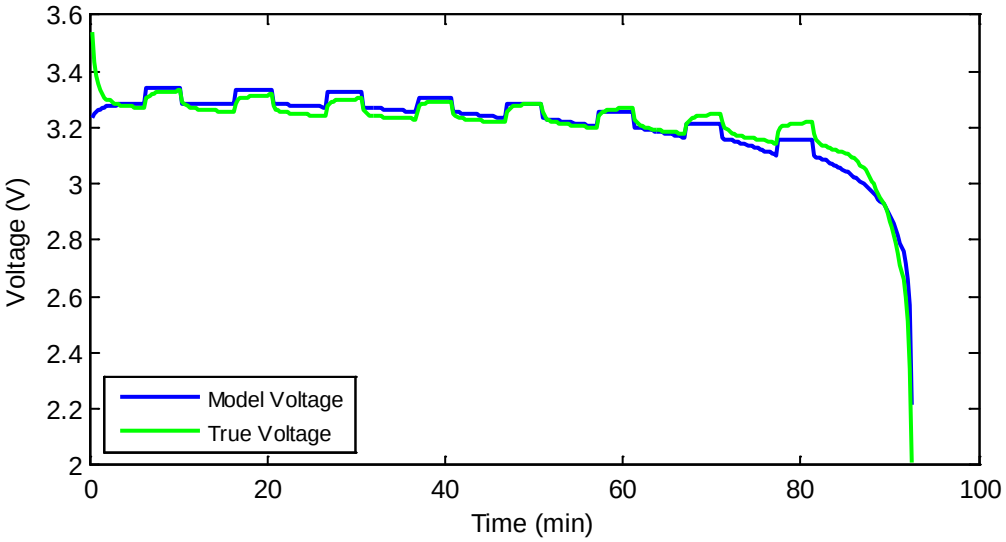

(b) Discharge profile

Figure 4.3: Nernst model (a) charge and (b) discharge profiles.

4.2.3 Equivalent Circuit Models

Another way to model the battery dynamics is through an equivalent circuit model [45]-[51]. Equivalent circuit models, which consist of a voltage source (referred as "electromotive force" or "open-circuit voltage" source) and passive circuit elements (resistors and capacitors), are used to interpret the battery behavior. Literally, these models can achieve a good accuracy and can be easily implemented in dynamic systems to predict the battery states.

To obtain values for the OCV as a function of the SOC, a fully charged cell was fully discharged and then fully charged at *C*/30 rate and the "voltage" versus "SOC" curves for both charging and discharging were averaged (see Figure 4.4). The values of the OCV versus SOC were stored in a lookup table. The reason for using *C*/30 rate is to reduce the cell's dynamics as much as possible. The values of the OCV for the charge and discharge tests were averaged to minimize the hysteresis. Next, some existent equivalent circuit models that employ an OCV source are presented.

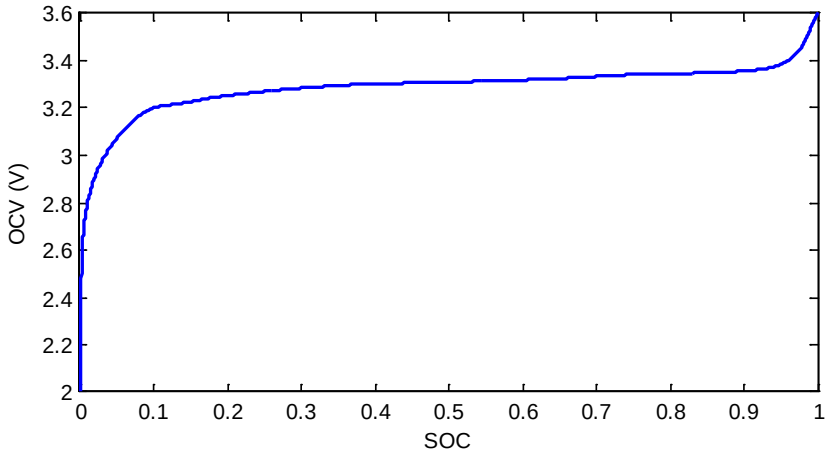

Figure 4.4: OCV as a function of SOC for charge and discharge (at room temperature).

4.2.3.1 Linear Model

The linear model incorporates an OCV voltage source in series with a (dis)charge resistance to model the voltage drop in the cell as shown in Figure 4.5.

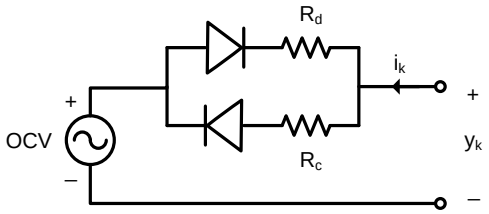

Figure 4.5: Linear cell model.

The output equation of this model is:

$$y_k = \mathrm{OCV}\left(\mathrm{SOC_k}\right) + Ri_k \tag{4.8}$$

where $R = R_c$ and $i_k > 0$ for charge, and $R = R_d$ and $i_k < 0$ for discharge. The value of R for both charge and discharge are found using least square estimation from the following N equations:

$$Y = \begin{bmatrix} y_1 - \mathrm{OCV}\left(\mathrm{SOC}_1\right) \\ y_2 - \mathrm{OCV}\left(\mathrm{SOC}_2\right) \\ \vdots \\ y_N - \mathrm{OCV}\left(\mathrm{SOC_N}\right) \end{bmatrix} = \underbrace{\begin{bmatrix} i_1 \\ i_2 \\ \vdots \\ i_N \end{bmatrix}}_{H} \underbrace{R}_{x} \tag{4.9}$$

From least square estimation, R_c (charge resistance) and R_d (discharge resistance) are found as follows:

$$R_c = 0.074\ \Omega \text{ and } R_d = 0.1016\ \Omega$$

The results of the linear model are shown in Figure 4.6.

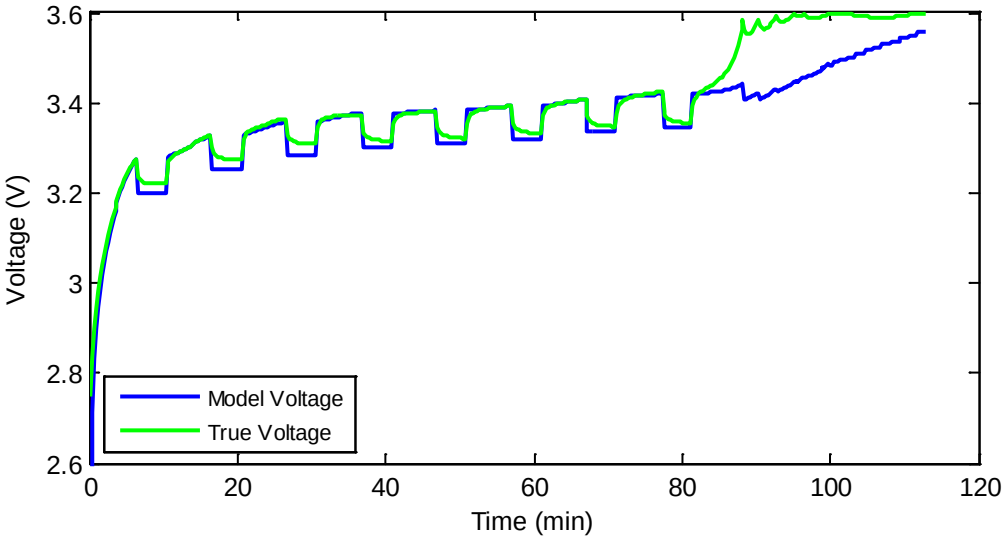

(a) Charge profile

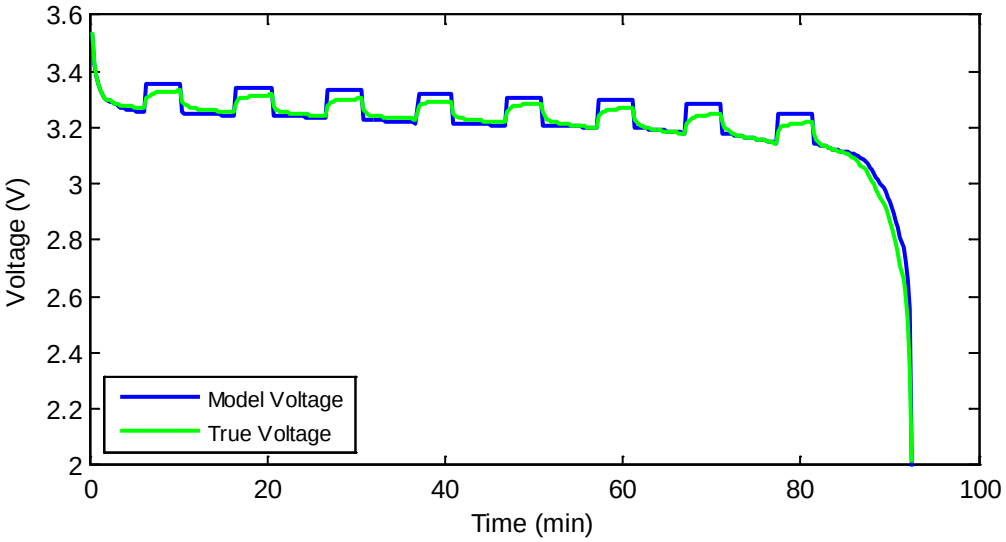

(b) Discharge profile

Figure 4.6: Linear model (a) charge and (b) discharge profiles.

4.2.3.2 RC Model

This model incorporates an additional filter (RC-network) to the linear model. The RC-network is added to implement the time constant during transients, which is equivalent in practice to the cell double layer and diffusion capacitance.

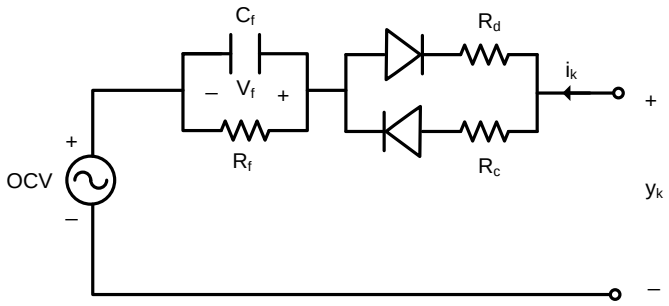

Figure 4.7: RC cell model.

The equation for this model is as follows:

$$y_k = \mathrm{OCV}\left(\mathrm{SOC_k}\right) + Ri_k + V_f \cdot \exp\left(\frac{-t}{R_f C_f}\right) \tag{4.10}$$

where $R = R_c$ and $i_k > 0$ for charge, $R = R_d$ and $i_k < 0$ for discharge, V_f is the voltage across the RC-network and t is the transient time when the cell turns from a (dis)charge to an idle state and vice versa. To find the values of the RC-network that result in a very good matching between the model and true voltages, a trial-and-error approach was used. Note that least square methods cannot be applied to find the values of R_f and C_f of the RC-network because the relationship between these elements and the output voltage is nonlinear. The model parameters are listed in Table 4.1 (the charge/discharge resistances are the same as for the linear model).

Table 4.1: RC model parameters.

V_f				*Internal Resistance*		*RC-network*	
Idle- to-charge	*Charge-to-idle*	*Idle-to-disch.*	*Disch.-to-idle*	R_c	R_d	R_f	C_f
-0.0074 V	0.074 V	0.01016V	-0.1016	0.074 Ω	0.1016 Ω	0.1 Ω	300 F

The results of the RC model are shown in Figure 4.8.

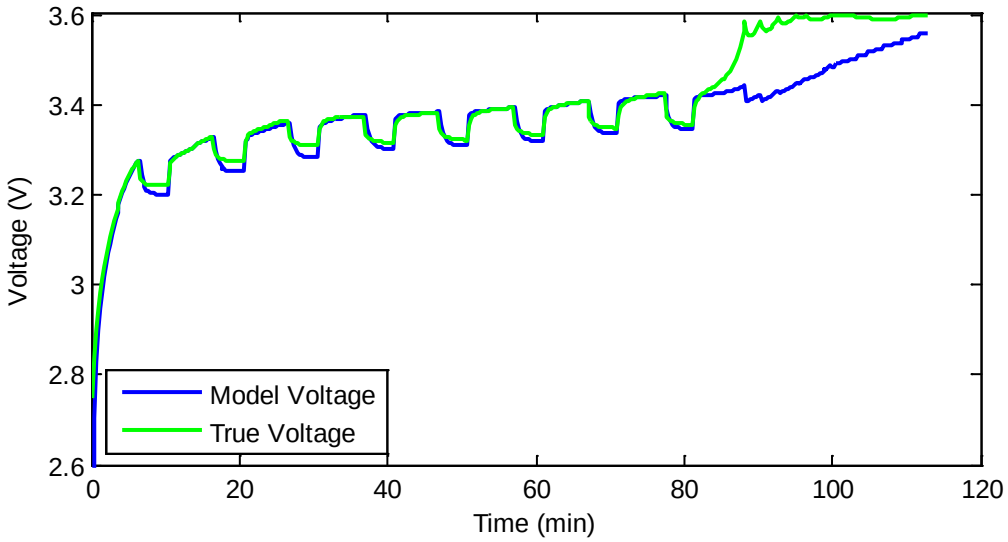

(a) Charge profile

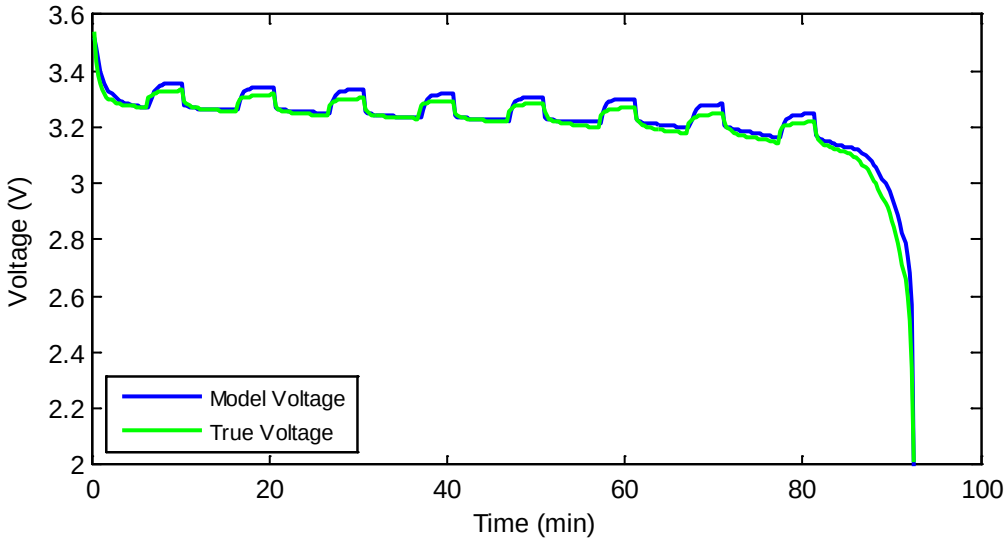

(b) Discharge profile

Figure 4.8: RC model (a) charge and (b) discharge profiles.

4.2.4 Hybrid Models

The advantage of equivalent circuit models discussed earlier is that they address the behavior of the battery through an equivalent circuit model, which is in fact easy to understand and implement and can result in a very accurate prediction. However, some behaviors cannot be modeled through equivalent circuits. Therefore, these behaviors can be modeled and added to the equivalent circuit models to improve their performance as in [47]. Some of these models are represented here. These models are presented in block diagrams for convenience.

4.2.4.1 Linear-Hysteresis Model

The hysteresis effect, which means that the cell's voltage relaxes to a value greater than the OCV for a given SOC after charging, and relaxes to a value less than the OCV of that SOC for discharging, was not modeled in the previous models. Figure 4.9 shows the linear model discussed earlier with the hysteresis added to it.

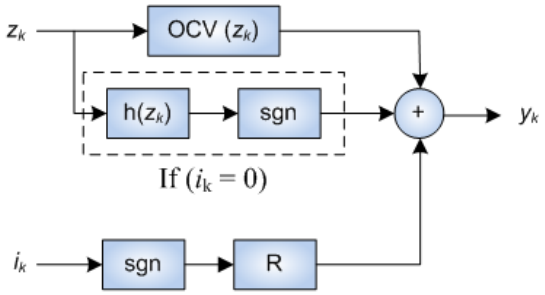

Figure 4.9: Linear-Hysteresis model.

The linear hysteresis model voltage and the hysteresis equations are given as follows:

$$y_k = \mathrm{OCV}(z_k) + sgn \cdot R\, i_k + sgn \cdot h(z_k) \tag{4.11}$$

$$h(z_k) = \frac{1}{2}\left(\mathrm{OCV}_{\mathrm{Ch}}(z_k) - \mathrm{OCV}_{\mathrm{Dis}}(z_k)\right) - sgn \cdot \left|Ri_{C/30}\right|, \text{ if } \left(i_k = 0\right), \text{ otherwise } h(z_k) = 0 \tag{4.12}$$

where *sgn* equals +1 for charge and −1 for discharge. The term $Ri_{C/30}$ represents the cell's internal voltage drop during (dis)charging at *C*/30 rate which is equal to 10 mV. The internal resistance *R* is equal to 0.074 Ω (charge) and 0.1016 Ω (discharge).

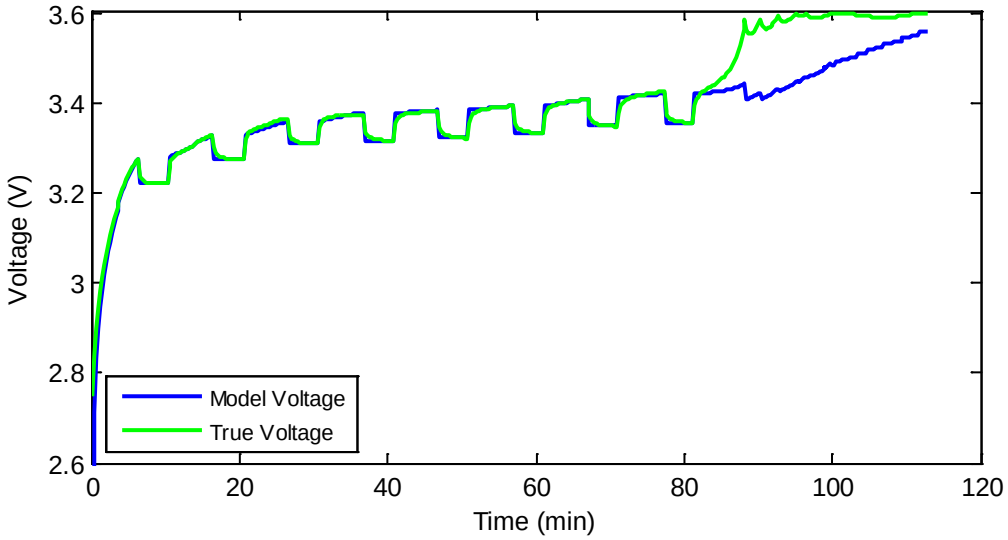

(a) Charge profile

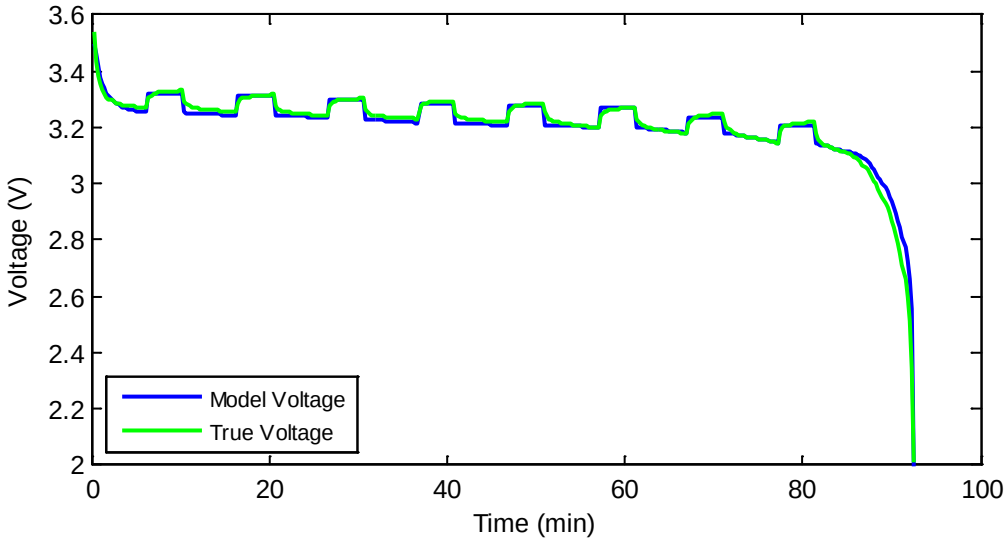

(b) Discharge profile

Figure 4.10: Linear-Hysteresis model (a) charge and (b) discharge profiles.

4.2.4.2 RC-Hysteresis Model

Similarly, the RC model discussed earlier was modified to include the hysteresis effect. The output voltage of this model is given in Equation (4.13), where *sgn* equals +1 for charge and -1 for discharge.

$$y_k = \left(\mathrm{OCV}(z_k) + sgn \cdot R i_k + sgn \cdot h(z_k)\right)\left(1 - sgn \cdot K \exp\left(\frac{-t}{\tau}\right)\right) \tag{4.13}$$

Figure 4.11 shows a block diagram of this model.

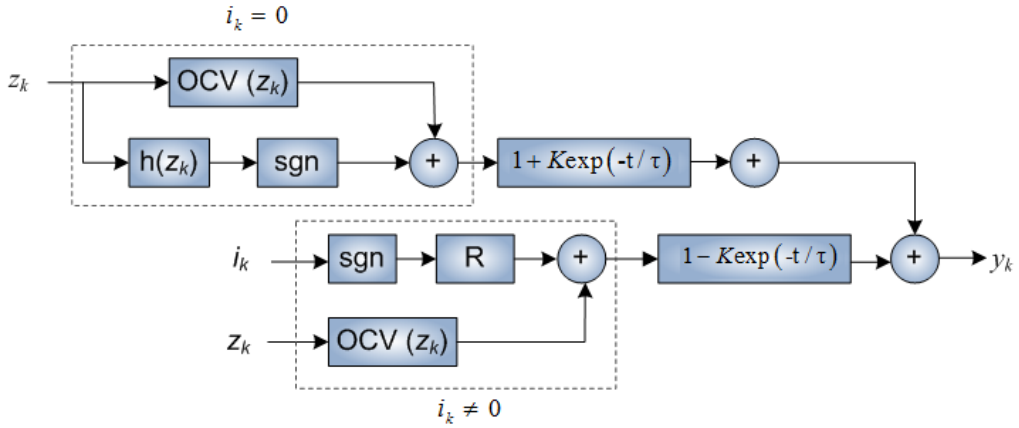

Figure 4.11: RC-Hysteresis model.

The parameters of this model are listed in Table 4.2.

Table 4.2: Parameters of the RC-Hysteresis model.

K	τ	R_c	R_d
0.01	15 sec	0.074 Ω	0.1016 Ω

The results of (dis)charging using a pulse 1-A test are shown in Figure 4.12.

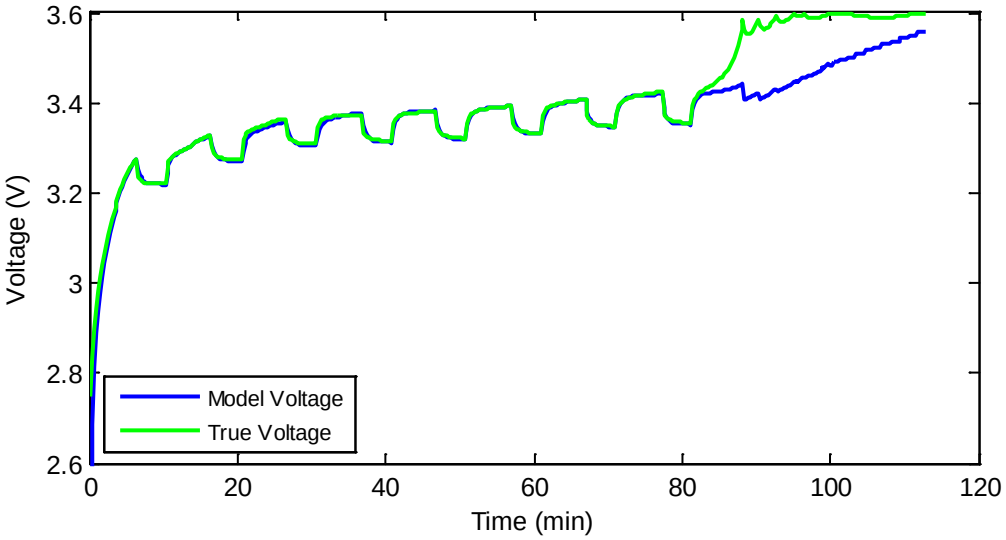

(a) Charge profile

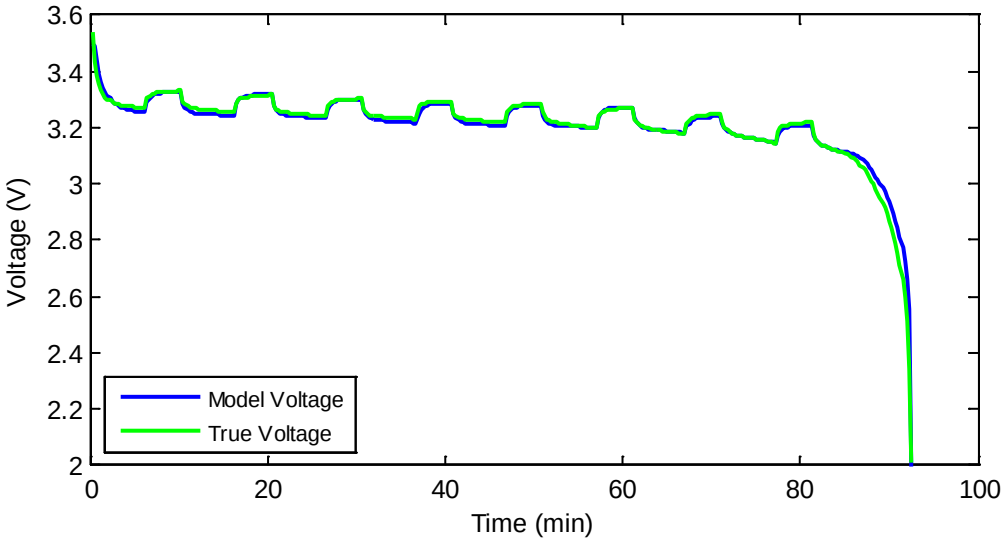

(b) Discharge profile

Figure 4.12: RC-Hysteresis model (a) charge and (b) discharge profiles.

4.3 RC-Hysteresis Model Improvement

In Section 4.2, some available models were derived and compared. It was shown that the accuracy of the model is proportional to its complexity. One limitation of these models is their poor performance when approaching the end of the charging process. The resulting error can considerably affect the SOC estimation and make it diverge (as will be shown in section 4.5). In this section, an improved version of the RC-Hysteresis model is proposed. This improved model includes the modeling of the internal resistance as a function of current and SOC as well as the addition of a correction factor to model the relaxation effect, both of which were not considered in the previous models.

4.3.1 Internal Resistance versus Current

The internal resistance was found to be dependent on the current rate. Hence, for an accurate modeling, the internal resistance must be changed if the current changes accordingly. This was noticed during the bulk or CC charging and CV modes. The explanation of that is as follows; for bulk charging, the relationship between the voltage drop and the current is not linear; that is, if the current drops by 50%, the internal resistance will rise to a higher value which is hard to predict. Similarly during CV mode, when the current drops, the internal resistance will continuously rise until the charge is terminated, which makes sense in fact since the charge acceptance rate of the cell decreases during CV mode because the cell is almost fully charged.

Table 4.3: Internal Resistance versus current rate (at SOC=0.5).

	Current Rate										
	0.05*C*	0.1*C*	0.2*C*	0.3*C*	0.4*C*	0.5*C*	0.6*C*	0.7*C*	0.8*C*	0.9*C*	*C*
R_c (Ω)	0.6154	0.2816	0.1630	0.1264	0.1128	0.1039	0.0984	0.0930	0.0890	0.0860	0.0740
R_d (Ω)	0.6154	0.3529	0.1991	0.1537	0.1310	0.1197	0.1136	0.1074	0.1026	0.1019	0.1016

4.3.2 Internal Resistance versus SOC

The internal resistance is almost constant for the most SOC range at a fixed current. However, at high SOCs when the voltage slope increases (assuming charging with a CC), the internal resistance starts increasing. In the models of section 4.2, the voltage drop in the cell was accounted through a fixed charge or discharge resistance. In fact, a fixed internal resistance can be used for the discharge if the SOC is considered 0% when a cutoff voltage of 2 V is reached. Therefore, a two-dimensional lookup table was formed to model the internal resistance as a function of SOC as well as current for further improvement at elevated SOCs.

4.3.3 Relaxation Effect

When the cell is relaxed after a charge or discharge event, its voltage converges to the OCV plus or minus a small value. This was addressed by adding the hysteresis to the models. However, the voltage takes a long time (in the order of one hour) to completely settle to its final value. To model this phenomenon, a correction (relaxation) factor, k_f, is added to the RC-Hysteresis model as shown in Figure 4.14.

4.3.4 Improved RC-Hysteresis Model

A correction (or relaxation) factor as well as a general internal resistance that is a function of current and SOC is used instead of a fixed value. The improved version of the RC-Hysteresis model is shown in Figure 4.13.

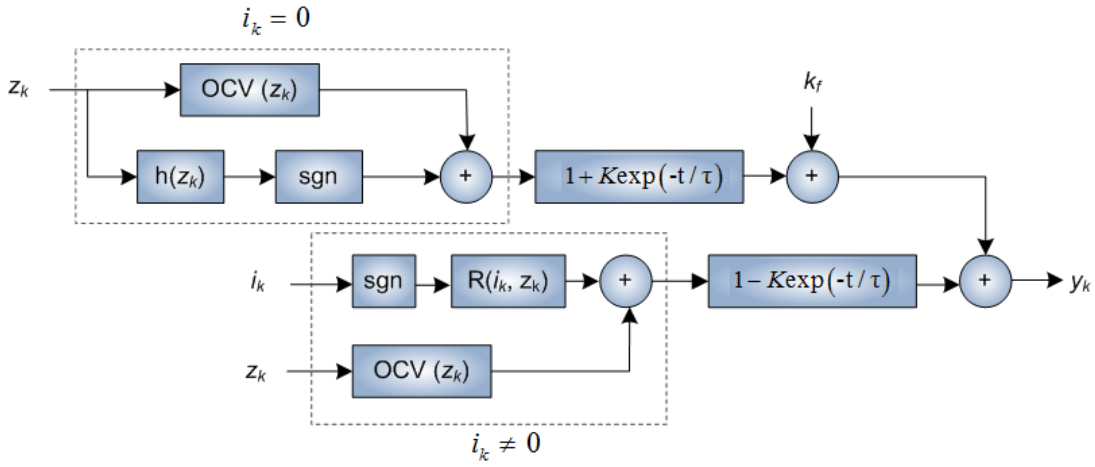

Figure 4.13: Improved RC-Hysteresis model.

The output voltage of the proposed model is given in Equation (4.14), where (+) and (-) indicate charging and discharging, respectively.

$$y_k = \left(\mathrm{OCV}(z_k) + sgn \cdot R(i_k, z_k)\, i_k(z_k) + sgn \cdot h(z_k)\right)\left(1 - sgn \cdot K\exp\left(\frac{-t}{\tau}\right)\right) + sgn \cdot k_f \qquad (4.14)$$

The parameter k_f is an additive correction linear function which is a function of relaxation time and is given in a general form as:

$$k_f\left(t_{relax}\right) = \frac{\varepsilon_V}{T_{max}} t_{relax},\ 0 < t_{relax} \le T_{max} \quad , \quad i_k = 0, \left|f_k\right| \le \varepsilon_V \qquad (4.15)$$

where $T_{\max}$ is the time at which the cell voltage settles to its steady state value during relaxation. Note that k_f is equal to zero when i_k has a value other than zero. Results of the improved RC-Hysteresis model are shown in Figure 4.14.

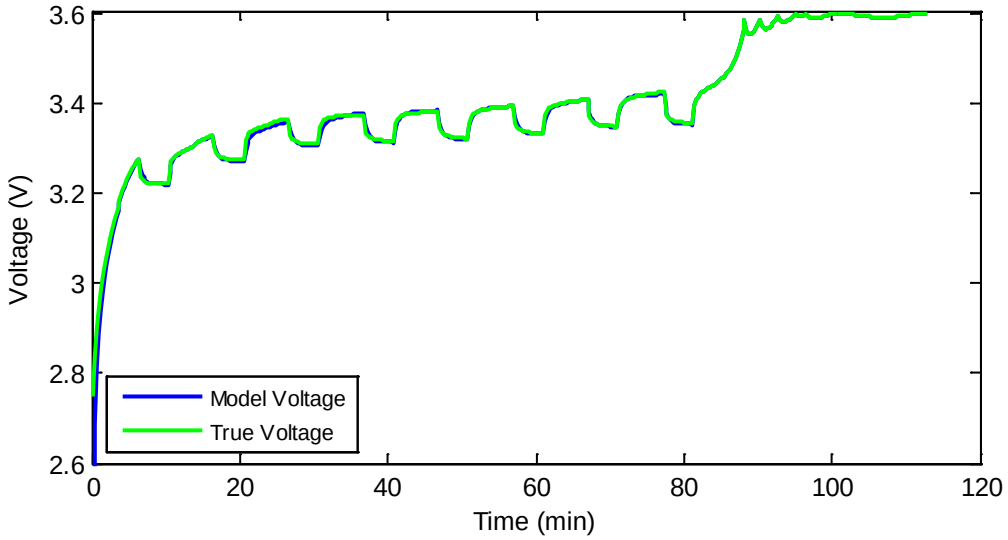

(a) Charge profile

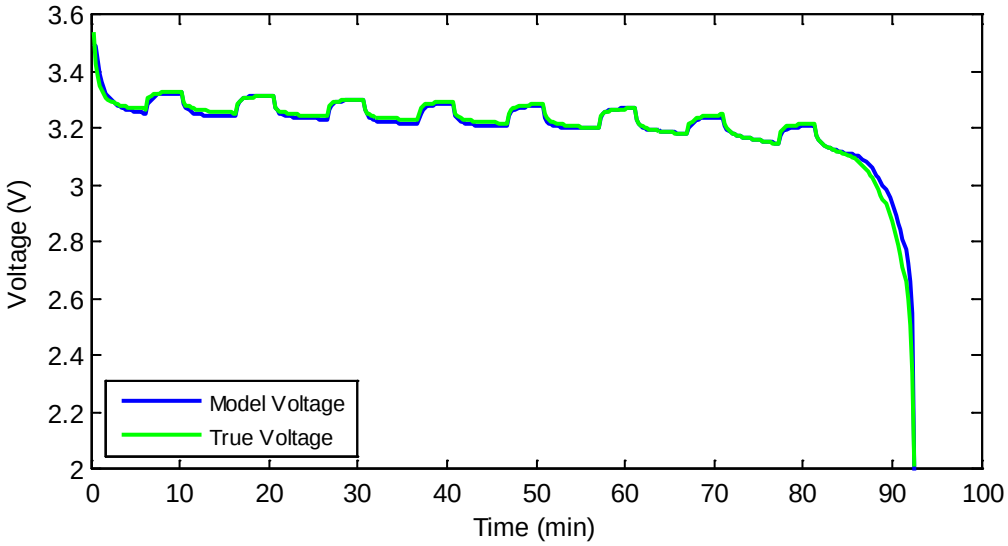

(b) Discharge profile

Figure 4.14: Improved RC-Hysteresis model (a) charge and (b) discharge profiles.

The models discussed in Sections 4.2 and 4.3 were compared in terms of the average modeling error. The results are shown in Figure 4.15.

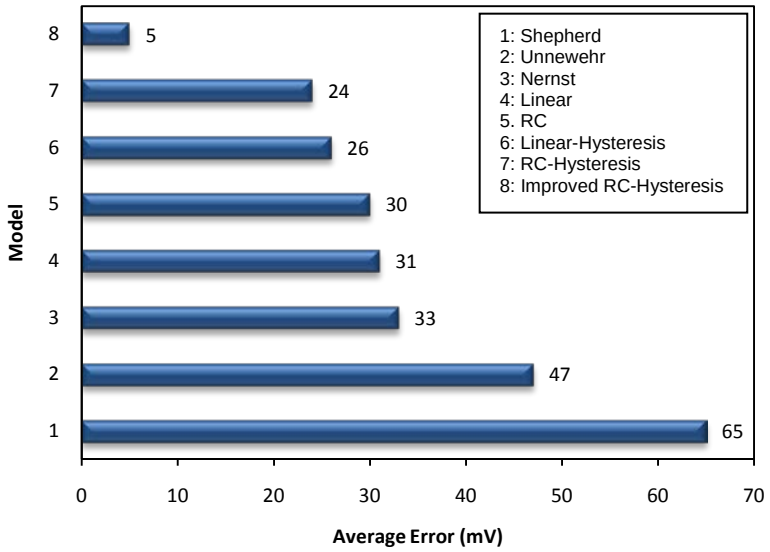

Figure 4.15: Average modeling error for the discussed models at for the 1-A pulse (dis)charge test (at room temperature).

4.4 Temperature Effect

One missing factor in the discussed models is the temperature. So far, all the models' parameters were found at room temperature. In general, battery performance is strongly dependent on the temperature. At very low temperatures, the electrolyte may freeze, while at very high temperatures, the active materials may break down. However, at moderate temperatures, the battery performance is the best. In this section, the parameters of the models are validated at different temperatures from -30^{o} C to 50^{o} C in increments of 10^{o} C.

4.4.1 OCV versus Temperature

In the previous section, the relationship between the OCV and SOC was found at room temperature. To establish a general relationship between the OCV and SOC at a wide range of temperatures, the following procedure was followed:

1. The cell is placed in the chamber and soaked at the test temperature for 4 hours.
2. The cell is charged (CC to 3.6 V then CV to 1 mA).
3. The cell is discharged at *C*/20 rate (50 mA) until the voltage drops to 2 V.
4. The cell is relaxed for few minutes.
5. The cell is charged at *C*/20 rate (50 mA) until the voltage reaches 3.6 V.

This procedure is repeated at each test temperature from -30^{o} C to 50^{o} C in increments of 10^{o} C. The way the SOC and OCV values were calculated is similar to the calculations made at room temperature. The only difference is that the nominal capacity, which was found to be strongly dependent on temperature, was found experimentally at each temperature (see Figure 4.17). The OCV versus SOC curves at these temperatures are shown in Figure 4.16.

The values of OCV can be stored in a two-dimensional lookup table as a function of temperature and SOC as follows:

$$\mathrm{OCV} = \begin{bmatrix} \mathrm{OCV}_{T_1, SOC_1} & \cdots & \mathrm{OCV}_{,T_1, SOC_N} \\ \vdots & \ddots & \vdots \\ \mathrm{OCV}_{T_M, SOC_1} & \cdots & \mathrm{OCV}_{T_M, SOC_N} \end{bmatrix}_{M \times N}$$

In a vector form, the OCV values can be expressed as follows:

$$\mathrm{OCV}^{T} = [\mathrm{OCV}(1), \ldots, \mathrm{OCV}(N)]$$

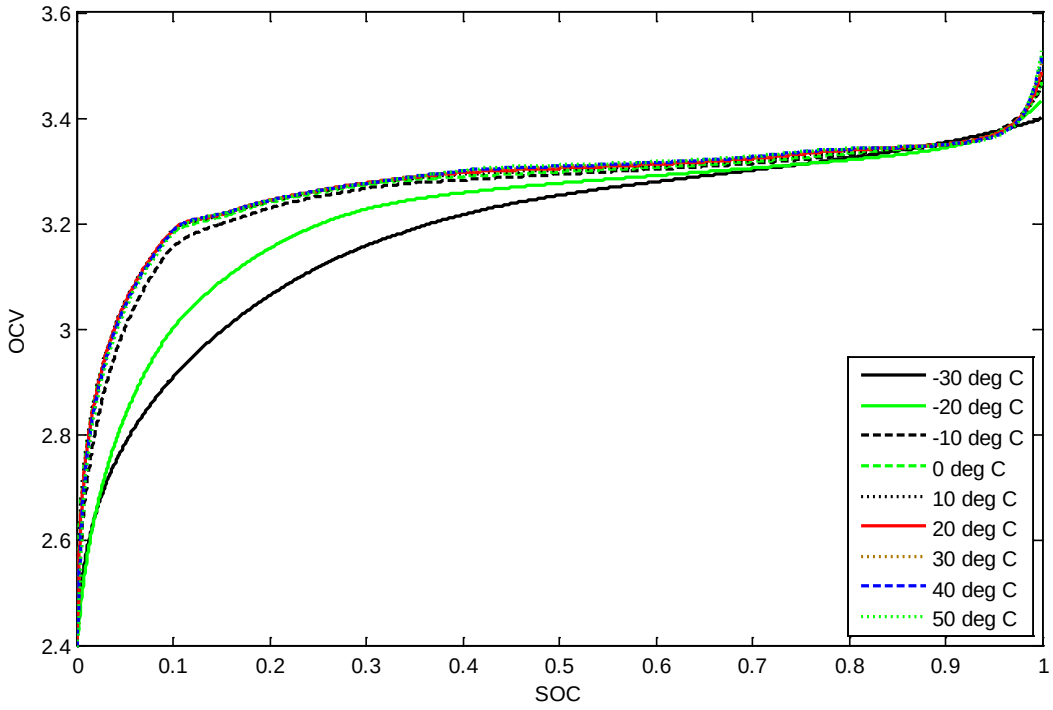

Figure 4.16: OCV versus SOC at different temperatures.

4.4.2 Capacity versus Temperature

The battery capability of holding charge was found to be descending as the temperature goes down and ascending as the temperature goes up. The reason for this is that the viscosity of the electrolyte increases at low temperatures (the electrolyte freezes at temperatures below zero), while at high temperatures, the viscosity decreases, which as a result, increases the diffusion of the ions and thus increases the capacity. The cell nominal capacity versus temperature is shown in Figure 4.17.

The values of the nominal capacity at different temperatures were used to calculate the SOC values in Figure 4.17 using ampere-hour. However, the capacity of the battery at different temperatures is an important element in calculating the expected return. The capacity values as a

function of temperature can be used in the dynamic economic model (section 2.7) to calculate the expected return.

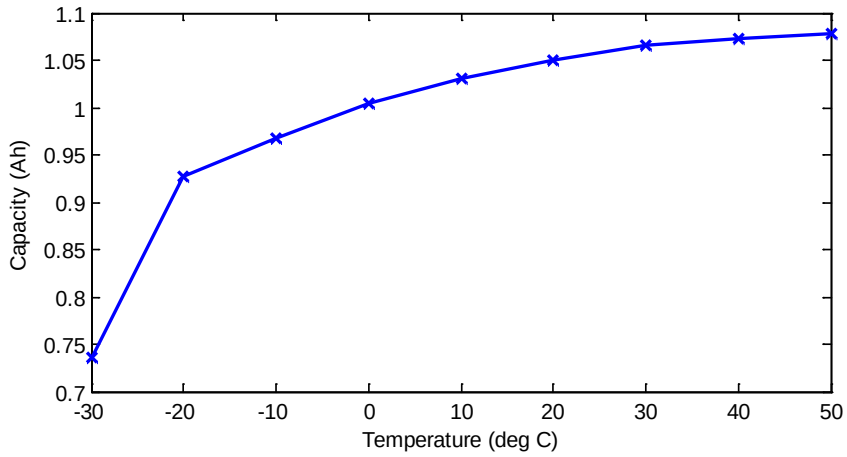

Figure 4.17: Nominal capacity at different temperatures.

4.4.3 Internal Resistance versus Temperature

From the OCV tests, the internal resistance at *C*/20 rate was calculated at each temperature from -30^{o} C to 50^{o} C in increments of 10^{o} C. To model the internal resistance as a function of temperature and current, the following test procedure is followed:

1. The cell is placed in the chamber and soaked at the test temperature for 4 hours.
2. The cell is completely discharged.
3. The cell is charged (CC to 3.6 V and CV to 50 mA) and discharged (CC to 2 V) at C/4, C/2 and C rates.
4. This procedure is repeated at the following temperatures (50^{o} C, 25^{o} C, 10^{o} C, 0^{o} C, -10^{o} C, -20^{o} C and -30^{o} C).

The results show that the resistance starts increasing dramatically as the temperature goes down, as shown in Figure 4.18.

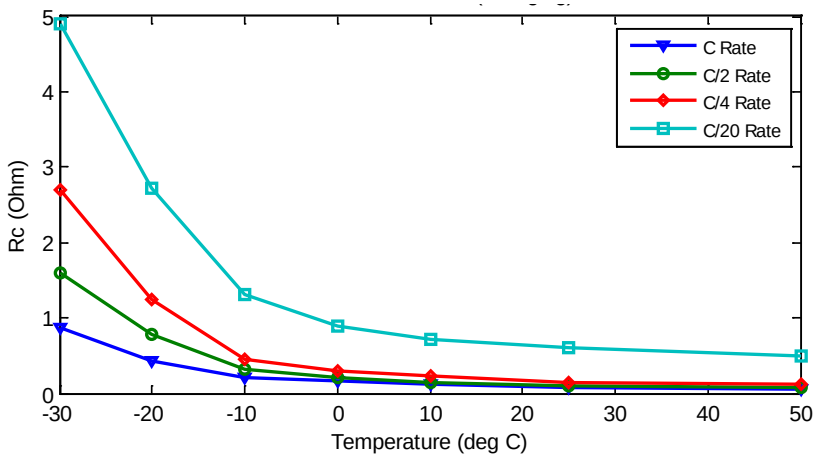

(a) Internal Resistance (charge)

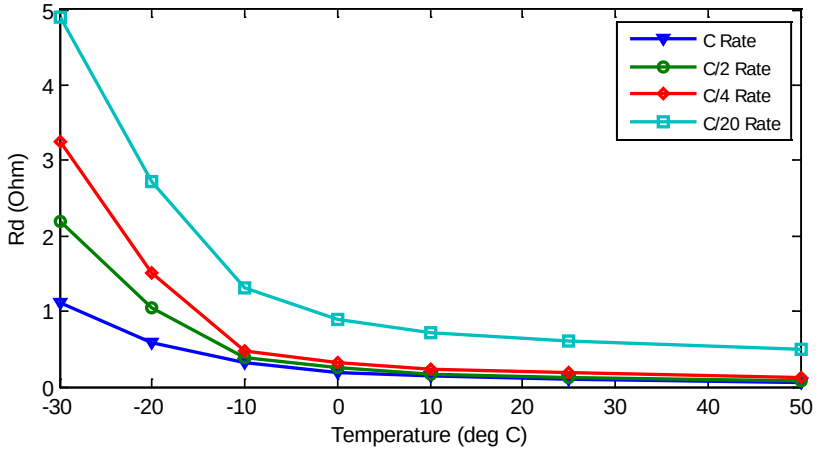

(b) Internal Resistance (discharge)

Figure 4.18: Internal resistance versus temperature at SOC=0.5 (a) charging, (b) discharging.

To include the dependence on the current rate, temperature and SOC, the values of the internal resistance can be stored in a lookup table and used every time-step based on the measurement of the current, temperature and SOC. In general, the internal resistance can be written as:

$$R_{i_1} = \begin{bmatrix} R_{i_1,T_1,SOC_1} & \cdots & R_{i_1,T_1,SOC_N} \\ \vdots & \ddots & \vdots \\ R_{i_1,T_M,SOC_1} & \cdots & R_{i_1,T_M,SOC_N} \end{bmatrix}_{M\times N} , \quad \ldots , \quad R_{i_L} = \begin{bmatrix} R_{i_L,T_1,SOC_1} & \cdots & R_{i_L,T_1,SOC_N} \\ \vdots & \ddots & \vdots \\ R_{i_L,T_M,SOC_1} & \cdots & R_{i_L,T_M,SOC_N} \end{bmatrix}_{M\times N}$$

In a vector form, the internal resistance is expressed as:

$$R^T = [R_{i_1}(1),...,R_{i_1}(N),\ R_{i_2}(1),...,R_{i_2}(N),\ R_{i_L}(1),...,R_{i_L}(N)]$$

4.5 Applications

Two applications of the proposed model are presented in this section; SOC and SOH estimation. The technique used to estimate these two quantities is based on EKFs. These filters rely on the concept of real-time observers. They can be used to optimally estimate the inner states of a dynamic system.

In fact, estimating the SOC and SOH using EKFs is advantageous compared to conventional methods. For example; the "discharge test" cannot be used in real-time; "ampere-hour counting" leads to drifting away after time and gives inaccurate results due to added errors; "open-circuit voltage" requires very low rates for a good accuracy; and "internal resistance and impedance measurements" require an AC current injection into the cell which cannot be achieved in real-time [58]. The proposed techniques have two main advantages; (1) it guarantees convergence under any load and (2) it can be implemented in real-time. Next, an EKF algorithm is constructed in a step-by-step procedure [59].

Firstly, the model is expressed in state space representation:

$$x_k = f_{k-1}(x_{k-1},u_{k-1},\omega_{k-1}) \tag{4.16}$$

$$y_k = h_k(x_k,u_k,v_k) \tag{4.17}$$

$$\omega_k \sim (0, Q_k),\ v_k \sim (0, R_k)$$

where x is the model state, k is the time index, $h_k(.)$ is the output equation of the model, ω_k is a discrete-time white noise (process uncertainty) with a covariance matrix Q_k, and v_k is a discrete-time white noise (measurement uncertainty) with covariance matrix R_k.

Secondly, the filter is initialized:

$$\hat{x}_0^+ = E[x_0] \tag{4.18}$$

$$P_0^+ = E[(x_0 - \hat{x}_0^+)(x_0 - \hat{x}_0^+)^T] \tag{4.19}$$

where P is the estimation error covariance matrix.

Thirdly, for k = 1, 2, …, the following steps are performed:

a) *Compute the following partial derivative matrices:*

$$F_{k-1} = \left.\frac{\partial f_{k-1}}{\partial x}\right|_{\hat{x}_{k-1}^+} \tag{4.20}$$

$$L_{k-1} = \left.\frac{\partial f_{k-1}}{\partial \omega}\right|_{\hat{x}_{k-1}^+} \tag{4.21}$$

b) *Perform the time update of the state estimate and estimation error covariance:*

$$P_k^- = F_{k-1}P_{k-1}^+F_{k-1}^T + L_{k-1}Q_{k-1}L_{k-1}^T \tag{4.22}$$

$$\hat{x}_k^- = f_{k-1}(\hat{x}_{k-1}^+, u_{k-1}, 0) \tag{4.23}$$

c) *Compute the following partial derivatives:*

$$H_k = \left.\frac{\partial h_k}{\partial x}\right|_{\hat{x}_k^-} \tag{4.24}$$

$$M_k = \left.\frac{\partial h_k}{\partial v}\right|_{\hat{x}_k^-} \tag{4.25}$$

d) Measurement update:

$$K_k = P_k^- H_k^T (H_k P_k^- H_k^T + M_k R_k M_k^T)^{-1} \tag{4.26}$$

$$\hat{x}_k^+ = \hat{x}_k^- + K_k (y_k - h_k(\hat{x}_k^-, 0)) \tag{4.27}$$

$$P_k^+ = (I - K_k H_k) P_k^- \tag{4.28}$$

Figure 4.19 shows the operation of the Kalman filter in predicting the models' states. The rest of this section will give a derivation of the EKF algorithms for the SOC and SOH estimation.

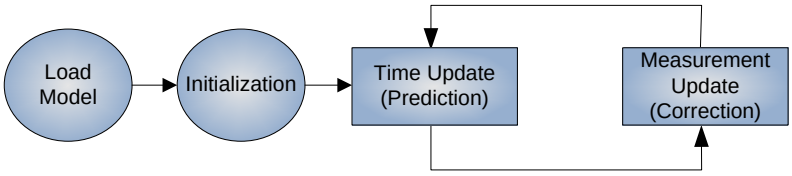

Figure 4.19: Kalman filter operation.

4.5.1 SOC Estimation Using EKF

In order to set a mathematical procedure for SOC estimation, the dynamics of the system must be expressed mathematically. If the current is assumed to be positive during charging, and negative during discharging, then, the equation of the state of charge, *z*, is given by:

$$z(t) = z(0) + \eta \int_0^t \frac{i(\tau)}{C_n} d\tau \tag{4.29}$$

where z(0) is the initial SOC, η is the charging or discharging efficiency, and C_n is the nominal capacity.

In recursive discrete-time representation, the last equation is expressed as:

$$z_k = z_{k-1} + \left(\frac{\eta \Delta t}{C_n} \right) i_{k-1} \tag{4.30}$$

where Δt is the time step between instants *k* and *k-1*. The output equation can be any of the previous models' equations. The SOC can be estimated through discrete-time EKF procedure [Equations (4.16) through (4.28)] as follows:

- Firstly, the model is expressed in state space representation:

$$z_k = f_{k-1}(z_{k-1}, i_{k-1}, \omega_{k-1})$$

$$= z_{k-1} + \left(\frac{\eta \Delta t}{C_n}\right) i_{k-1} + \omega_{k-1}$$

$$y_k = h_k(z_k, i_k, v_k)$$

$$= h_k(z_k, i_k) + v_k$$

$$\omega_k \sim (0, Q_k), \; v_k \sim (0, R_k)$$

where *z* is the SOC, *k* is the time index, $h_k(.)$ is the output equation of the model, ω_k is a discrete-time white noise (process uncertainty) with a covariance matrix Q_k, and v_k is a discrete-time white noise (measurement uncertainty) with covariance matrix R_k.

- Secondly, the filter is initialized:

$$\hat{z}_0^+ = E[z_0]$$

$$= z_0$$

$$P_0^+ = E[(z_0 - \hat{z}_0^+)(z_0 - \hat{z}_0^+)^T]$$

$$= P_{z_0}$$

where *P* is the estimation error covariance matrix.

- Thirdly, for k = 1, 2, …, the following steps are performed:

1. Compute the following partial derivative matrices:

$$F_{k-1} = \left.\frac{\partial f_{k-1}}{\partial z}\right|_{\hat{z}_{k-1}^{+}}$$

$$= 1$$

$$L_{k-1} = \left.\frac{\partial f_{k-1}}{\partial \omega}\right|_{\hat{z}_{k-1}^{+}}$$

$$= 1$$

2. Perform the time update of the state estimate and estimation error covariance:

$$P_k^{-} = F_{k-1} P_{k-1}^{+} F_{k-1}^{T} + L_{k-1} Q_{k-1} L_{k-1}^{T}$$

$$= P_{k-1}^{+} + Q_{k-1}$$

$$\hat{z}_k^{-} = f_{k-1}(\hat{z}_{k-1}^{+}, u_{k-1}, 0)$$

3. Compute the following partial derivatives:

$$H_k = \left.\frac{\partial h_k}{\partial z}\right|_{\hat{z}_k^{-}}$$

$$= \frac{y_k(\hat{z}_k^{-}) - y_{k-1}(\hat{z}_k^{-})}{\hat{z}_k^{-} - \hat{z}_{k-1}^{-}}$$

$$M_k = \left.\frac{\partial h_k}{\partial v}\right|_{\hat{z}_k^{-}}$$

$$= 1$$

4. Measurement update:

$$K_k = P_k^- H_k^T (H_k P_k^- H_k^T + M_k R_k M_k^T)^{-1}$$

$$= (P_{k-1}^+ + Q_{k-1}).\left(\frac{y_k(\hat{z}_k^-) - y_{k-1}(\hat{z}_k^-)}{\hat{z}_k^- - \hat{z}_{k-1}^-}\right)\left((P_{k-1}^+ + Q_{k-1}).\left(\frac{y_k(\hat{z}_k^-) - y_{k-1}(\hat{z}_k^-)}{\hat{z}_k^- - \hat{z}_{k-1}^-}\right)^2 + R_k\right)$$

$$= (P_{k-1}^+ + Q_{k-1})^2.\left(\frac{y_k(\hat{z}_k^-) - y_{k-1}(\hat{z}_k^-)}{\hat{z}_k^- - \hat{z}_{k-1}^-}\right)^3 + R_k.(P_{k-1}^+ + Q_{k-1}).\left(\frac{y_k(\hat{z}_k^-) - y_{k-1}(\hat{z}_k^-)}{\hat{z}_k^- - \hat{z}_{k-1}^-}\right)$$

$$\hat{z}_k^+ = \hat{z}_k^- + K_k(y_k - h_k(\hat{z}_k^-, 0))$$

$$P_k^+ = (I - K_k H_k) P_k^-$$

The results of the SOC estimation are shown in Figure 4.20 [(a) – (h)] for those models for the 1-A pulse charging test. The errors added to the voltage and current measurments were 10 mV and 10 mA, while the initial SOC was purposefully set at 0.2 instead of zero to see how the models converge to the true value.

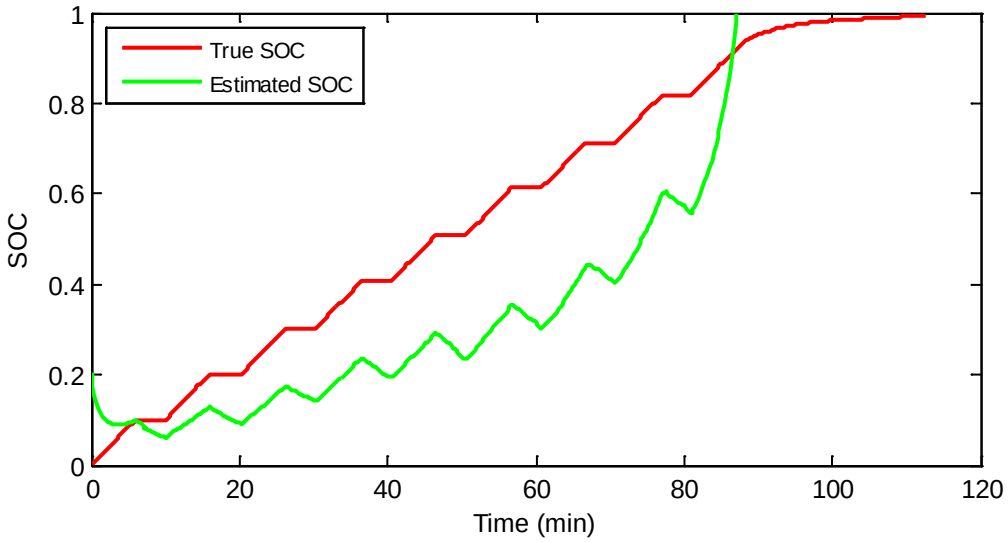

(a) Shepherd model (charge)

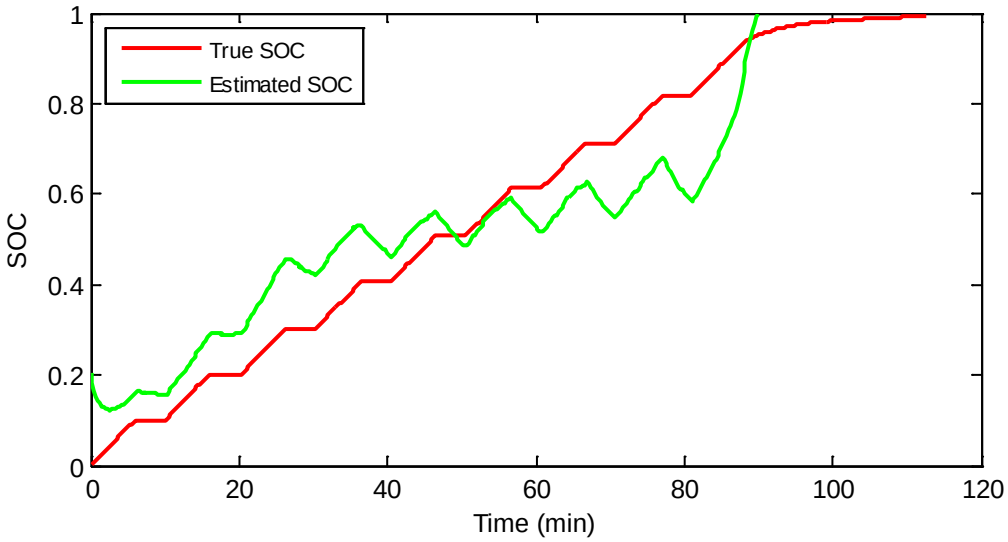

(b) Unnewehr model (charge)

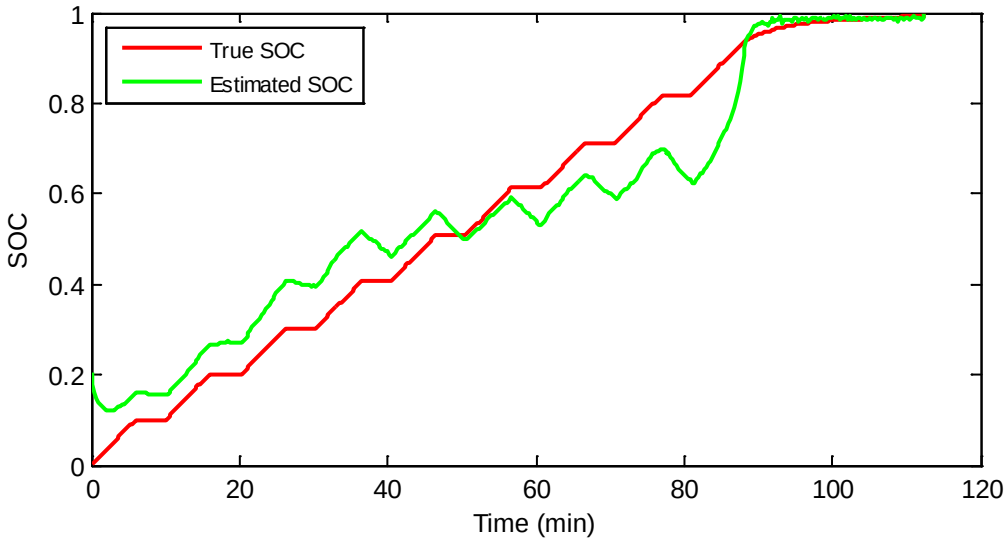

(c) Nernst model (charge)

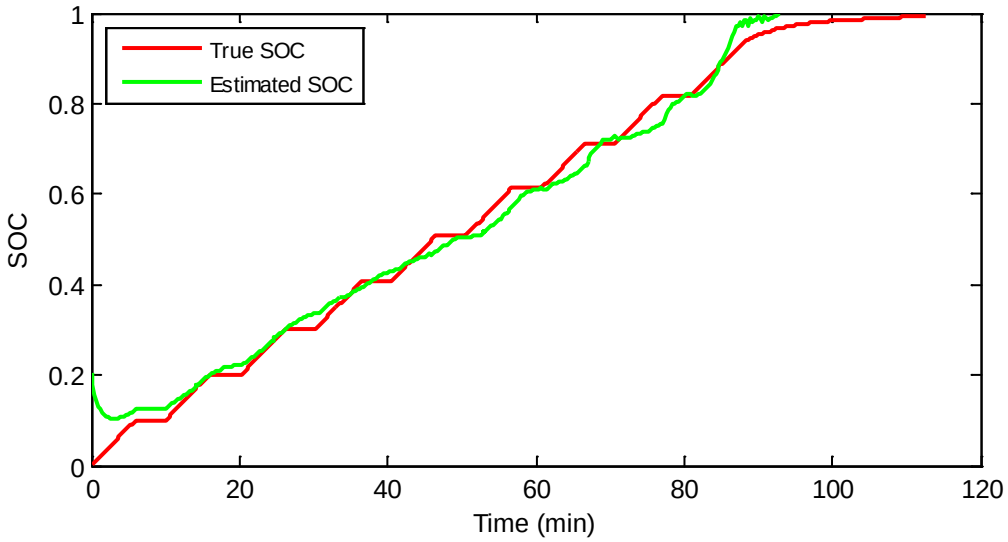

(d) Linear model (charge)

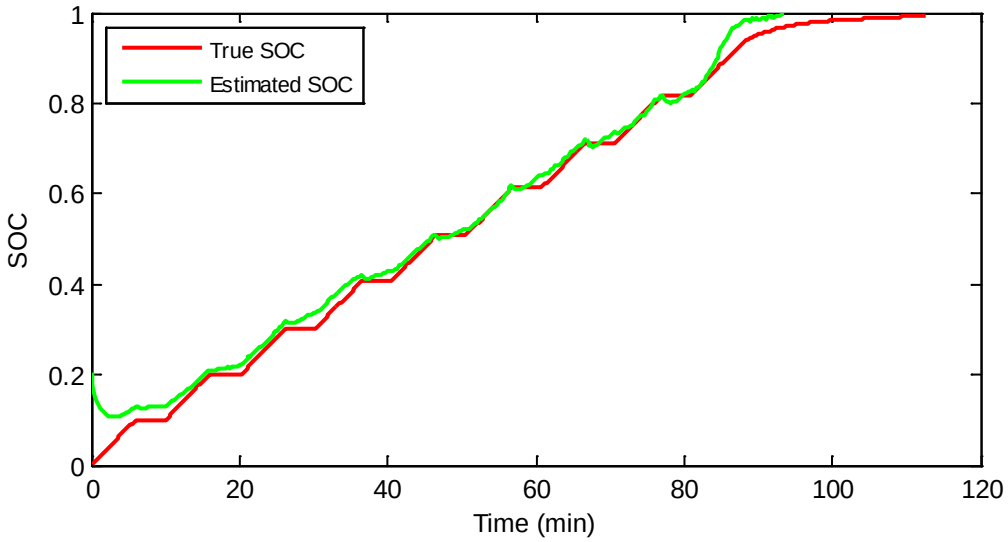

(e) RC model (charge)

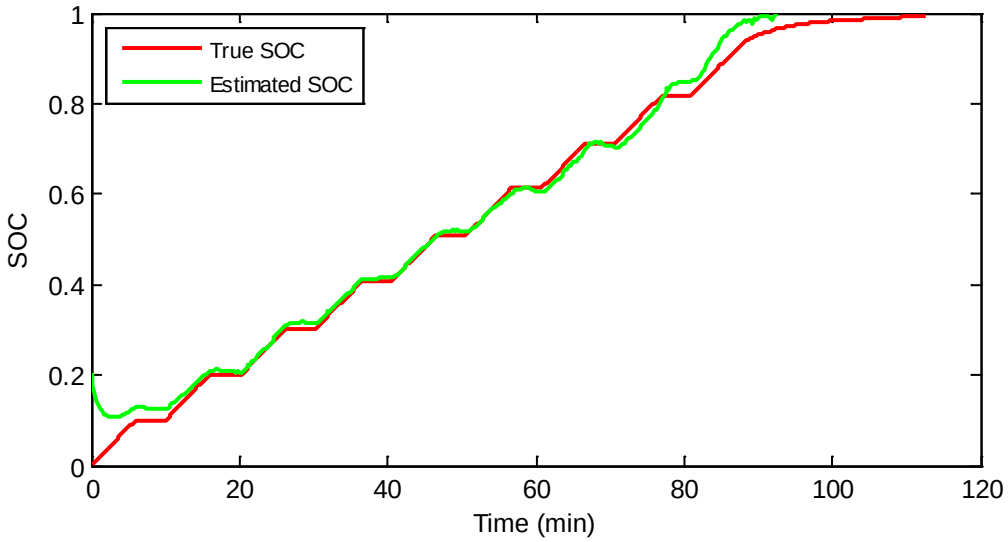

(f) Linear-hysteresis model (charge)

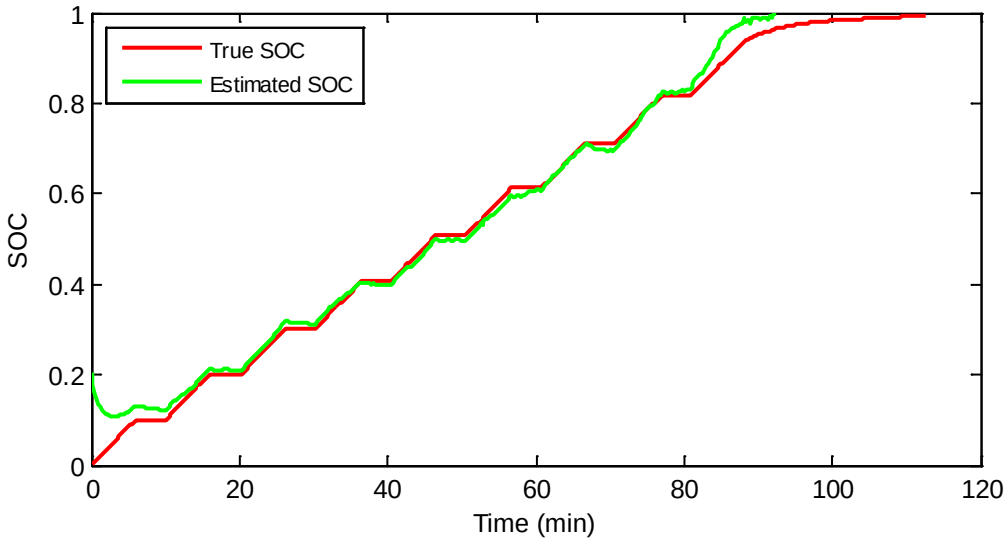

(g) RC-hysteresis model (charge)

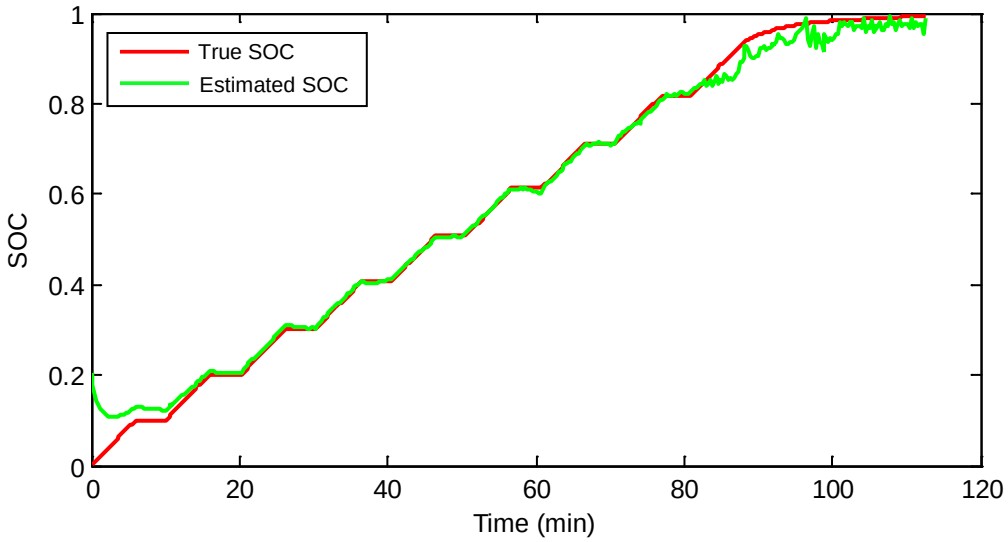

(h) Improved RC-hysteresis model (charge)

Figure 4.20: SOC estimation results obtained for the1-A pulse charging test for the discussed models at room temperature.

Similarly, the results of the SOC estimation for the 1-A pulse discharge test are shown in Figure 4.21 [(a) – (h)] . The errors added to the voltage and current measurments were 10 mV

and 10 mA, while the initial SOC was purposefully set at 0.8 instead unity to see how the models converge to the true value.

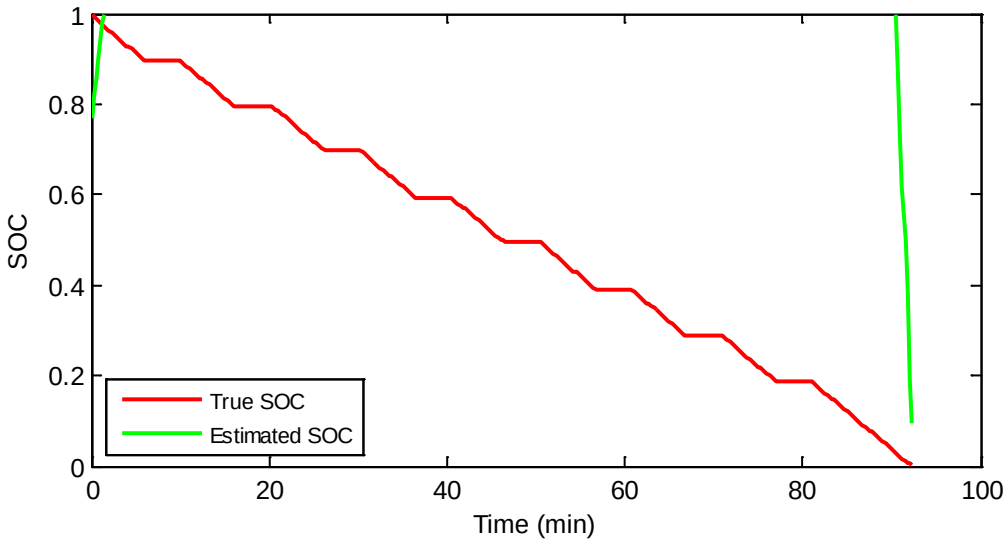

(a) Shepherd model (discharge)

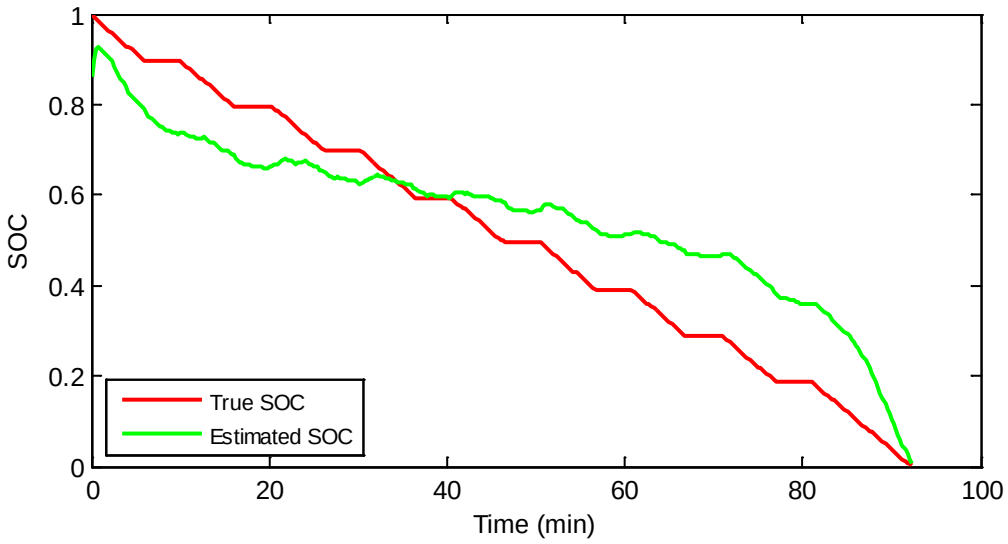

(b) Unnewehr model (discharge)

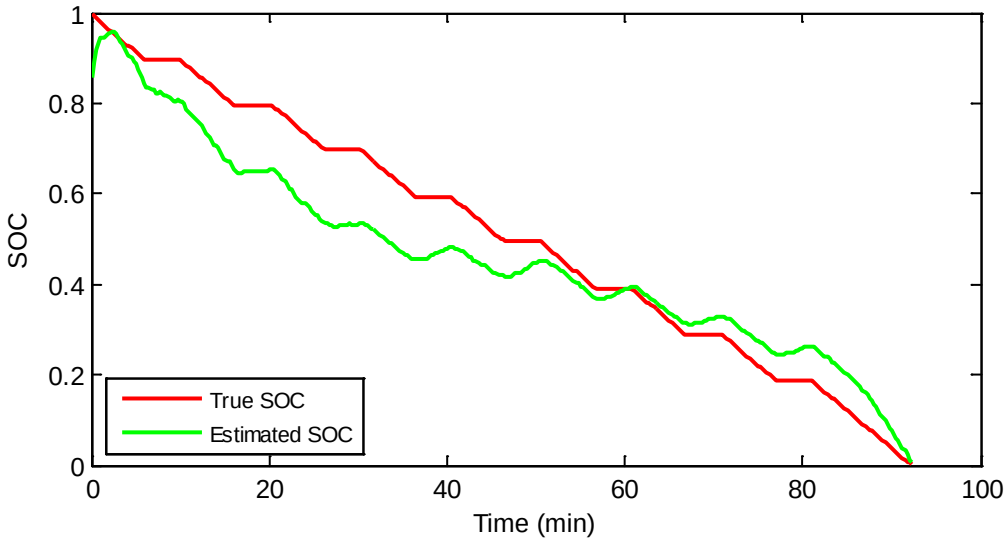

(c) Nernst model (discharge)

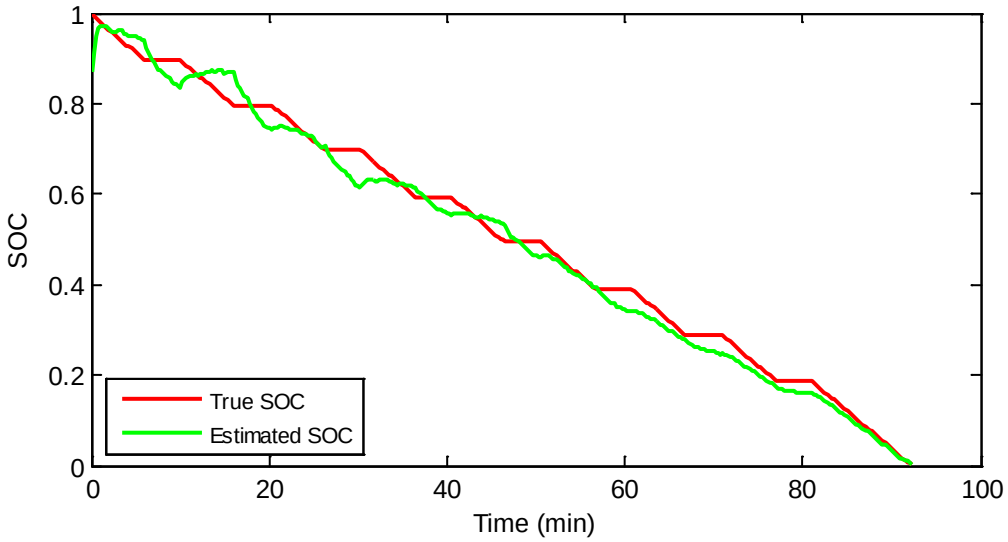

(d) Linear model (discharge)

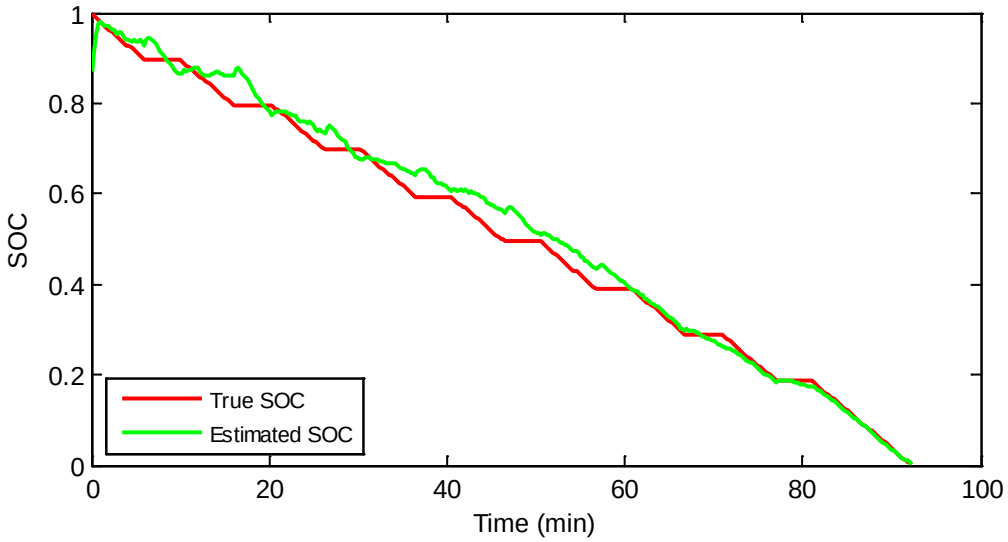

(e) RC model (discharge)

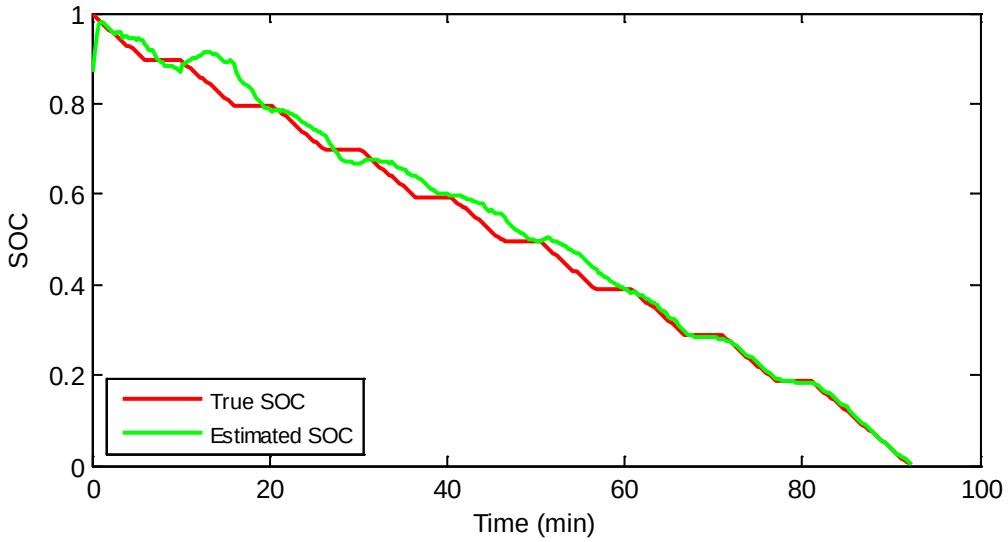

(f) Linear-hysteresis model (discharge)

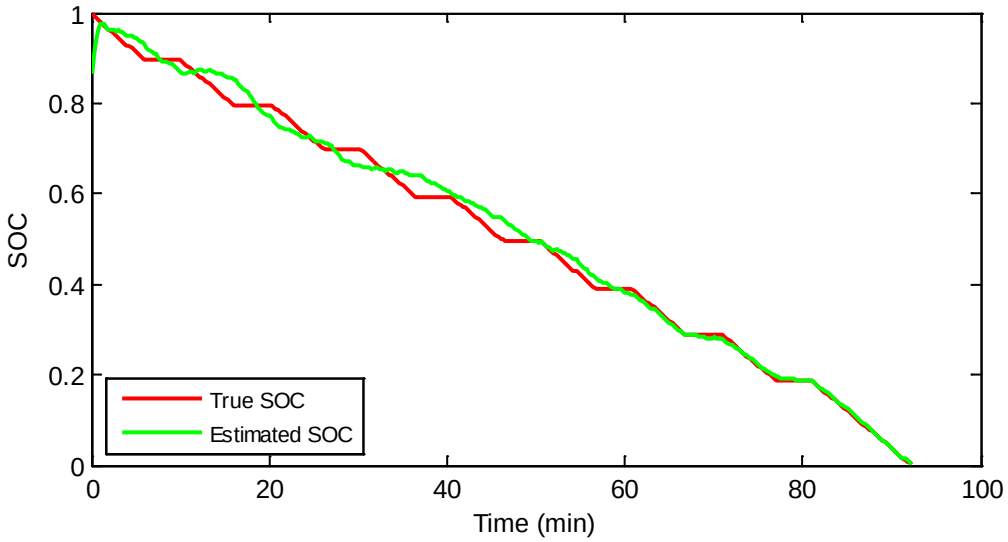

(g) RC-hysteresis model (discharge)

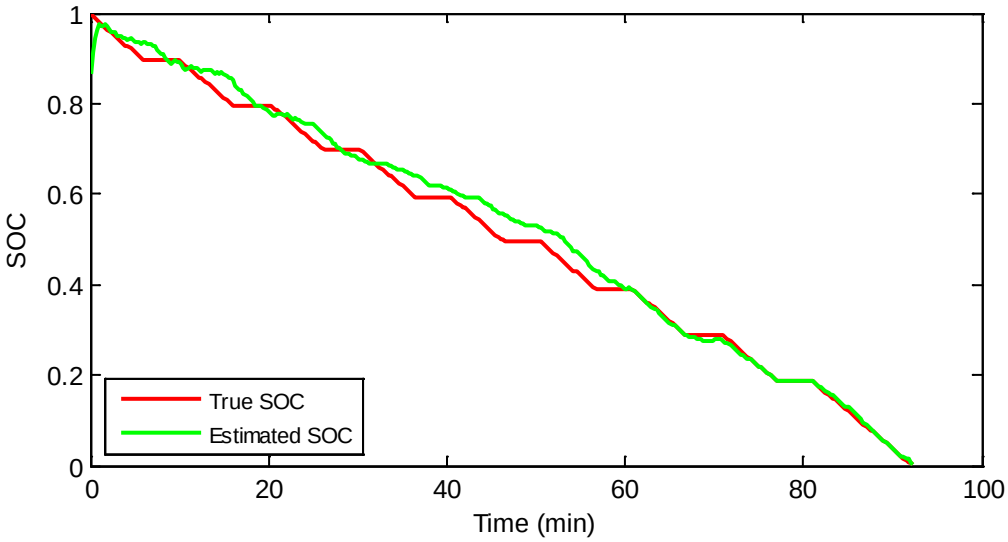

(h) Improved RC-hysteresis model (discharge)

Figure 4.21: SOC estimation results obtained for the1-A pulse discharging test for the discussed model at room temperature.

4.5.2 SOH Estimation Using EKF

Commonly, there are two parameters used as an indication of the battery condition compared to its new condition; the internal resistance and discharge capacity. The internal resistance increases as the battery ages, which can limit the power capability of the battery as the battery ages (power fade). The discharge capacity, on the other hand, decreases as the battery ages (capacity fade). To estimate the SOH through estimating the internal resistance and discharge capacity of the battery cell, simple EKF algorithms are constructed as discussed next.

4.5.2.1 Estimating the Internal Resistance

Assuming an accurate estimated SOC is obtained from one of the previous models, i.e. linear model, then, the internal resistance can be estimated through a simple EKF. The input and output equations of the state space model are constructed as follows:

$$R_{k+1} = R_k + \omega_k \tag{4.31}$$

$$y_k = \mathrm{OCV}(z_k) + R_k i_k + v_k \tag{4.32}$$

By applying the EKF algorithm on this set of equations, the internal resistance can be estimated. The results of a 1-A contentious current discharge test are shown in Figure 4.22 [(a) – (h)].

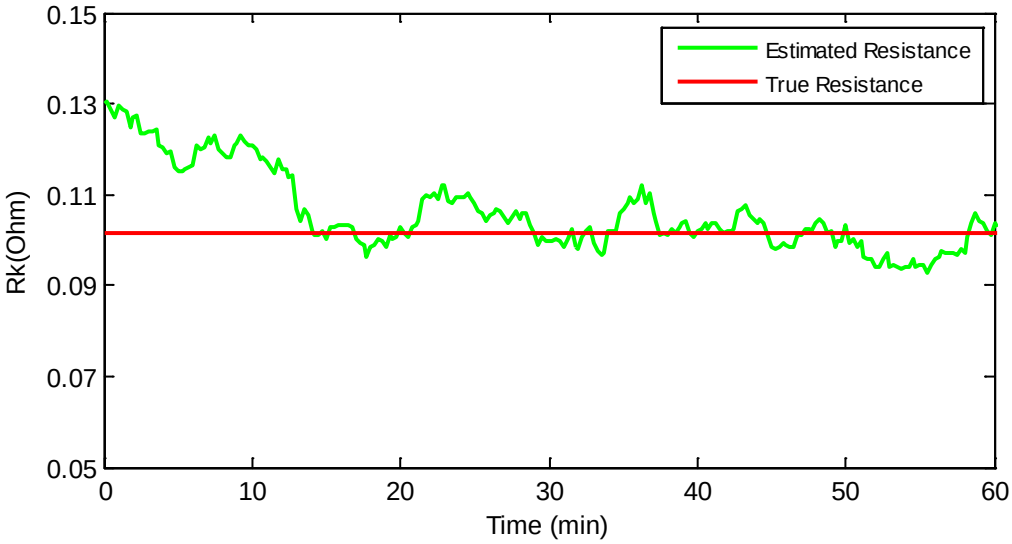

(a) R_0=0.13 Ohm, ω=0.05 and v=0.05

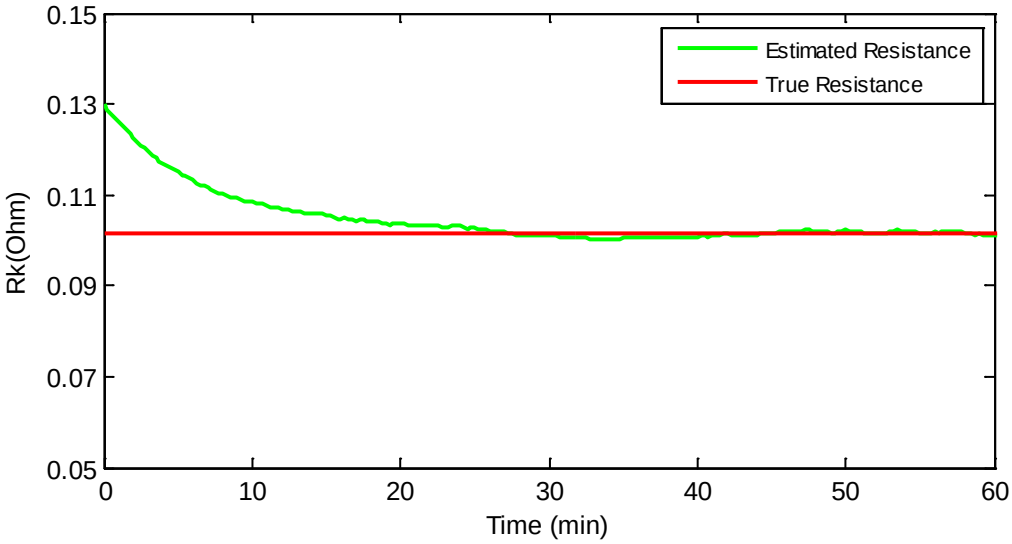

(b) R_0=0.13 Ohm, ω=0.005 and v=0.005

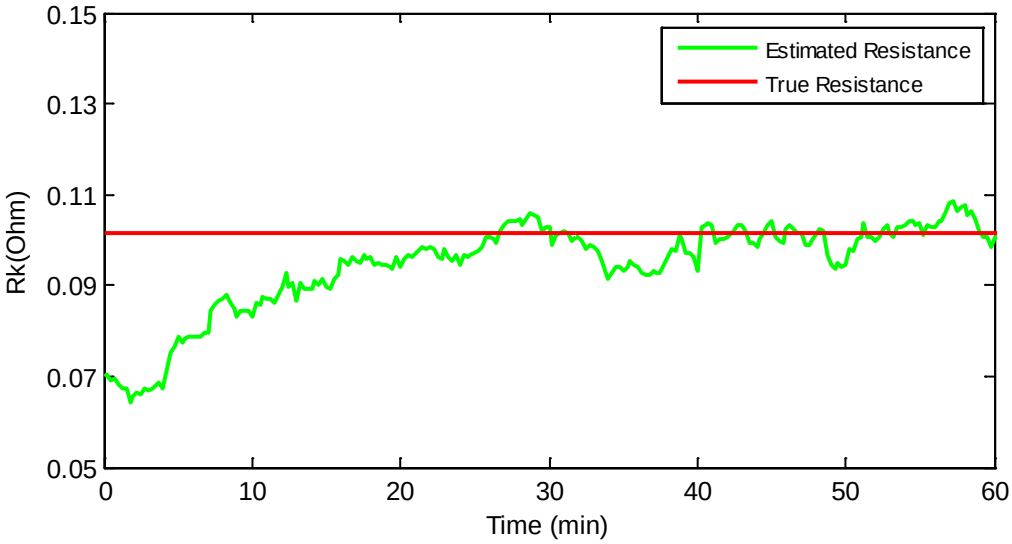

(c) R_0=0.07 Ohm, ω=0.05 and v=0.05

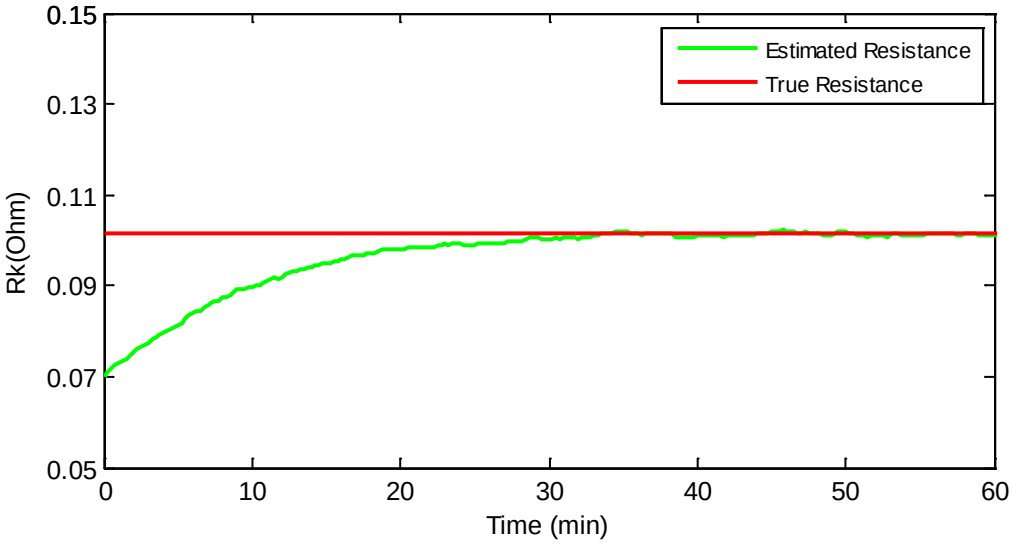

(d) R_0=0.07 Ohm, ω=0.005 and v=0.005

Figure 4.22: Internal resistance estimation for (a) R_0=0.13 Ohm, ω=0.05 and v=0.05, (b) R_0=0.13 Ohm, ω=0.005 and v=0.005, (c) R_0=0.07 Ohm, ω=0.05 and v=0.05 and (d) R_0=0.07 Ohm, ω=0.005 and v=0.005.

4.5.2.2 Estimating the Discharge Capacity

Similarly, to estimate the discharge capacity, a simple EKF algorithm is constructed for the following state space model input and output equations (assuming the linear model is used):

$$C_{k+1} = C_k + \omega_k \tag{4.33}$$

$$y_k = \mathrm{OCV}(z_k) + R_k i_k + v_k \tag{4.34}$$

where

$$z_k = z_{k-1} + \frac{\eta i_{k-1} \Delta t}{C_k} + v_k$$

Assume the SOC estimated values are fairly accurate, then, following equation is written as follows:

$$\left(f_k = z_k - z_{k-1} + \frac{\eta i_{k-1} \Delta t}{C_k} + v_k \right) \to 0$$

The value of f_k must converge to zero if the estimated capacity converged to its true value (provided accurate SOC and minimized process noise are guaranteed). Thus, the following equations can be written:

$$C_{k+1} = C_k + \omega_k$$

$$f_k = z_k - z_{k-1} + \frac{\eta i_{k-1} \Delta t}{C_k} + v_k \tag{4.35}$$

The purpose is to enforce the output equation to converge to zero to find the capacity. Again, assuming accurate SOC values are obtained, then, the capacity can be estimated. The results of a 1-A continuous discharge current test are shown in Figure 4.23 [(a) – (h)].

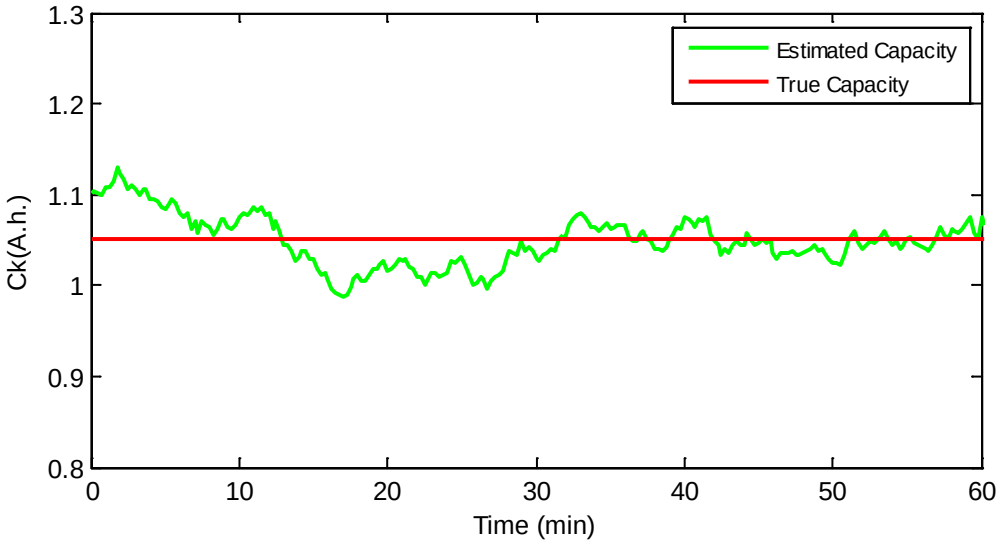

(a) C_0=1.1 A.h., ω=0.02 and v=0.02

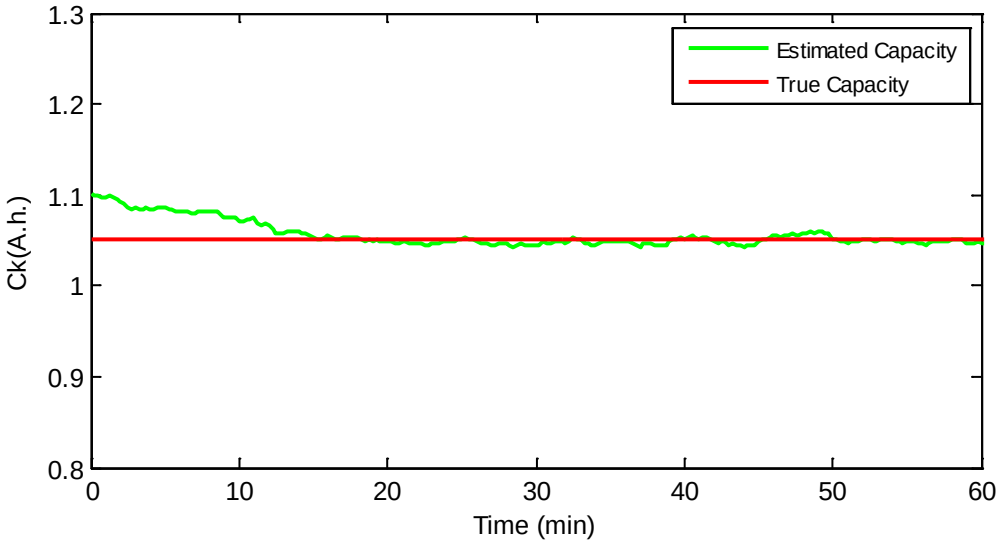

(b) C_0=1.1 A.h., ω=0.005 and v=0.005

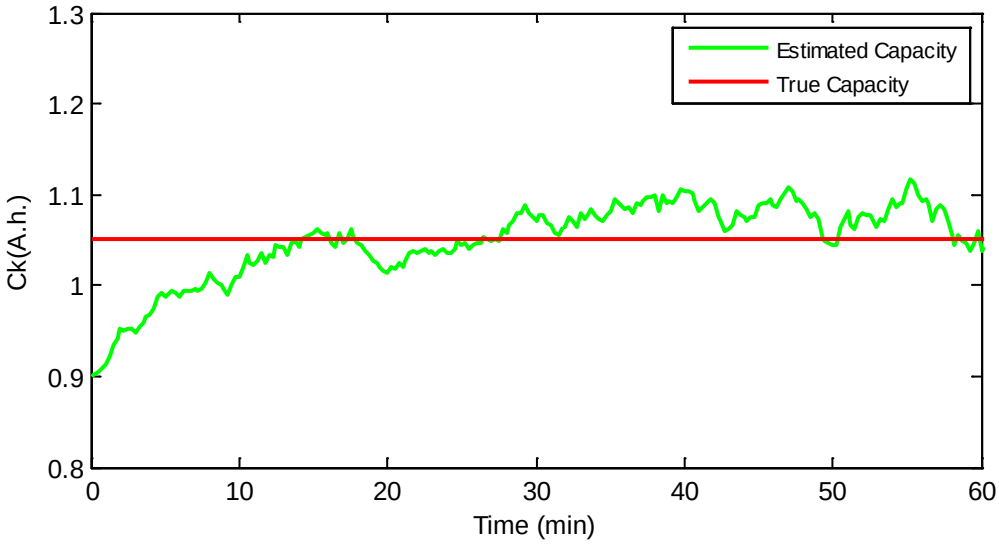

(c) C_0=0.9 A.h., ω=0.02 and v=0.02

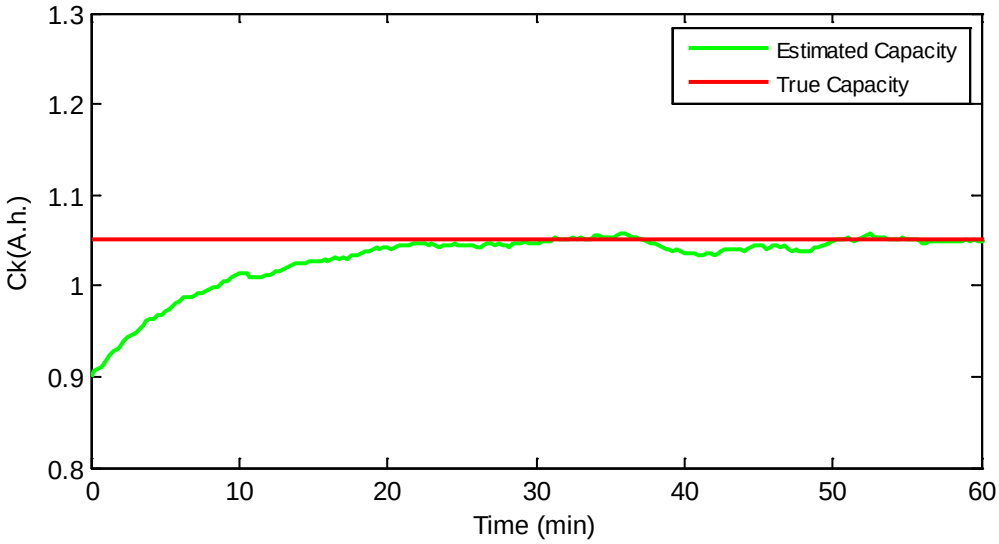

(d) C_0=0.9 A.h., ω=0.005 and v=0.005

Figure 4.23: Discharge capacity estimation for (a) C_0=1.1 A.h., ω=0.02 and v=0.02, (b) C_0=1.1 A.h., ω=0.005 and v=0.005, (c) C_0=0.9 A.h., ω=0.02 and v=0.02 and (d) C_0=0.9 A.h., ω=0.005 and v=0.005.

4.6 Ageing Effect and Parameters Adaptation

The results obtained in section 4.5.2 can be generalized to model the ageing effects on the parameters through the lifespan of the battery. The parameters such as OCV, R, η, h and τ will possibly change, at different rates, as the battery ages differently from a cell to another. To enforce the cell's parameters to adapt in real-time, the following state space model is constructed:

$$x_{k+1} = \begin{bmatrix} (\mathrm{OCV})_{k+1} \\ R_{k+1} \\ C_{k+1} \\ \eta_{k+1} \\ h_{k+1} \\ \tau_{k+1} \end{bmatrix} = \begin{bmatrix} 1 & 0 & 0 & 0 & 0 & 0 \\ 0 & 1 & 0 & 0 & 0 & 0 \\ 0 & 0 & 1 & 0 & 0 & 0 \\ 0 & 0 & 0 & 1 & 0 & 0 \\ 0 & 0 & 0 & 0 & 1 & 0 \\ 0 & 0 & 0 & 0 & 0 & 1 \end{bmatrix} \begin{bmatrix} (\mathrm{OCV})_{k} \\ C_{k} \\ R_{k} \\ \eta_{k} \\ h_{k} \\ \tau_{k} \end{bmatrix} + \begin{bmatrix} \omega_{OCV,k} \\ \omega_{C,k} \\ \omega_{R,k} \\ \omega_{\eta,k} \\ \omega_{h,k} \\ \omega_{\tau,k} \end{bmatrix}$$

$$y_k = h(z_k, i_k, h_k, \tau_k, T_k) + v_k$$

where x_k is the input vector and y_k is the model output voltage as a function of SOC, current, hysteresis, time constant and temperature. In the input equation, each parameter is a string of the parameter values different conditions, which can be expressed using vector matrices as follows:

$$(\mathrm{OCV})^T{}_{k+1} = \left[\mathrm{OCV}(z_1,T_1)_k \quad \ldots \quad \mathrm{OCV}(z_N,T_1)_k \quad \mathrm{OCV}(z_2,T_2)_k \quad \ldots \quad \mathrm{OCV}(z_N,T_M)_k\right]$$

$$R^T{}_{k+1} = \left[R(z_1,T_1)_k \quad \ldots \quad R(z_N,T_1)_k \quad R(z_2,T_2)_k \quad \ldots \quad R(z_N,T_M)_k\right]$$

$$C^T{}_{k+1} = \left[C(T_1)_k \quad C(T_2)_k \quad \ldots \quad C(T_M)_k\right]$$

$$\eta^T{}_{k+1} = \left[\eta(z_1,T_1)_k \quad \ldots \quad \eta(z_N,T_1)_k \quad \eta(z_2,T_2)_k \quad \ldots \quad \eta(z_N,T_M)_k\right]$$

$$h^T{}_{k+1} = \left[h(z_1,T_1)_k \quad \ldots \quad h(z_N,T_1)_k \quad h(z_2,T_2)_k \quad \ldots \quad h(z_N,T_M)_k\right]$$

$$\tau^{T}_{k+1} = \left[\tau(z_1, T_1)_k \quad \ldots \quad \tau(z_N, T_1)_k \quad \tau(z_2, T_2)_k \quad \ldots \quad \tau(z_N, T_M)_k \right]$$

Again, the parameters will converge to their true values if an accurate SOC is obtained.

4.7 Conclusions

This chapter proposed an empirical battery model with a very accurate output. The model, which is similar in its concept to some existent models but with an improved performance, is easily derived and is applicable to lithium batteries as well as other batteries, in general. The improvement in the proposed model is apparent during pulse (dis)charge events as a result of the addition of some new parameters such as the time constant and relaxation factor. Also, the model showed a good performance at elevated states of charge because the internal resistance was modeled not only as a function of current but also as a function of SOC. Further, the model parameters were found at a wide range of temperatures to validate the model at all possible temperatures.

After the model was developed, three EKFs algorithms were derived to estimate the SOC and SOH (internal resistance and discharge capacity). However, the errors obtained through estimating these quantities are expected and are a result of some modeling errors, which might be due to errors in modeling the OCV, internal resistance, or other parameters.

It is important to address the ageing effect in the model to enforce the parameters adapt to their true values through the lifespan of the battery. It is believed, however, that EKFs can be used to continuously estimate the parameters the same way the SOH was estimated provided an accurate SOC estimation mechanism is available. The EKF equations for the parameters adaption were briefly presented.

The analysis in this chapter was performed on an individual cell. However, every battery is different and its parameters might slightly differ even if they are identical. One way to minimize this variation among identical cells is by finding the parameters of different cells and averaging these parameters. This was not accomplished in this work since it is time consuming, but, it can be easily achieved by following the same procedure. Also, for large battery packs that consist of a large number of individual cells, more advanced circuitry and control algorithms must be considered to manage the battery pack operation.

CHAPTER FIVE: ENERGY MANAGEMENT WITH DISTRIBUTED RENEWABLE ENERGY SOURCES

5.1 Introduction

In Chapter 2, a dynamic economic model was proposed to manage the operation of the energy storage based on a certain criteria. In Chapters 3 and 4, a BMS that handles main functions including battery charging and SOC/SOH estimation was presented. In Chapter 5, load and weather forecasting models are proposed. These forecasting models, which are derived using ANNs, are necessary to optimize the operation of the MSS and to allow the owner of the distributed system (including storage and renewable sources) to schedule a power exchange plan with the grid. The goal in the following sections is to develop an operation strategy for the MSS when operated in a spot market electricity system, which can be achieved through employing the dynamic economic model, battery model and forecasting models in the EMS.

5.2 System Description

The distributed system is shown in Figure 5.1. The load, which is assumed to be a house (or any other electricity consumer), renewable DG sources (solar PV and wind) and a MSS are connected to the main utility grid through a common AC bus as shown. Basically, the EMS must minimize the usage of storage and conventional power plants (utility) and maximize the usage of renewable sources. Further, the EMS must optimize the scheduling of the MSS operation by making smart decisions that allow maximizing the economic return, which can be achieved by

utilizing the variation in the spot electricity prices, maximizing the battery lifetime, and transacting power with the utility.

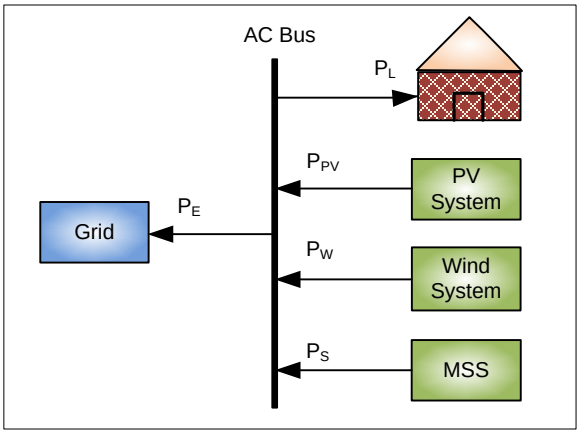

Figure 5.1: A general distributed system. Arrows' directions indicate positive values of variables.

Figure 5.2 shows a functional block diagram for the EMS. The dynamic economic model is responsible for scheduling a power exchange plan with the spot market after the load and weather forecasts as well as the spot prices for a given time horizon are all received. Then, the exchange plan is scheduled.

The assumptions made in the proposed EMS are as follows:

1. The reactive power is ignored.
2. The transmission lines are assumed to have an infinite capacity.
3. All quantities in Figure 5.1 have positive values (except for P_S and P_E, which can be positive or negative depending on whether they act as a source or load).

The power balance equation is:

$$P_E(\mathrm{t}) = P_{PV}(\mathrm{t}) + P_W(\mathrm{t}) + P_S(\mathrm{t}) - P_L(\mathrm{t}) \tag{5.1}$$

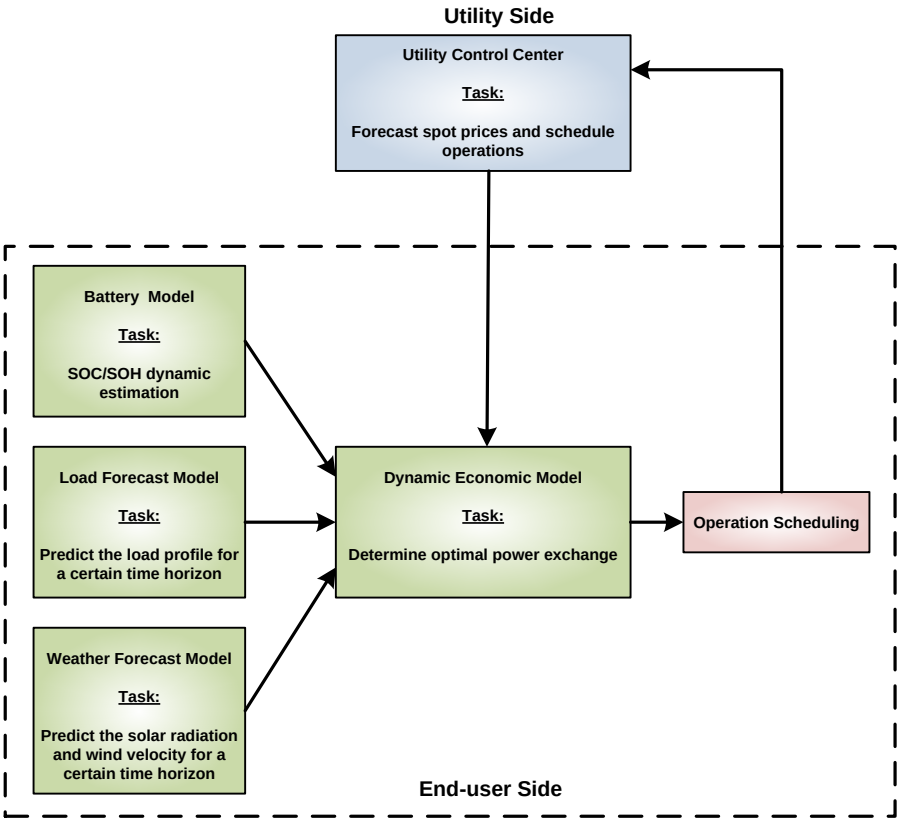

Figure 5.2: A functional block diagram of the EMS.

The daily return equation that must be maximized is given as follows:

a) For $P_G > P_L$:

$$Max.\left\{R = (SP)_H .(C)_{disch} - (SP)_L .(C_{ch}) + (SP).(P_G - P_L).(\Delta t)\right\} \quad , \quad P_G > P_L \qquad (5.2)$$

b) For $P_G < P_L$:

$$Max.\left\{R = (SP)_H .(C)_{disch} - (SP)_L .(C_{ch})\right\} \quad , \quad P_G < P_L \qquad (5.3)$$

where P_G is equal to P_{PV} + P_W and Δt is the time increment which is assumed to be one hour. The power exchange constraints that must be met under any circumstances are (Equation 5.7 is from the dynamic model in Chapter 2):

$$\text{Max. (dis)charge rate} = \frac{C}{4} \qquad (5.4)$$

$$(\mathrm{SOC})_{\max} \leq 100\% \tag{5.5}$$

$$(\mathrm{SOC})_{\min} \geq 20\% \tag{5.6}$$

$$R_p > R_{min} \tag{5.7}$$

As an assumption, the daily bids for sale and purchase of energy must be provided to the power pool no later than 12 hours before the scheduled day of operation, as in the Nordic spot market. This assumption will be used in section 5.4 when the operation scheduling is considered.

5.3 Forecasting Models Using Artificial Neural Networks

Previously, EKFs were used to predict the battery inner states and parameters. In fact, Kalman filters are advantageous in predicting the performance of a dynamic system when a very accurate model of the system is available. In this section, forecasting models for the electric load and weather are proposed. However, since an accurate model is very difficult (if not impossible) to obtain for such kind of problems, another technique is used to derive these models.

Artificial neural networks (ANNs) were found to be very adequate to solve forecasting problems provided historical data is provided. An ANN is a computational model that resembles the human brain in the way of learning and making decisions. They employ a massive interconnection of simple computing cells referred to as neurons (or processing units). The power of ANNs comes from two things; first, its massively parallel distributed structure, and second; its ability to learn and thus generalize [60].

In addition, ANNs offer some desired capabilities such as that they can be used in nonlinear systems, input-output mapping, adaptive. An example of a feed forward ANN is a simple two-layer network (see Figure 5.3). In this network, which consists of two visible layers

(input and output) and one hidden layer and a number of neurons in the input, output and hidden layers. The weight functions $\{w_{11}, w_{12}, w_{13}, w_{21}, w_{22}$, and $w_{23}\}$ interconnect the input layer with the hidden layer, where the weight functions $\{w_1, w_2$, and $w_3\}$ interconnect the hidden layer with the output layer. This model will be used in this section to develop forecasting models for load and weather but with more inputs and neurons.

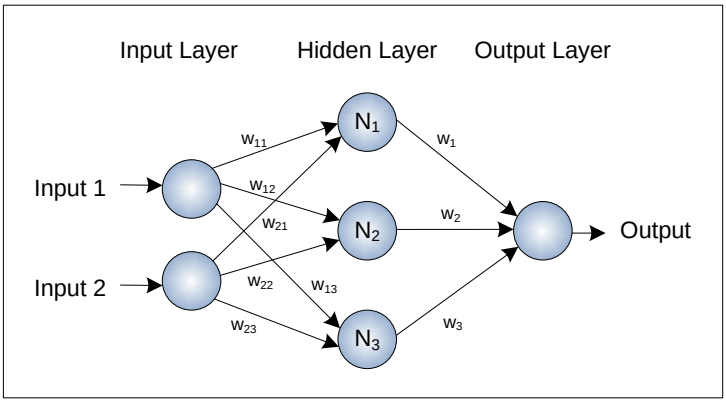

Figure 5.3: A simple two-layer feed-forward ANN.

Next, four models are proposed for forecasting the electric load, solar radiation wind speed and wind direction. These models, however, can be adjusted and used for any time horizon (12-hours, 24-hours, 48-hours, etc.). As a rule-of-thumb, as the forecasting time horizon increases, the uncertainty will increase accordingly.

5.3.1 Hourly Load Forecasting Model

Some data were imported from [62] and used to train, validate and test the model. This data compromises the following for years 2008, 2009 and 2010:

- Day hour
- Week day
- Holiday or weekend flag (1/0 values are used)
- Dew point temperature
- Dry bulb temperature
- Previous day average load
- Same-hour previous-day load
- Same-hour same-day previous-week load

A model similar to the one shown in Figure 5.3 was created in MATLAB with eight inputs and 20 neurons in the hidden layer. To test the performance of the developed model, four different five-day periods were selected and the actual load versus the predicted load was plotted. The results are shown in Figure 5.4 [(a) through (d)].

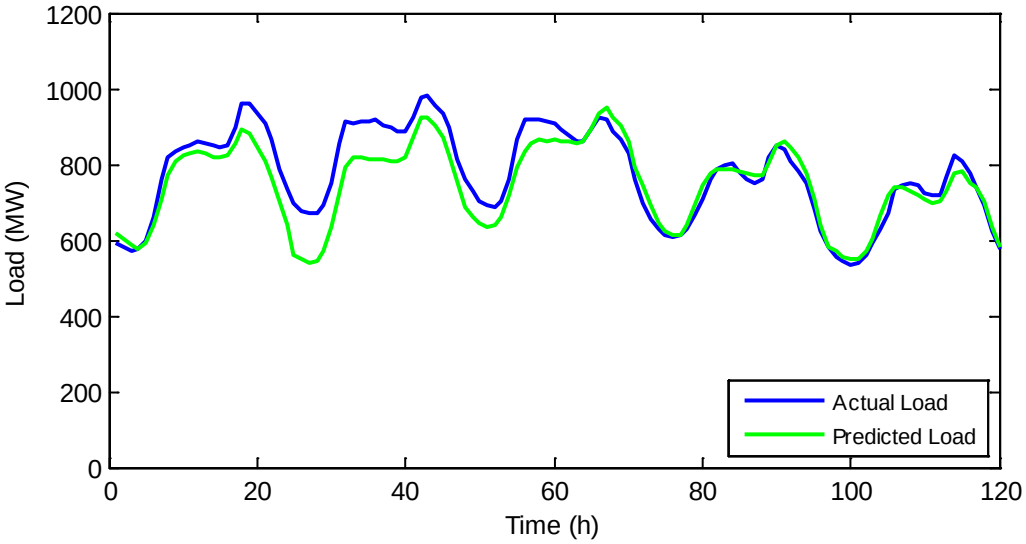

(a) Days from 1/2/2008 to 1/6/2008

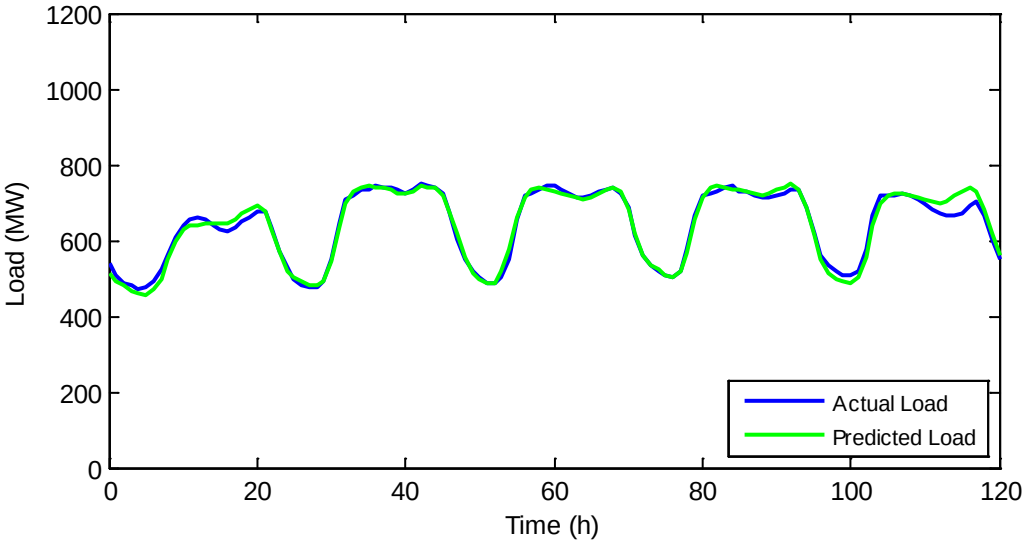

(b) Days from 4/5/2009 to 4/9/2009

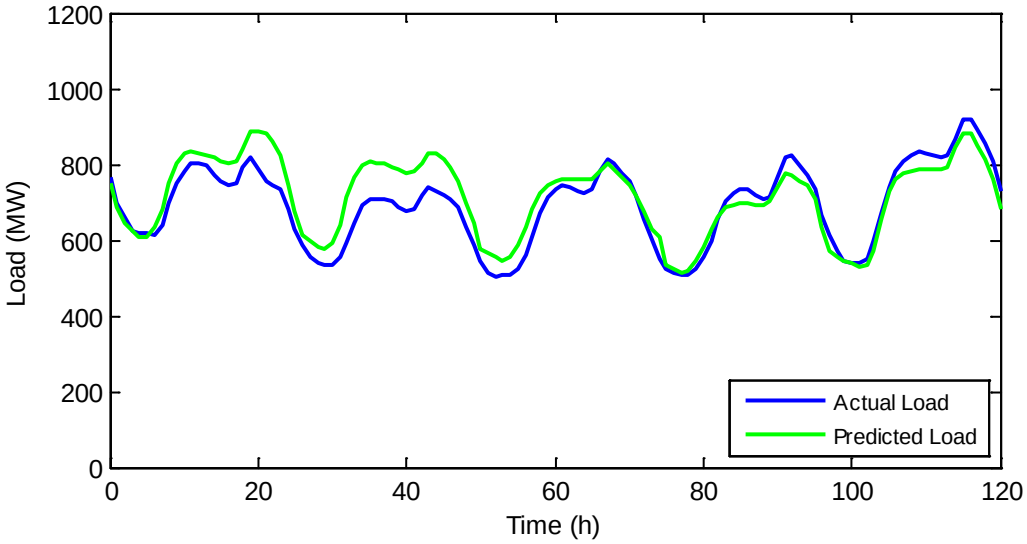

(c) Days from 12/24/2009 to 12/28/2009

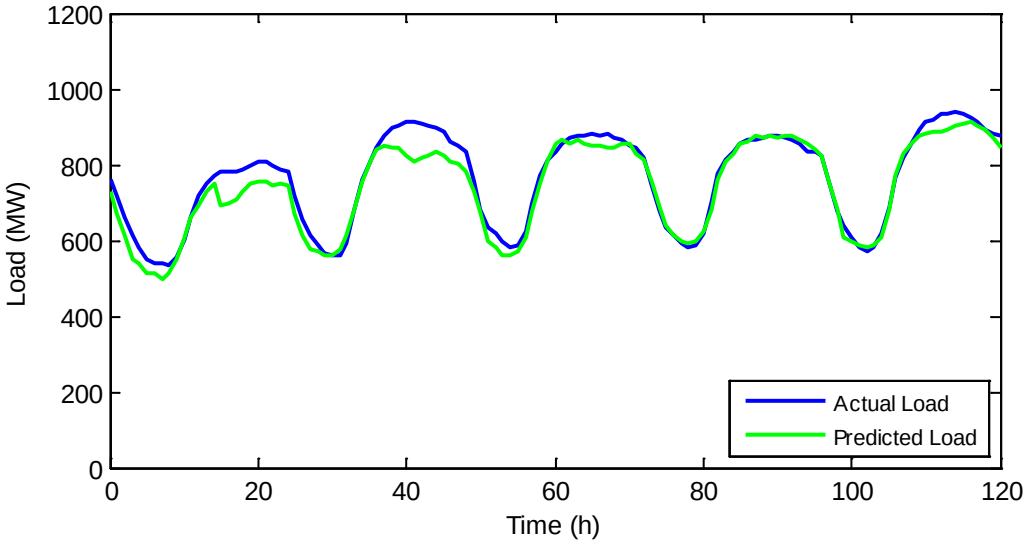

(d) Days from 7/11/2010 to 7/15/2010

Figure 5.4: Load prediction for four different five-day periods for a 24-hour forecasting time horizon.

Figure 5.5 shows the correlation between the predicted load and the actual load for the hourly load data for years 2008, 2009 and 2010.

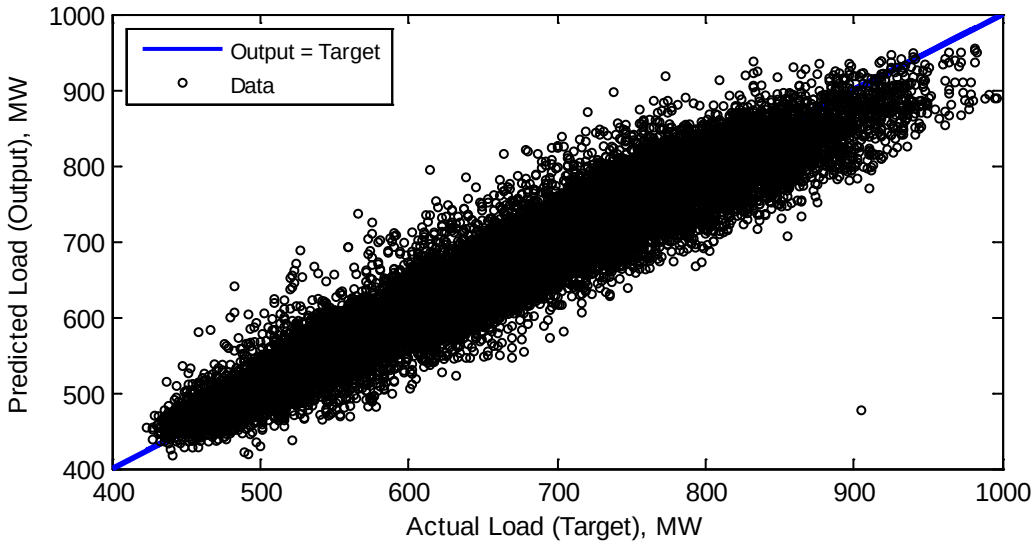

Figure 5.5: Correlation between the predicted load (output) and actual load (target) for day-ahead time horizon.

For the day-ahead time horizon, the root mean square error (RMSE) is 31.34 MW and the correlation between the actual load (target) and predicted load (output) is 0.959. Table 5.1 lists the RMSE and the correlation values between the actual load (target) and the predicted load (output) for different time horizons.

Table 5.1: Load RMSE and correlation (*r*) for different forecasting horizons.

Forecast horizon	*RMSE* (MW)	*r*
1-hour	20.69	0.983
6-hour	23.51	0.978
12-hour	29.28	0.966
24-hour	31.34	0.959
48-hour	36.95	0.945

5.3.2 Hourly Weather Forecasting Model

In a similar way, three weather forecasting models for the solar radiation, wind speed and wind direction were developed. In these models, some historical data [63] for the years 2008, 2009, and 2010 was imported for the purpose of training, validating and testing the model. A model similar to the one shown in Figure 5.6 was created with 11 inputs and 20 neurons in the hidden layer.

5.3.2.1 Hourly Solar Radiation Forecasting Model

This model uses the following data as inputs:

- Day hour
- Air temperature
- Dew point temperature
- Global solar radiation
- Wind direction
- Wind run
- Wind peak gust
- Relative humidity
- Precipitation
- Solar radiation of same hour previous day
- Solar radiation of same hour same day previous week

The results of this model for four different five-day periods are shown in Figure 5.6 [(a) through (d)]. (1 Langely per hour = 11.63 Watt/square meter = 1 Cal/cm2).

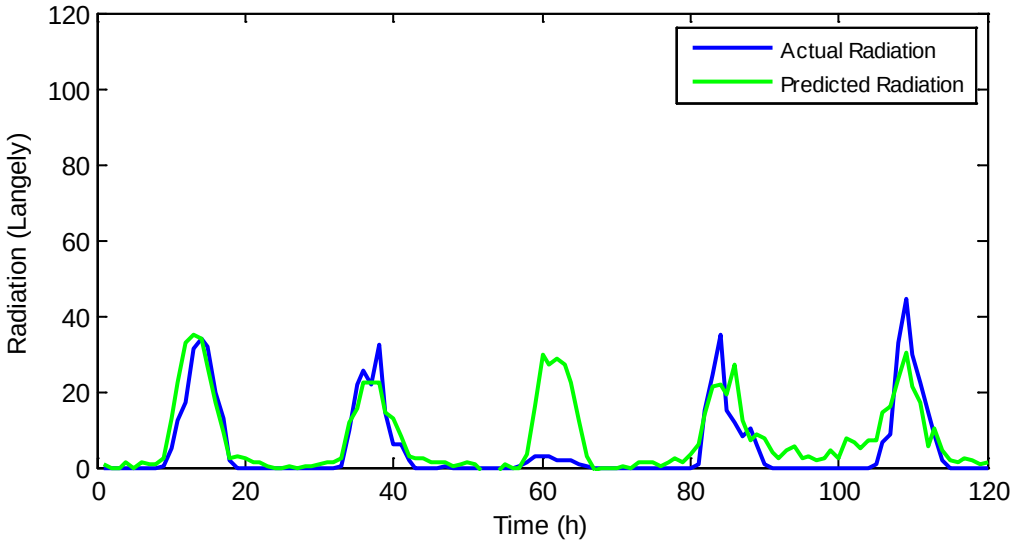

(a) Days from 1/2/2008 to 1/6/2008

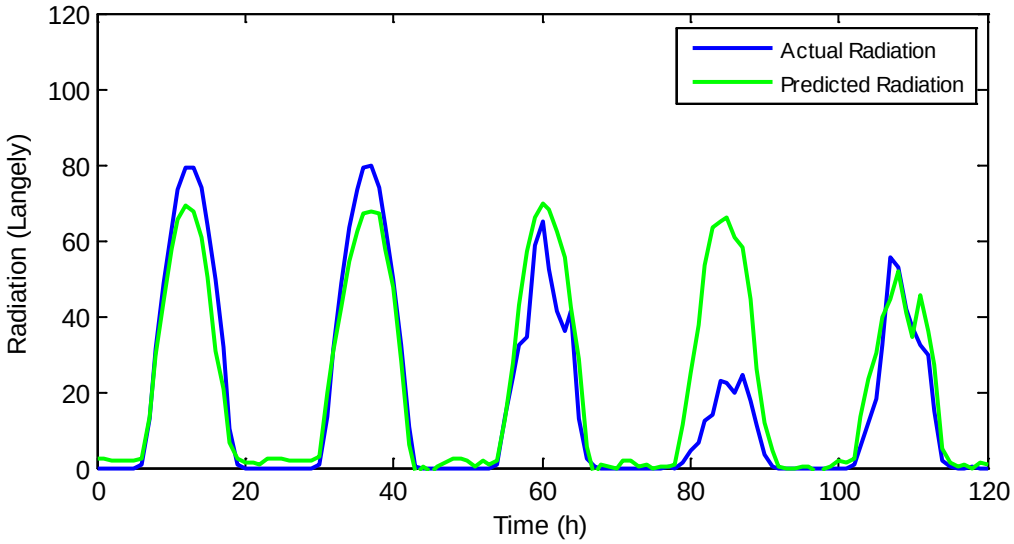

(b) Days from 4/5/2009 to 4/9/2009

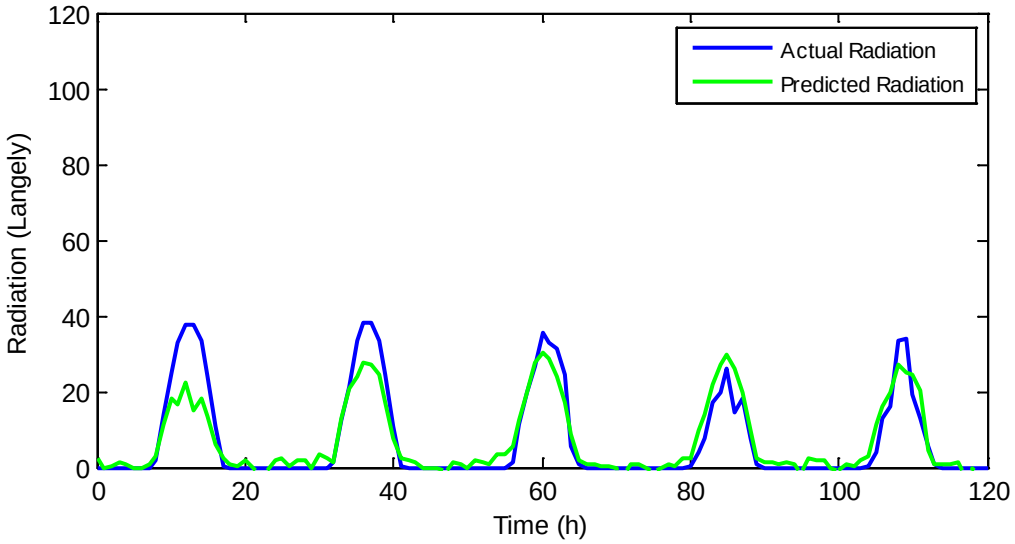

(c) Days from 12/24/2009 to 12/28/2009

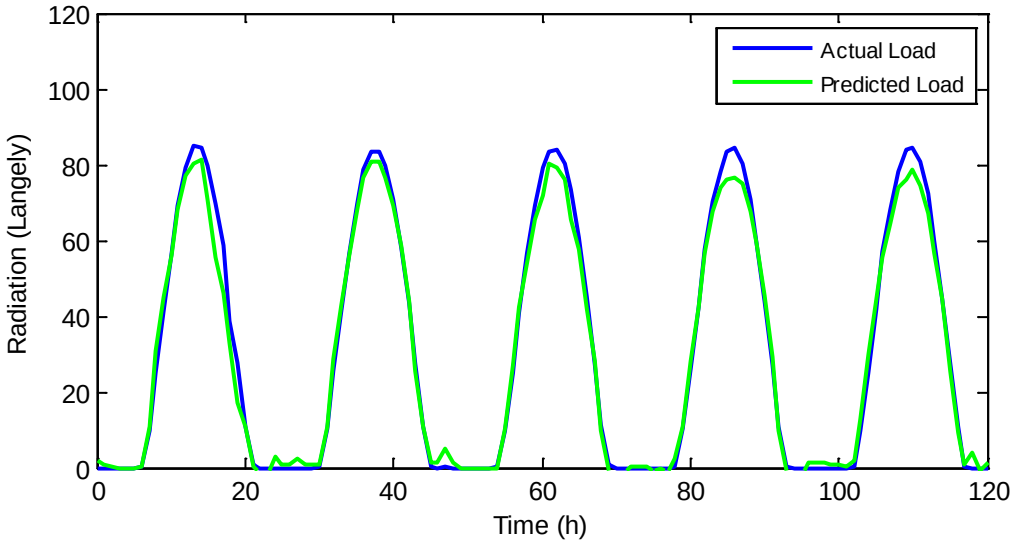

(d) Days from 7/11/2010 to 7/15/2010

Figure 5.6: Solar radiation prediction for four different five-day periods for a 24-hour forecasting time horizon.

Figure 5.7 shows the correlation between the predicted radiation and the actual radiation for the hourly solar radiation data for years 2008, 2009 and 2010. Note that the forecasting accuracy is better in summer because the possibility of a cloudy sky is low.

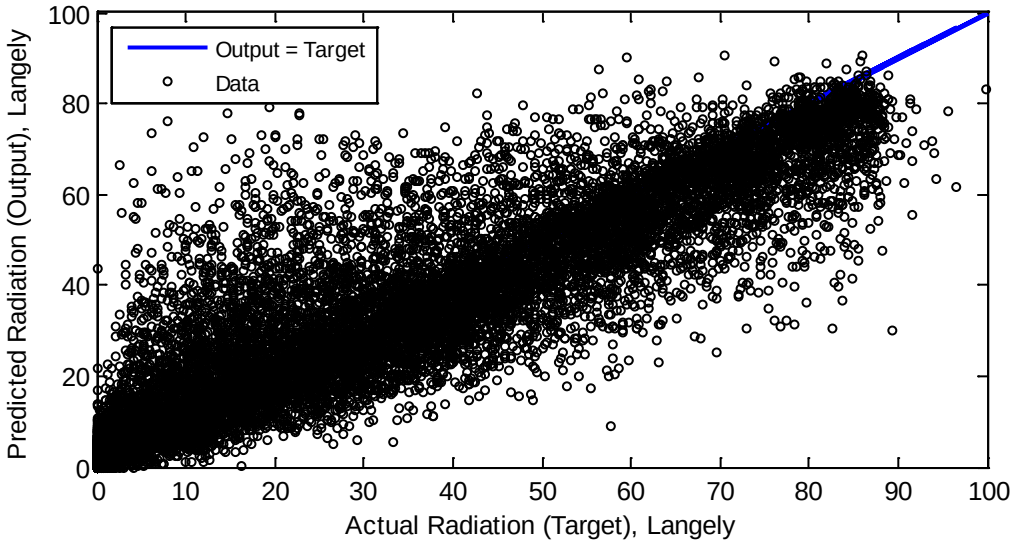

Figure 5.7: Correlation between the predicted solar radiation (output) and actual solar radiation (target) for day-ahead time horizon.

For the day-ahead time horizon, the RMSE is 8.68 Langely and the correlation between the actual radiation (target) and predicted radiation (output) is 0.94. The values of the RMSE and correlation between the actual radiation (target) and predicted radiation (output) for other time horizons are listed in Table 5.2.

Table 5.2: Solar radiation RMSE and correlation (*r*) for different forecasting horizons.

Forecast horizon	*RMSE* (Langely)	*r*
1-hour	7.64	0.954
6-hour	7.96	0.949
12-hour	8.29	0.946
24-hour	8.68	0.94
48-hour	8.94	0.936

5.3.2.2 Hourly Wind Speed Forecasting Model

This model uses the following data as inputs:

- Day hour
- Air temperature
- Dew point temperature
- Global solar radiation
- Wind direction
- Wind run
- Wind peak gust
- Relative humidity
- Precipitation
- Wind speed of same hour previous day
- Wind speed of same hour same day previous week

The results of this model for four different five-day periods are shown in Figure 5.8 [(a) through (d)].

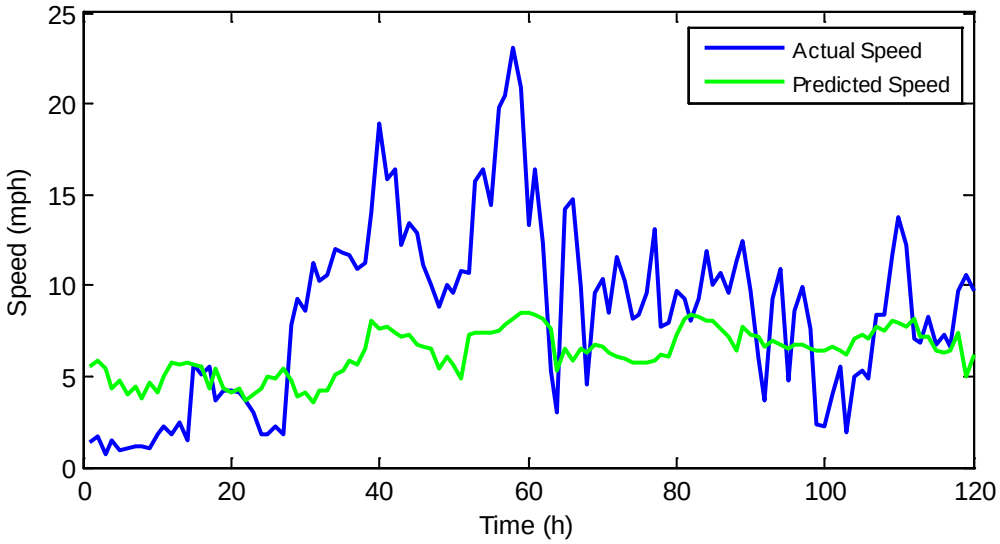

(a) Days from 1/2/2008 to 1/6/2008

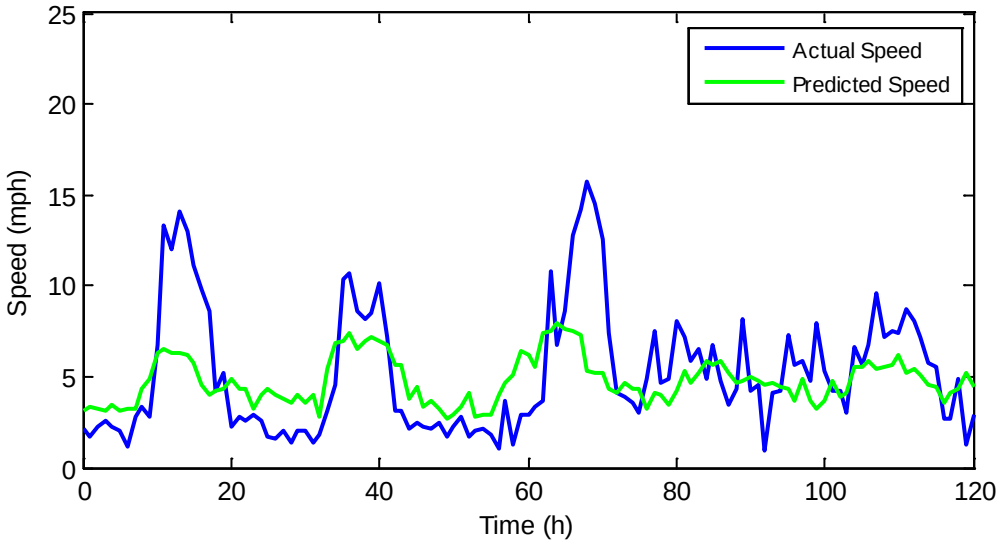

(b) Days from 4/5/2009 to 4/9/2009

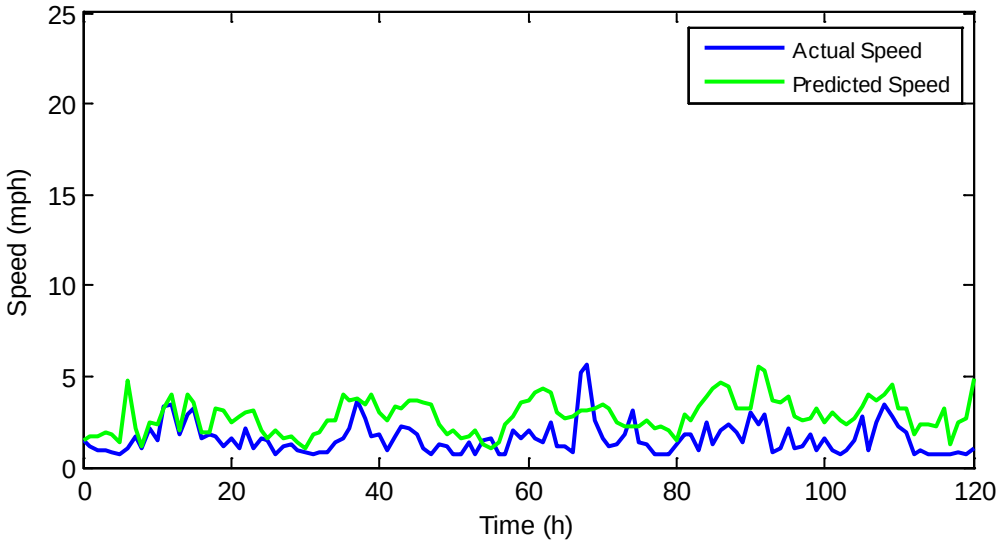

(c) Days from 12/24/2009 to 12/28/2009

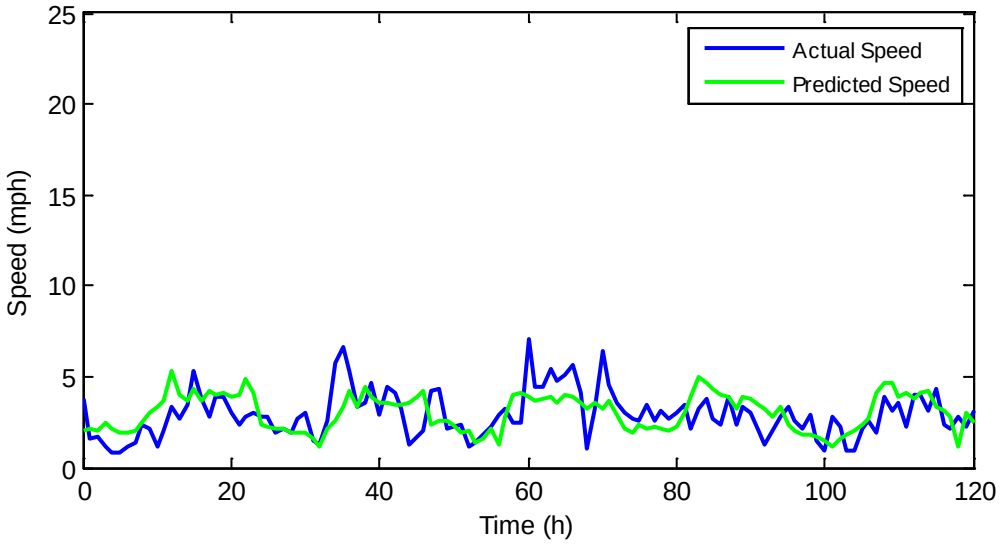

(d) Days from 7/11/2010 to 7/15/2010

Figure 5.8: Wind speed prediction for four different five-day periods for a 24-hour forecasting time horizon.

Figure 5.9 shows the correlation between the predicted speed and the actual speed for the hourly wind speed data for years 2008, 2009 and 2010. Obviously, the wind speed model performs better at low speeds, where at sudden high speeds, its performance is poor.

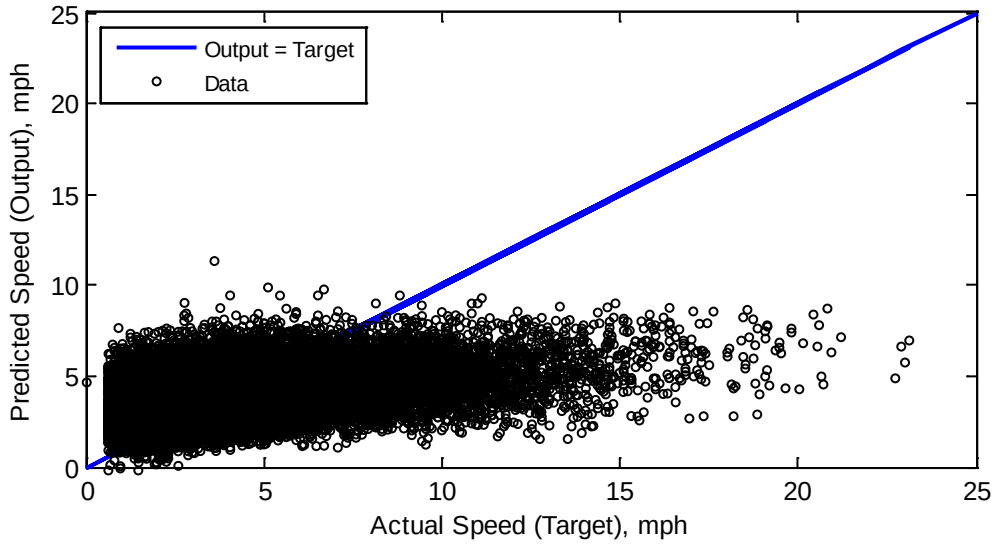

Figure 5.9: Correlation between the predicted wind speed (output) and actual wind speed (target) for day-ahead time horizon.

For day-ahead time horizon, the RMSE is 2.56 mph and the correlation between the actual speed (target) and predicted speed (output) is 0.444. Other values for the RMSE and the correlation between the actual speed (target) and the predicted speed (output) for other time horizons are listed in Table 5.3.

Table 5.3: Wind speed RMSE and correlation (*r*) for different forecasting horizons.

Forecast horizon	*RMSE* (mph)	*r*
1-hour	1.62	0.823
6-hour	2.22	0.631
12-hour	2.4	0.537
24-hour	2.56	0.465
48-hour	2.58	0.43

5.3.2.3 Hourly Wind Direction Forecasting Model

This model uses the following data as inputs:

- Day hour
- Air temperature
- Dew point temperature
- Global solar radiation
- Wind direction
- Wind run
- Wind peak gust
- Relative humidity
- Precipitation
- Wind direction of same hour previous day
- Wind direction of same hour same day previous week

The results of this model for four different five-day periods are shown in Figure 5.10 [(a) through (d)].

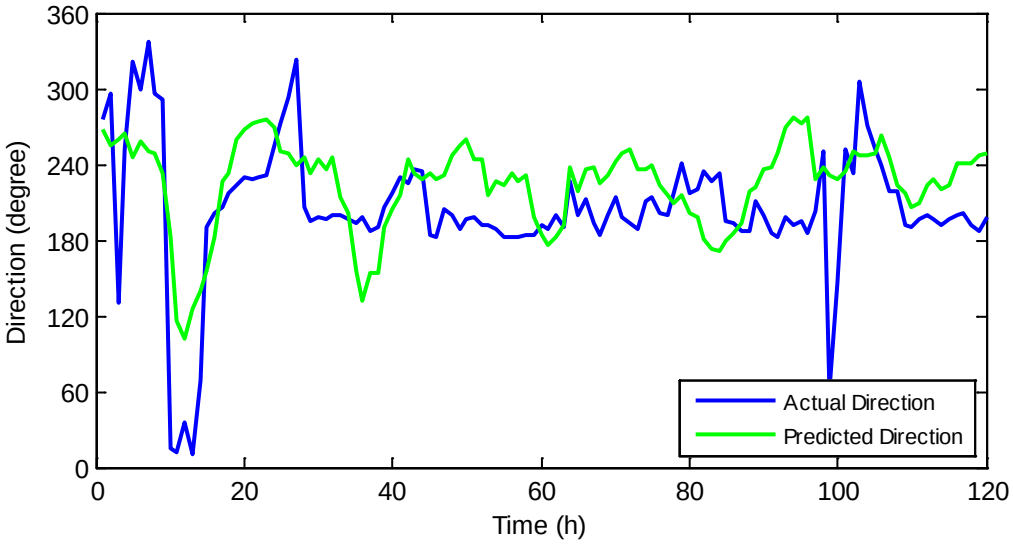

(a) Days from 1/2/2008 to 1/6/2008

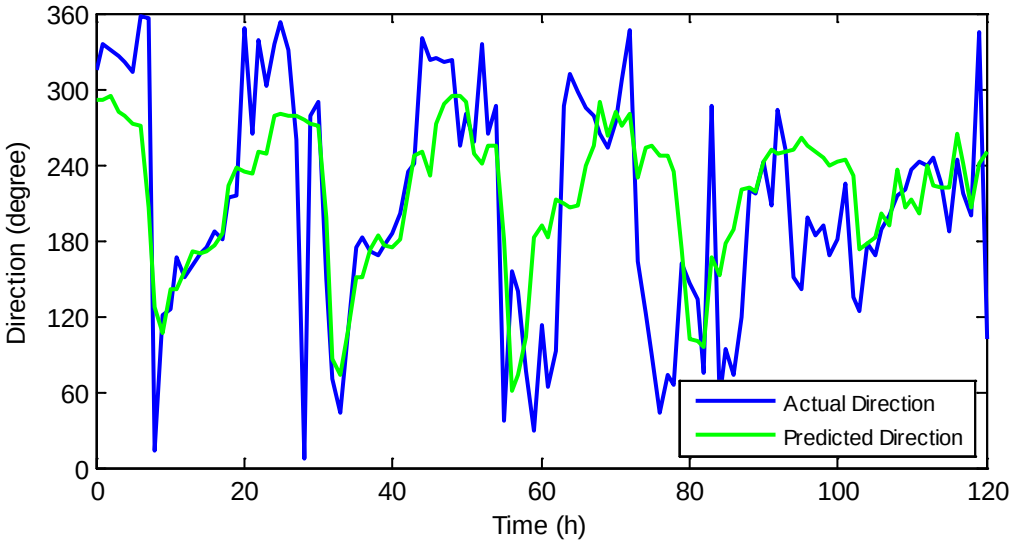

(b) Days from 4/5/2009 to 4/9/2009

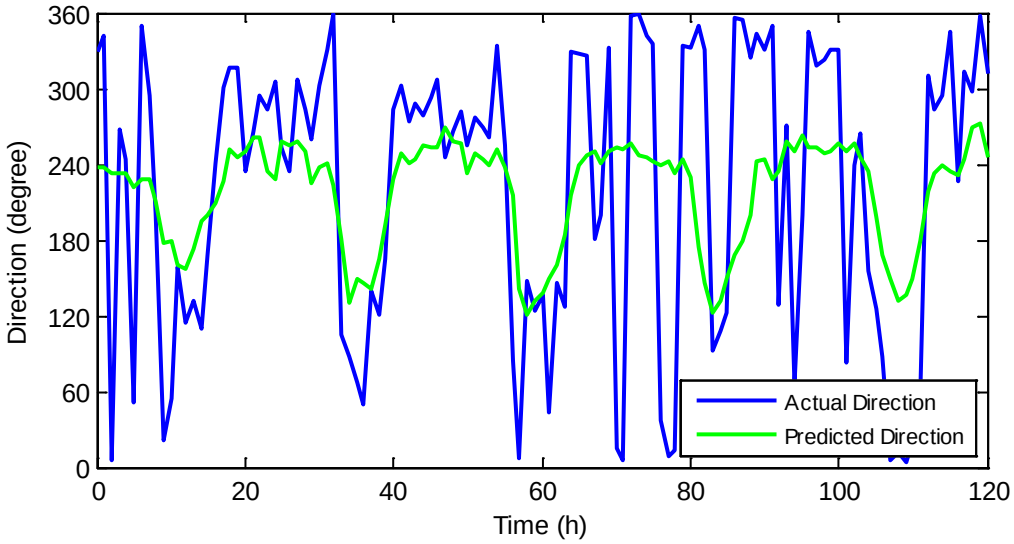

(c) Days from 12/24/2009 to 12/28/2009

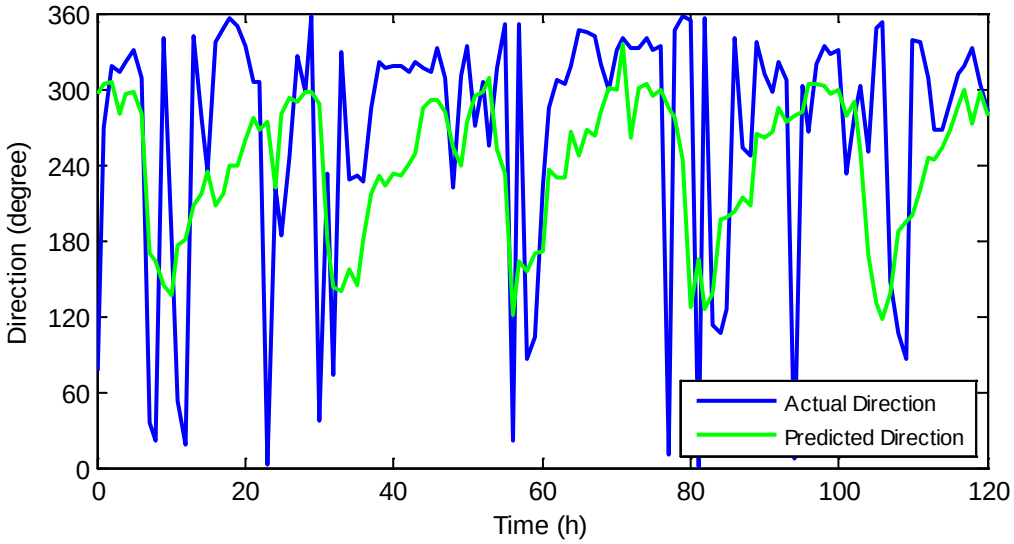

(d) Days from 7/11/2010 to 7/15/2010

Figure 5.10: Wind direction prediction for four different five-day periods for a 24-hour forecasting time horizon.

Figure 5.11 shows the correlation between the predicted direction and the actual direction for the hourly wind direction data for years 2008, 2009 and 2010.

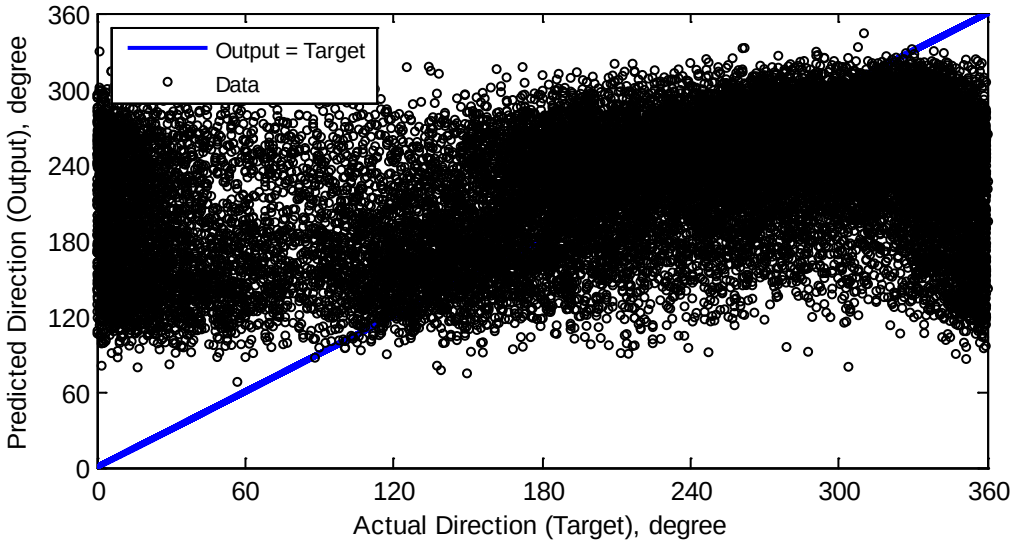

Figure 5.11: Correlation between the predicted wind direction (output) and actual wind direction (target) for day-ahead time horizon.

The RMSE is 93.4 degrees and the correlation between the actual angle (target) and predicted angle (output) is 0.46 for the day-ahead time horizon. For other time horizons, the RMSE and the correlation between the actual wind direction (target) and the predicted wind direction (output) are listed in Table 5.4.

Table 5.4: Wind direction RMSE and correlation (*r*) for different forecasting horizons.

Forecast horizon	*RMSE* (degree)	*r*
1-hour	84.6	0.591
6-hour	91.2	0.489
12-hour	92.7	0.484
24-hour	93.4	0.46
48-hour	93.8	0.441

5.4 Operation Strategy

There are two modes for the MSS operation; scheduling and real-time operations. In the scheduling operation, the goal is simply to schedule an exchange plan with the spot market, while the goal for the later operation is to follow the scheduled plan. More details about these two operation modes are presented next.

5.4.1 Scheduling Operation

The operation is scheduled every day at a specific hour. The purpose is to find the optimum power exchange plan between the MSS and the utility grid. This can be achieved for different time horizons (i.e. half day, one day, two days, etc.). However, there is a tradeoff between increasing the time horizon and the accuracy of the forecasts, which was noticed in the previous section. Figure 5.12 shows the scheduling timeline for both 24-h and 48-h time horizons cases.

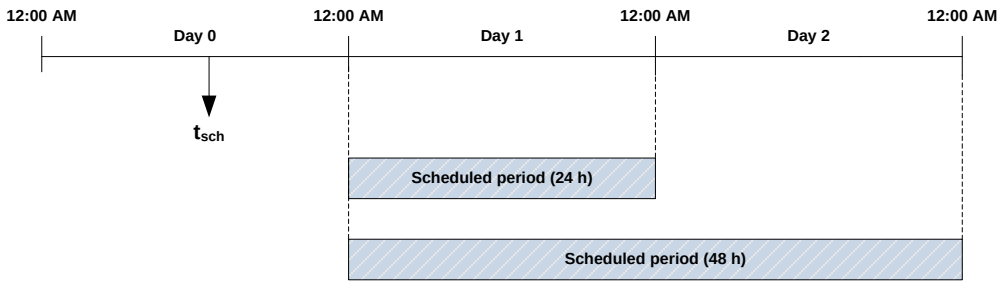

Figure 5.12: Scheduling time horizons.

The scheduling operation is illustrated through a flowchart diagram as shown in Figure 5.13. The scheduling operation is summarized as follows:

- The scheduling is performed at the scheduling time one day before the operation day.

- The spot prices, weather and load forecasts as well as the estimated initial battery SOC and SOH for the operation day are all loaded.
- The maximum possible return for exchanging power with the grid is calculated and based on that, the operation schedule is determined.

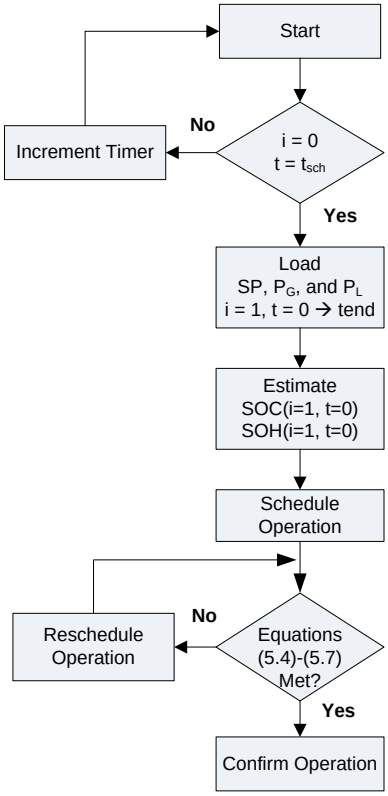

Figure 5.13: Flowchart of the scheduling operation.

5.4.2 Real-time Operation

In the real-time operation, the objective is to enforce the distributed system including the MSS to match the scheduled plan. This operation is summarized in Table 5.5.

Table 5.5: Real-time operation equations.

Mode	*Equation*
Charge ($SP < SP_{min}$)	$C_{k+1} = C_k + I_{const} . \Delta t$
Correction ($SP > SP_{min}$ and $R < R_{min}$)	$C_{k+1} = C_k + K. \Delta t$
Discharge ($SP > SP_{max}$ and $R > R_{min}$)	$C_{k+1} = C_k - I_{const} . \Delta t + K. \Delta t$

where I_{const} is a positive constant (dis)charge current drawn from the grid or DG, and K is a correction gain, which is defined as follows:

$$K = \begin{cases} e_1 - e_2 & , \ e_2 > 0 \\ 0 & , \ e_2 \leq 0 \end{cases} \tag{5.8}$$

where e_1 and e_2 indicate the difference between the real and estimated DG and load power, and are defined as follows:

$$e_1 = P_{G,real} - P_{L,real} \tag{5.9}$$

$$e_2 = P_{G,est} - P_{L,est} \tag{5.10}$$

The online operation of the MSS is shown in Figure 5.14.

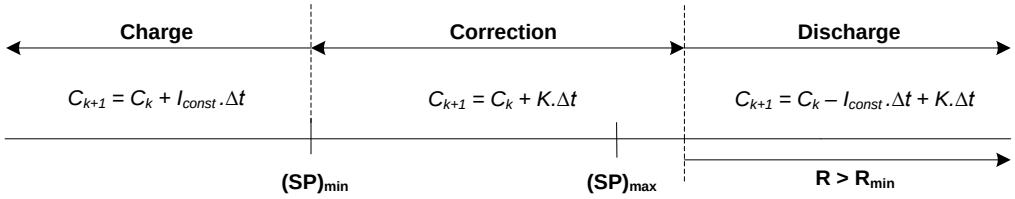

Figure 5.14: Real-time MSS operation schemes vs. SP. The term ($K. \Delta t$) represents the error in the DG forecast which is compensated by the MSS.

5.5 System Simulation

To examine the proposed operation strategy via simulation, the following parameters, which can fit a typical residential application, were selected.

Table 5.6: System sizing for a simulation example.

Component	*Size*
MSS Capacity	10 kWh
MSS Power Converter	2.5 kW
PV system	2.4 kW
Wind system	1.5 kW

5.5.1 System's Inputs

The load and DG (PV and wind) power values were derived logically from the data obtained to derive the forecasting models. The developed forecasting models were used to estimate the load and DG power for four different days. This data is summarized in the following tables for the four different days.

Table 5.7: Load power on day 1.

Hour	P_L	$P_{L,est}$	*Hour*	P_L	$P_{L,est}$
0	1776	2086.5	12	2559	2504.7
1	1740	2023.2	13	2544	2528.4
2	1713	1960.8	14	2529	2566.5
3	1722	1959	15	2547	2635.2
4	1794	1955.7	16	2691	2739.9
5	1974	1997.7	17	2883	2758.2
6	2280	2118.9	18	2886	2712
7	2451	2242.8	19	2799	2667.3
8	2499	2345.4	20	2730	2609.4
9	2532	2394	21	2592	2519.4
10	2550	2431.2	22	2355	2397.6
11	2580	2522.4	23	2199	2236.2

Table 5.8: Load power on day 2.

Hour	P_L	$P_{L,est}$	*Hour*	P_L	$P_{L,est}$
0	1521	1410	12	1962	1886.4
1	1467	1390.2	13	1923	1884
2	1437	1356.9	14	1890	1879.2
3	1419	1330.5	15	1875	1884.9
4	1428	1346.1	16	1902	1915.8
5	1482	1420.2	17	1953	1974
6	1572	1508.1	18	1977	2045.4
7	1689	1642.2	19	2025	2080.2
8	1827	1788.3	20	2025	2016.6
9	1926	1874.4	21	1899	1866.9
10	1959	1877.1	22	1707	1692.6
11	1983	1876.2	23	1584	1523.4

Table 5.9: Load power on day 3.

Hour	P_L	$P_{L,est}$	*Hour*	P_L	$P_{L,est}$
0	2097	2068.5	12	2388	2546.7
1	1983	2037.9	13	2319	2525.4
2	1878	1961.7	14	2271	2503.2
3	1851	1909.5	15	2238	2492.1
4	1848	1906.5	16	2250	2494.2
5	1836	1976.7	17	2376	2568.9
6	1923	2116.5	18	2448	2691
7	2097	2337.9	19	2361	2695.2
8	2253	2492.4	20	2268	2661.3
9	2349	2556	21	2235	2605.5
10	2409	2569.5	22	2199	2499
11	2409	2563.8	23	2043	2275.8

Table 5.10: Load power on day 4.

Hour	P_L	$P_{L,est}$	*Hour*	P_L	$P_{L,est}$
0	2148	2088.6	12	2250	2126.1
1	1986	1960.2	13	2307	2131.8
2	1833	1717.8	14	2343	2182.8
3	1746	1686.6	15	2346	2209.5
4	1650	1644.9	16	2352	2231.7
5	1623	1632.9	17	2367	2257.8
6	1611	1622.1	18	2394	2284.2
7	1602	1652.7	19	2430	2286
8	1668	1719.6	20	2430	2286.6
9	1803	1858.5	21	2397	2267.7
10	1980	2007.3	22	2364	2267.7
11	2151	2106.3	23	2337	2213.4

Table 5.11: Solar power on day 1.

Hour	P_{PV}	$P_{PV,est}$	*Hour*	P_{PV}	$P_{PV,est}$
00	0	8.05	12	756.2	864.7
01	0	15.9	13	809.5	844.8
02	0	17.4	14	760.3	669.1
03	0	17.4	15	472.5	403.5
04	0	26.0	16	308.1	260.4
05	0	49.7	17	45.1	19.9
06	0	21.2	18	0	31.4
07	0	72.9	19	0	18.8
08	8.1	61.6	20	0	2.1
09	114.9	224.3	21	0	13.1
10	291.8	510.7	22	0	22.7
11	406.8	733.6	23	0	37.9

Table 5.12: Solar power on day 2.

Hour	P_{PV}	$P_{PV,est}$	*Hour*	P_{PV}	$P_{PV,est}$
00	0	6.9	12	1896.7	1507.4
01	0	48.3	13	1779.1	1342.2
02	0	27.6	14	1536.0	1024.4
03	0	3.9	15	1187.5	571.3
04	0	12.6	16	769.9	368.7
05	20.1	3.2	17	243.1	124.7
06	311.0	282.1	18	16.3	27.4
07	747.3	596.5	19	0	32.5
08	1162.3	919.9	20	0	38.3
09	1512.4	1254.5	21	0	30.3
10	1758.9	1415.6	22	0	4.2
11	1896.7	1471.9	23	0	40.5

Table 5.13: Solar power on day 3.

Hour	P_{PV}	$P_{PV,est}$	*Hour*	P_{PV}	$P_{PV,est}$
00	0	27.7	12	905.2	580.9
01	0	34.9	13	800.6	551.6
02	0	5.2	14	579.3	394.6
03	0	8.2	15	257.5	206.1
04	0	13.6	16	12.0	58.9
05	0	10.5	17	0	69.8
06	0	40.3	18	0	32.8
07	48.2	15.6	19	0	1.0
08	337.9	309.7	20	0	17.1
09	595.4	466.7	21	0	26.1
10	792.4	577.8	22	0	8.7
11	897.1	651.3	23	0	54.8

Table 5.14: Solar power on day 4.

Hour	P_{PV}	$P_{PV,est}$	*Hour*	P_{PV}	$P_{PV,est}$
00	0	7.2	12	2039.7	1981.3
01	0	9.5	13	2027.7	1987.8
02	0	7.4	14	1910.8	1814.4
03	0	16.9	15	1677.6	1540.8
04	0	16.2	16	1408.0	1282.4
05	12	50.6	17	933.3	978.4
06	229.2	245.8	18	667.9	550.2
07	603.3	643.9	19	257.5	324.5
08	997.6	997.8	20	16.0	13.7
09	1362.9	1352.8	21	0	24.6
10	1667.2	1644.4	22	0	11.6
11	1894.8	1836.8	23	0	38.8

Table 5.15: Wind power on day 1.

Hour	P_W	$P_{W,est}$	*Hour*	P_W	$P_{W,est}$
00	321.6	1018.0	12	597.6	1282.4
01	398.4	1091.6	13	367.2	1229.1
02	158.4	1019.8	14	1353.6	1265.1
03	348	1000.0	15	1236	1339.2
04	230.4	1077.0	16	1317.6	930.6
05	254.4	994.3	17	885.6	1085.3
06	276	1021.6	18	1005.6	830.1
07	278.4	930.0	19	1017.6	729.9
08	256.8	1048.3	20	984.0	845.9
09	444	1020.1	21	873.6	853.2
10	530.4	1244.3	22	715.2	990.8
11	429.6	1295.7	23	439.2	1016.7

Table 5.16: Wind power on day 2.

Hour	P_W	$P_{W,est}$	*Hour*	P_W	$P_{W,est}$
00	417.6	814.6	12	1500	1500
01	528.0	781.2	13	1500	1500
02	631.2	701.4	14	1500	1500
03	537.6	766.7	15	1500	1500
04	477.6	687.6	16	1500	1500
05	280.8	720.8	17	1024.8	1359.8
06	660.0	745.0	18	1260	1121.2
07	789.6	932.6	19	537.6	1218.3
08	662.4	1008.9	20	669.6	1450.5
09	1500	1500	21	609.6	1107.7
10	1500	1500	22	705.6	906.3
11	1500	1500	23	607.2	532.6

Table 5.17: Wind power on day 3.

Hour	P_W	$P_{W,est}$	*Hour*	P_W	$P_{W,est}$
00	285.6	684.7	12	434.4	1128.2
01	218.4	765.4	13	703.2	1198.4
02	235.2	601.9	14	765.6	994.6
03	192	659.5	15	379.2	926.0
04	160.8	563.0	16	429.6	873.7
05	237.6	936.9	17	420	968.5
06	396	901.6	18	285.6	806.7
07	247.2	450.7	19	369.6	1059.6
08	520.8	744.4	20	240	940.4
09	362.4	709.7	21	501.6	991.4
10	792	731.9	22	244.8	1152.3
11	835.2	1105.6	23	391.2	971.3

Table 5.18: Wind power on day 4.

Hour	P_W	$P_{W,est}$	*Hour*	P_W	$P_{W,est}$
00	372	590.2	12	633.6	680.4
01	412.8	564.1	13	825.6	691.2
02	285.6	638.2	14	1279.2	1133.2
03	189.6	514.5	15	902.4	619.3
04	187.2	516.1	16	662.4	996.8
05	264	592.7	17	921.6	1031.7
06	340.8	509.9	18	936	1270.7
07	573.6	566.7	19	712.8	1087.7
08	504	629.9	20	571.2	1213.5
09	283.2	846.6	21	679.2	1400.3
10	499.2	954.5	22	727.2	1218.1
11	813.6	1093.2	23	679.2	659.6

In addition, the spot prices for the four days are derived in a similar way as was assumed in Chapter 2.

Table 5.19: Spot electricity prices for day 1.

Hour	*Price (cent/kWh)*	*Hour*	*Price (cent/kWh)*
00	8.8	12	14.9
01	8.3	13	14.2
02	8.2	14	28.9
03	7.9	15	33.2
04	8.0	16	35.1
05	8.2	17	33.2
06	8.8	18	28.1
07	9.3	19	25.1
08	11.4	20	23.3
09	14.6	21	21.3
10	17.1	22	14.6
11	15.3	23	11.4

Table 5.20: Spot electricity prices for day 2.

Hour	*Price (cent/kWh)*	*Hour*	*Price (cent/kWh)*
00	8.8	12	19.1
01	8.3	13	22.2
02	8.2	14	25.9
03	7.9	15	33.2
04	8	16	35.1
05	10.5	17	33.2
06	14.8	18	28.1
07	18.3	19	25.1
08	22.4	20	22.3
09	21.6	21	18.3
10	20.1	22	14.6
11	19.3	23	11.4

Table 5.21: Spot electricity prices for day 3.

Hour	*Price (cent/kWh)*	*Hour*	*Price (cent/kWh)*
00	9.1	12	19.1
01	8.6	13	19.5
02	8.2	14	19.9
03	8.1	15	21.2
04	8	16	25.1
05	8.5	17	27.2
06	11.1	18	28.1
07	15.2	19	24.1
08	18.4	20	20.3
09	20.6	21	17.3
10	20.1	22	14.6
11	19.3	23	11.4

Table 5.22: Spot electricity prices for day 4.

Hour	*Price (cent/kWh)*	*Hour*	*Price (cent/kWh)*
00	7.8	12	19.1
01	7.3	13	23.2
02	7.1	14	26.9
03	7.9	15	31.2
04	8	16	32.1
05	9.5	17	32.2
06	13.2	18	26.1
07	17.3	19	24.1
08	20.4	20	20.3
09	20.6	21	17.3
10	20.1	22	14.6
11	19.3	23	11.4

Lastly, the minimum return to initiate a discharge cycle is listed in Table 5.23 for the four days [calculated using Equation (2.15)]. Note that the calculated values are almost the same because it is assumed that the battery has the same SOH (or discharge capacity) for the four days. The values of R_{min} are calculated on a daily basis in the scheduling operation.

Table 5.23: Minimum Return to initiate a discharge cycle.

	R_{min}
Day 1	$ 0.328
Day 2	$ 0.325
Day 3	$ 0.326
Day 4	$ 0.324

5.5.2 Assumptions

The following assumptions were made in the simulation:

1. The energy storage has an initial SOC of 0.3 on the first day.
2. An accurate SOC and SOH are obtained.
3. $I_{const} \cdot \Delta t = C/8$ (equivalent to 1.25 kWh).
4. Actual spot prices are the same as the forecasted prices.
5. The battery is new (normalized discharge capacity D is 1).
6. Charging (with CC) is terminated if a SOC of 0.8 is reached and discharging is terminated if a SOC of 0.3 is reached under any circumstances.
7. Charging from the grid utility is performed at $C/4$ rate.
8. Discharging and charging efficiencies are 100%.
9. The minimum and maximum spot prices SP_{min} and SP_{max} are constant and derived from Chapter 2:

   SP_{min} = 0.09 \$/kWh

   SP_{max} = 0.29 \$/kWh
10. The normalized cycle-life per dollar of capital cost (L_N) equals to 1.67 (derived from Chapter 2 and scaled down for a 10 kWh storage system)
11. All power losses are neglected.

5.5.3 Results

The simulation results for the load and DG power for the four days are shown in Figures 5.15 and 5.16.

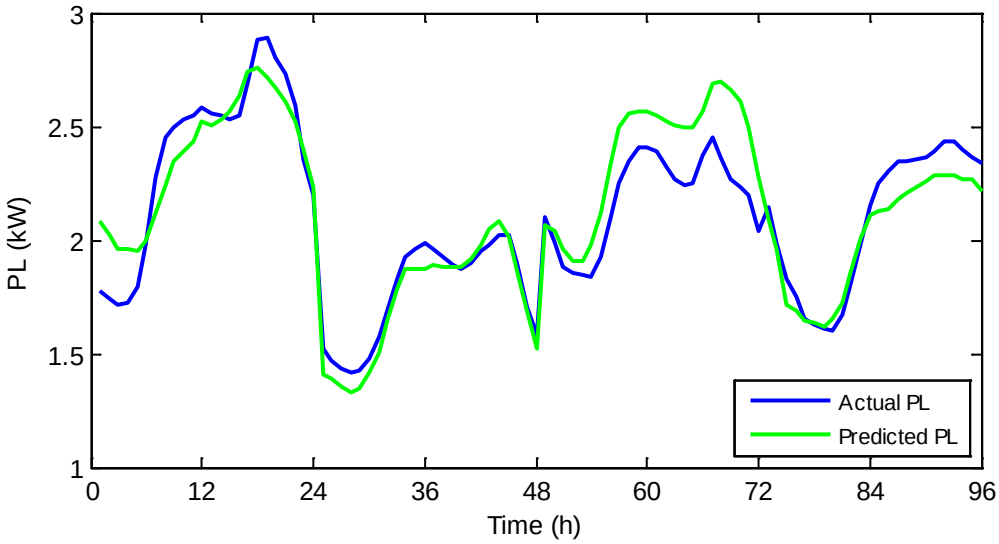

Figure 5.15: Actual and predicted load power (P_L).

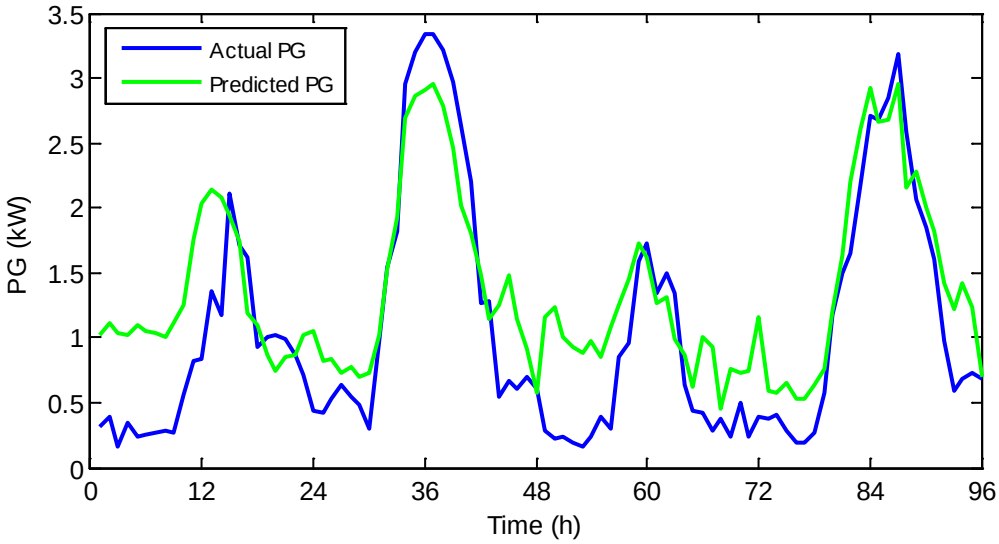

Figure 5.16: Actual and predicted distributed generated power (P_G).

The hourly spot prices for the four days (logically assumed) are shown in Fig. 5.17.

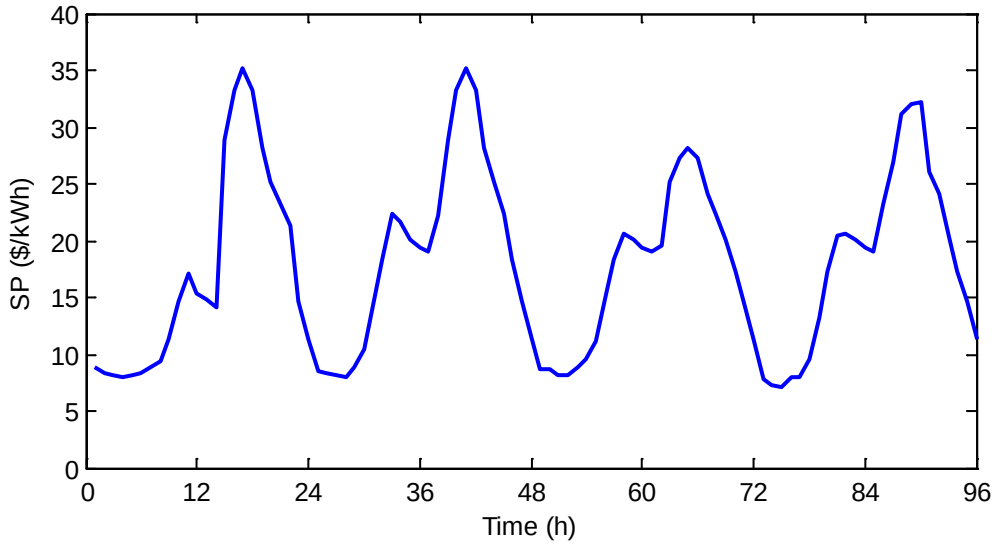

Figure 5.17: Spot market electricity prices (*SP*).

The real-time operation of the MSS in terms of its SOC for the four days is shown in Figure 5.18.

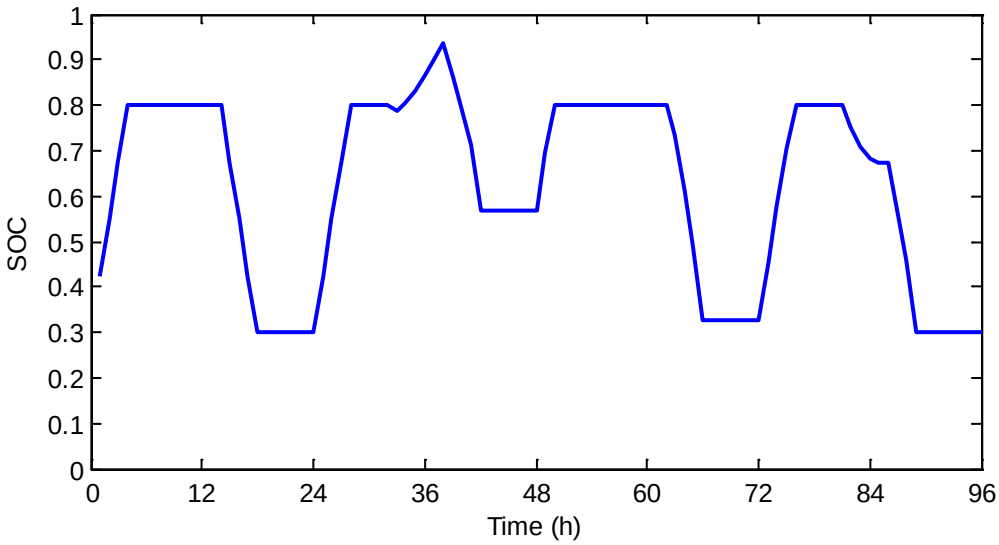

Figure 5.18: Online operation of the MSS.

The return calculated for the four days is shown in Figure 5.19 (hourly return) and Figure 5.20 (total return). Obviously, the return in Figure 5.19 is much higher than R_{min} (with a MSS and DG system) and is slightly above R_{min} for a MSS system only.

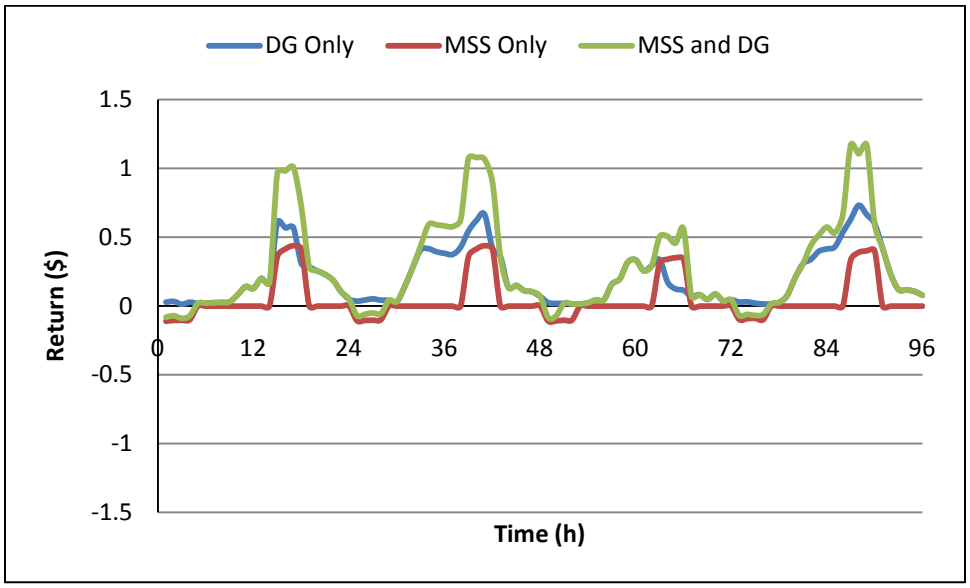

Figure 5.19: Hourly return for different distributed systems.

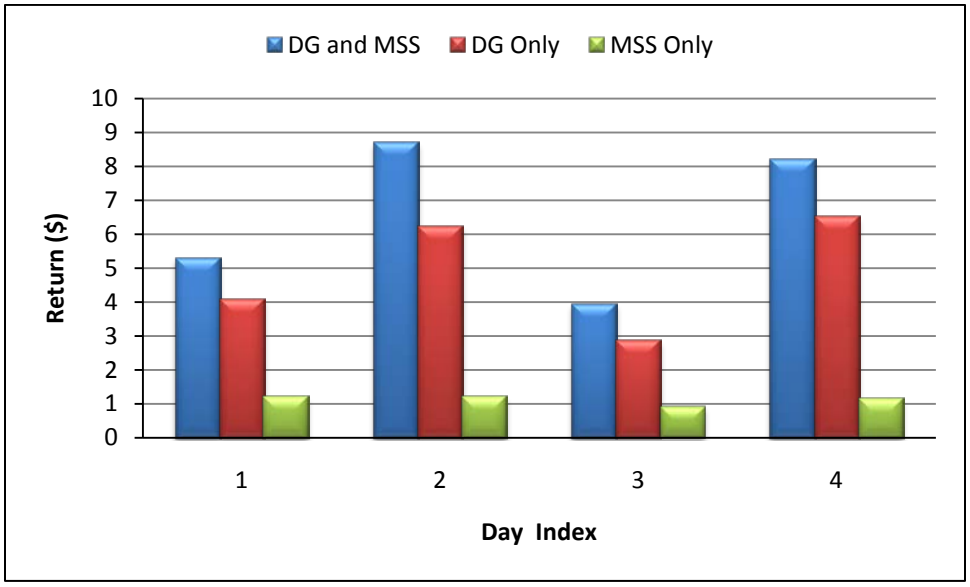

Figure 5.20: Average daily revenue for different distributed systems.

5.5.4 Summary

It was shown that the integration of DGs and the MSS is beneficial. In fact, the return can be dramatically increased when the MSS and DGs are combined. The reasons for that are as follows:

1. The storage can absorb any excess power above the load (excess power is wasted in case of DGs only).
2. The storage allows transacting power with the grid with and without DGs since it overcomes the forecasting errors, which cannot be achieved with DG only.
3. The MSS can further maximize the return by storing excess DG power at low-demand hours and transacting this power back at high-demand hours.

Table 5.23 summarizes some of the features of the three types of distributed systems.

Table 5.24: Comparison between distributed systems.

	Peak Shaving	*Energy Bidding*	*Daily Return*
DG Only	Not guaranteed	Problematic	High (assuming high P_G)
MSS Only	Guaranteed	Possible	Low (compared to "DG only" assuming one cycle per day)
DG and MSS	Guaranteed	Possible	Very high

The system size that was chosen for the simulation can accommodate a typical residential application. However, the system size may vary according to the application. Regardless what the MSS is designed for, the MSS must be sized properly. This includes the system size compared to the DGs sizes, the energy storage size, the power converter (charger/inverter) size, as well as the load size. Also, appropriate DOD and SOC cutoffs must be chosen properly to overcome forecasts uncertainty and thus improve scheduling accuracy.

5.6 Conclusions

The forecasting models proposed in this chapter showed acceptable results for the load power and solar radiation models where the correlation was around 0.95 (day-ahead), while for the wind speed and direction models the correlation was below 0.5 (day-ahead) which is quite low. Nonetheless, the purpose in this chapter is to show how the EMS operates which was achieved via simulation. The accuracy of the wind speed and direction forecasting models can be improved by improving the ANN structure and/or modifying the inputs of the models.

It was shown that the SOC must be kept within certain limits to allow the storage to supply or sink any unexpected deficit or surplus in the DG power due to forecasting uncertainties. The SOC cutoffs and the DOD must be all designed in such a way to ensure an exact matching between the forecasted and actual exchange plan.

It is critical, however, to properly size the MSS according to the DG size. It is advantageous to oversize the storage device with respect to the DG size in order to maximize the profit especially when the uncertainties in the weather conditions are high.

It was noticed that as far as the forecasting accuracy increases, the expected return increases accordingly. Thus, the return can be maximized through either improving the forecasting accuracy (to avoid penalties), which is beyond the scope of this dissertation, or optimizing the MSS control and design, which was intensively illustrated in this chapter and in the preceding chapters.

CHAPTER SIX: CONCLUSIONS AND FUTURE WORK

6.1 Summary and Conclusions

Energy storage is a key element in the success of the future smart grid infrastructure since it can be perfectly utilized to reshape today's electricity market. The current electric power generation and transmission system, which has not changed since more than a hundred years, can meet today's-but not future's-demand. Hence, energy storage and distributed renewable energy sources must be adopted at different levels (utilities, industrial, commercial, residential, etc.) to contribute in the success of the smart grid and thus avoid expanding the current power system. In fact, the adoption of distributed generation sources and storage systems by any electricity consumers, regardless what category the consumer is from, can help moving forward. To achieve that, there are some challenges that must be overcome such as reducing the costs of distributed generation/storage systems, which is currently under intensive research, as well as other associated challenges including technical, legislative and social challenges.

Chapter 2 of this dissertation introduced some design considerations for micro-storage systems. It was shown that an AC-coupled architecture is advantageous compared to DC-coupled and inline architectures since it allows a flexible, robust and modular design. Also, some design issues for the power converter were presented. The power converter must meet some technical specifications to insure safe operation and to sustain a high-quality supplied power to the grid to avoid grid issues. Furthermore, a residential case study was discussed to show how the system size (including the energy storage and converter) is derived. Other issues that were covered in this chapter include some energy storage technologies and communications as well as some economic

analyses. Each topic in this chapter, which can indeed be a subject of an entire dissertation, was introduced briefly. The objective of the chapter as a whole was to show how the design of such MSS can be optimized.

In Chapter 3, charge-control algorithms for lithium and nickel batteries were presented. This chapter introduced various concepts related to battery chargers. It presented some charging algorithms for single chemistry and others for multichemistry battery chargers. Some charging methods including constant-current constant-voltage (CC/CV), interrupted charge control (ICC) and pulse charging were introduced. Furthermore, other issues that must be handled by any BMS including temperature control, battery type identification (in case of multichemistry chargers), charge termination and SOC estimation were all discussed. The discussion in this chapter was comprehensive and was achieved by introducing, comparing and evaluating some recent developed charging algorithms for lithium and nickel battery chargers, which can accommodate a wide range of applications. The evaluation in this chapter was achieved through analyzing experimental charging profiles for NiCd, NiMH and Li-ion battery cells.

Chapter 4 proposed advanced techniques to enhance the performance of the BMS. A proper charge-control mechanism that insures a reliable charging operation without sacrificing the battery lifetime is extremely important. Thus, advanced techniques can be used alongside with the charge-control algorithms to closely monitor the battery. In this chapter, a battery model that employs the concept of equivalent circuit, with some parameters added, to interpret the battery behavior was proposed. This model showed very accurate results. The parameters were found first at room temperature and then at other temperatures from -30^{o} C to 50^{o} C in increments of 10^{o} C. It was shown that the model parameters are strongly affected by the temperature. To validate the

model at all temperatures, the parameters of the model can be calculated at different temperatures and stored in a lookup table. The proposed model was used to estimate the inner states of the battery including the SOC and SOH, which cannot be achieved without implementing a battery model. The SOC is important to estimate in real-time to insure that the battery does not exceed a lower or an upper cut-off limit. Also, the SOC estimation is beneficial when exchanging power with the utility grid to calculate the amount of power that can be delivered to the grid. The SOH estimation is important to estimate the battery remaining life and to calculate the expected return when exchanging power with the utility grid. Both the SOC and SOH were estimated using EKFs for two reasons; they allow implementation in real-time; and they always converge to the true value. The results of the EKFs' algorithms can be used to further estimate the battery parameters along the battery lifespan.

In Chapter 5, an EMS was proposed with the objective to control the operation of the MSS in a spot electricity market system with and without the existence of renewable energy sources. In the first case, when only a MSS exists, the operation is straightforward; that is, once the spot electricity prices are received, the power exchange plan is scheduled to maximize the economic return. In the other case, when renewable energy sources exist, the power exchange plan is also scheduled to maximize the economic return, but this cannot be achieved straightforward. Due to the nature of renewable energy sources such as solar and wind, which is strongly affected by the weather conditions, an EMS must employ forecasting models to predict the amount of power that can be generated from these sources to schedule an operation with the spot electricity market. In addition to predicting the power generated from renewable DGs, the EMS must also predict the amount of the local load (if it exists) all for the same time horizon. ANNs were employed in this

chapter to develop weather and load forecasting models to manage the operation of a MSS when operated alongside with solar and wind power plants feeding a residential property.

6.2 Future Work

In addition to the results obtained throughout this work, still, many related-areas were not investigated. Some of these areas include:

1. The design of a management system for technologies other than nickel and lithium batteries. For example, sodium-sulfur and zinc bromine batteries as well as supercapacitors can be considered.
2. Extending the design of the BMS at all possible temperatures by enforcing the battery model to capture all the battery dynamics at any temperature regardless the battery condition (age). These two effects-temperature and aging-were briefly presented in this dissertation.
3. Improving the design of the forecasting models especially the wind speed and direction models.
4. Developing an operation strategy to operate the MSS by controlling the charging operation based on the weather conditions and load demand (DG and load power forecasts), which can be very beneficial if fairly accurate load and weather forecasting models were available.
5. Improving the EMS to further increase the economic return.

REFERENCES

[1] U.S. Energy Information Administration (EIA) website: http://www.eia.gov/oiaf/ieo/world.html.

[2] Exploring the Imperative of Revitalizing America's Electric Infrastructure, U.S. DOE: http://www.oe.energy.gov/DocumentsandMedia/DOE_SG_Book_Single_Pages(1).pdf

[3] Homepage of International Energy Agency-Photovoltaic Power Systems Programme: http://www.iea-pvps.org/.

[4] Homepage of the Global Wind Energy Council: http://www.gwec.net/.

[5] Vallvé X., Graillot A., Gual S and Colin, H "Micro storage and Demand Side Management in distributed PV grid-connected installations", *9th International Conference on Electrical Power Quality and Utilization*, pp. 1-6, 2007.

[6] R. H. Lasseter and P. Paigi "Microgrid: A Conceptual Solution", *35th IEEE PESC*, pp. 4285-4290, 2004.

[7] A. Hussein, S. Harb, N. Kutkut, J. Shen and I. Batarseh "Design Considerations for Micro Storage Systems in Residential Applications", *32nd IEEE INTELEC*, pp. 1-6, 2010.

[8] Homepage of Nordic power market: http://www.nordpoolspot.com/PowerMaket/.

[9] Homepage of wind-works.org: http://www.wind-works.org/.

[10] "Benefits of Demand Response in Electricity Markets and Recommendations for achieving them", U.S. DOE Report, 2006.

[11] W. I. Bower and J. C. Wiles, "Analysis of Grounded and Ungrounded Photovoltaic Systems", *1st WCPEC*, pp. 809-812, 1994.

[12] Y. Xue, L. Chang, S. B. Kjær, J. Bordonau and T. Shimizu "Topologies of Single-Phase Inverters for Small Distributed Power Generators: An Overview", *IEEE Trans. Power Electronics*, vol. 19, no. 5, pp. 1305-1314, 2004.

[13] 1547 IEEE Standard for Interconnecting Distributed Resources with Electric Power Systems.

[14] G. Hegde, P. Pullammanappallil and C. Nayar, “Modular AC Coupled Hybrid Power Systems for the Emerging GHG Mitigation Products Market”, *TENCON*, pp. 971-975, 2003.

[15] T. Kerekes, R. Teodorescu, P. Rodriguez, G. Vazquez and E. Aldabas “A New High-efficiency Single-phase Transformerless PV Inverter Topology”, *IEEE Trans. Industrial Electronics*, vol. 58, no. 1, pp. 184-191, 2011.

[16] Q. Li and P. Wolfs “A Review of the Single Phase Photvoltaic Module Integrated Converter Topologies with Three Different DC Link Configurations”, *IEEE Trans. Power Electronics*, vol. 23, no. 3, pp. 1320-1333, 2008.

[17] D. S. Parker, M. D. Mazzara and J. R. Sherwin “Monitored Energy Use Patterns In Low-Income Housing In A Hot And Humid Climate”, Florida Solar Energy Center (FSEC): http://www.fsec.ucf.edu/en/publications/html/fsec-pf-300-96/.

[18] U.S. Average Monthly Bill by Sector, U.S. Energy Information Administration (EIA): www.eia.doe.gov/cneaf/electricity/esr/table5.xls.

[19] ComEd website: http://www.comed.com/.

[20] CAISO website: http://www.caiso.com/.

[21] Maxwell Corp. datasheets: http://www.maxwell.com/.

[22] JM Energy Corp. datasheets: www.jmenergy.co.jp/en/.

[23] D. T. Ton, C. J. Hanley, G. H. Peek and J. D. Boyes “Solar Energy Grid Integration Systems-Energy Storage (SEGIS-ES)”: http://www1.eere.energy.gov/solar/pdfs/segis-es_concept_paper.pdf/.

[24] D. Rastler “Overview of Electric Energy Storage Systems”: http://dodfuelcell.cecer.army.mil/rd/NZE_Workshop/2_Rastler.pdf.

[25] K. C. Divya and J. Østergaard “Battery Energy Storage Technology for Power Systems—An Overview”, Electric Power Systems Research, vol. 79, no. 4, pp. 511-520, 2009.

[26] Seizing the Value of Energy Storage for Renewable Energy Integration; webinar presented by “INFOCAST”, June 23rd 2010.

[27] Standard Electric Price Plans (Summer-peak E21 plan prices): http://www.srpnet.com/prices/pdfx/Standard_Electric_Price_Plans_05012010.pdf/.

[28] Homepage of "Battery University": www.batteryuniversity.com/.

[29] Homepage of "Battery and Energy Technologies": www.mpoweruk.com/.

[30] R. C. Cope and Y. Podrazhansky "The Art of Battery Charging", *14th Battery Conference on Applications and Advances*, pp. 233-235, 1999.

[31] J. Nicolai and L. Wuidart "From Nickel-Cadmium to Nickel-Metal-Hydride Fast Battery Charger", STMicroelectronics Inc. Application Note: http://www.st.com/stonline/books/pdf/docs/2074.pdf/.

[32] T. Mundra and A. Kumar "An Innovative Battery Charger for Safe Charging of NiMH/NiCd Batteries", *IEEE Trans. Consumer Electronics*, vol. 53, no. 3, pp. 1044-1052, 2007.

[33] F. Boico, B. Lehman and K. Shujaee, "Solar Battery Chargers for NiMH Batteries", *IEEE Trans. Power Electronics*, vol. 22, No. 5, pp. 1600-1609, 2007.

[34] M. Gonzdez, F. Ferrero, J. Antbn and M. Pkez "Considerations to Improve the Practical Design of Universal and Full-Effective NiCd/NiMH Battery Fast Chargers", *14th IEEE APEC'99*, pp. 167-173, 1999.

[35] J. Díaz, J. Martín-Ramos, A. Pernía, F. Nuño and F. Linera "Intelligent and Universal Fast Charger for NiCd and NiMH Batteries in Portable Applications", *IEEE Trans. Industrial Electronics*, vol. 51, no. 4, pp. 857-863, 2004.

[36] Panasonic Lithium-Ion Charging Datasheet (Jan. 2007): http://www.panasonic.com/industrial/includes/pdf/Panasonic_LiIon_Charging.pdf/.

[37] M. Elias, K. Nor and A. Arof "Design of Smart Charger for Series for Lithium-Ion Batteries", *PEDS'05*, pp. 1485-1490, 2005.

[38] M. Bhatt, W. Hurley and W. Wölfle "A New Approach to Intermittent Charging of Valve-Regulated Lead-Acid Batteries in Standby Applications", *IEEE Trans. on Industrial Electronics*, vol. 52, no. 5, pp. 1337-1342, 2005.

[39] A. Hussein, M. Pepper, A. Harb and I. Batarseh "An Efficient Solar Charging Algorithm for Different Battery Chemistries", *5th IEEE VPPC'09*, pp. 188-193, 2009.

[40] H. Barth, C. Schaeper, T. Schmidla, H. Nordmann, M. Kiel, H. van der Broeck, Y. Yurdagel, C. Wieczorek, F. Hecht and D. U. Sauer, "Development of a Universal Adaptive Battery Charger as an Educational Project", *IEEE Future Energy Challenge*, pp. 1839-1845, 2008.

[41] S. Park, H. Miwa, B. Clark, D. Ditzler, G. Malone, N. D'souza and J. Lai, "A Universal Battery Charging Algorithm for Ni-Cd, Ni-MH, SLA, and Li-Ion for Wide RangeVoltage in Portable Applications", *IEEE Future Energy Challenge*, pp. 4689-4694, 2008.

[42] F. Lima, J. Ramalho, D. Tavares, J. Duarte, C. Albuquerque, T. Marques, A. Geraldes, A. Casimiro, G. Renkema, J. Been and W. Groeneveld "A Novel Universal Battery Charger for NiCd, NiMH, Li-Ion and Li-Polymer", *ESSCIRC '03*, pp. 209-212, 2003.

[43] S. Moore and P. Schneider "A Review of Cell Equalization Methods for Lithium Ion and Lithium Polymer Battery Systems", Delphi Automotive Systems: http://www.americansolarchallenge.org /tech/resources/SAE_2001-01-0959.pdf/.

[44] W. B. Gu and C. Y. Wang "Thermal-Electrochemical Modeling of Battery Systems", *Journal of The Electrochemical Society*, vol. 147, no. 8, pp. 2910-2922, 2000.

[45] Y.H. Kim and H.D. Ha "Design of Interface Circuits with Electrical Battery Models", *IEEE Trans. Industrial Electronics*, vol. 44, no. 1, pp. 81-86, 1997.

[46] I.S. Kim "A Technique for Estimating the State of Health of Lithium Batteries Through a Dual-Sliding-Mode Observer", *IEEE Trans. Power Electronics*, vol. 25, no. 4, pp. 1013-1022, 2010.

[47] A. Vasebi, M. Partovibakhsh and S. M. T. Bathaee "A novel combined battery model for state-of-charge estimation in lead-acid batteries based on extended Kalman filter for hybrid electric vehicle applications", *Journal of Power Sources*, vol. 174, no. 1, pp. 30-40, 2007.

[48] S. Abu-Sharkh and D. Doerffel "Rapid test and non-linear model characterization of solid-state lithium-ion batteries", *Journal of Power Sources*, vol. 130, no. 1-2, pp. 266-274, 2004.

[49] S. Lee, J. Kim, J. Lee and B.H. Cho "State-of-charge and capacity estimation of lithium-ion battery using a new open-circuit voltage versus state-of-charge", *Journal of Power Sources*, vol. 185, no. 2, pp. 1367-1373, 2008.

[50] Z. Salameh, M. Casacca and W. Lynch "A Mathematical Model for Lead-Acid Batteries", *IEEE Trans. Energy Conversion*, vol. 7, no. 1, pp. 93-98, 1992.

[51] J. Zhang, S. Ci, H. Sharif and M. Alahmad "An Enhanced Circuit-Based Model for Single-Cell Battery", *25th IEEE APEC*, pp. 672-675, 2010.

[52] G. L. Plett "Extended Kalman filtering for battery management systems of LiPB-based HEV battery packs Part 2. Modeling and identification", *Journal of Power Sources*, vol. 134, no. 2, pp. 262-276, 2004.

[53] ThermoAnalyticsInc."Battery Modeling":www.thermoanalytics.com/docs/batteries.html/.

[54] N. Chaturvedi, R. Klein, J. Christensen, J. Ahmed and and A. Kojic "Algorithms for Advanced Battery Management Systems", *IEEE Control Systems Magazine*, June 2010.

[55] G. L. Plett "Extended Kalman filtering for battery management systems of LiPB-based HEV battery packs", parts 1and 3, Journal of Power Sources, vol. 134, no. 2, pp. 252-292, 2004.

[56] G. L. Plett "Results of Temperature-Dependent LiPB Cell Modeling for HEV SOC Estimation", *CD-ROM Proceedings of the 21st Electric Vehicle Symposium* (*EVS21*), 2005.

[57] G. L. Plett "Dual and Joint EKF for Simultaneous SOC and SOH Estimation", *CD-ROM Proceedings of the 21st Electric Vehicle Symposium* (*EVS21*), 2005.

[58] S. Piller, M. Perrin and A. Jossen "Methods for state-of-charge determination and their applications", *Journal of Power Sources*, vol. 96, no. 1, pp. 113-120, 2001.

[59] D. J. Simon "Optimal State Estimation", 1st edition, pp. 407-409, 2006.

[60] S. Haykin "Neural Networks and Learning Machines", 3rd edition, pp. 1-46, 1999.

[61] M. Korpaas, A. T. Holen and R. Hildrum "Operation and sizing of energy storage for wind power plants in a market system", *Electrical Power and Energy Systems*, vol. 25, no. 8, pp. 599-606, 2003.

[62] Homepage of ISO New England: http://www.iso-ne.com/.

[63] Homepage of AgriMet-The Pacific Northwest Cooperative Agricultural Weather Network: http://www.usbr.gov/pn/agrimet/.

[64] A. Hussein and I. Batarseh "A Review of Charging Algorithms for Nickel and Lithium Battery Chargers", *IEEE Trans. Vehicular Technology*, vol. 60, no. 3, pp. 830-838, 2011.

[65] A. Hussein and I. Batarseh "An Overview of Generic Battery Models", *IEEE Power and Energy Society* (*PES*) *General Meeting*, 2011 (*In Press*).

[66] A. Hussein and I. Batarseh "State-of-Charge Estimation for a Single Lithium Battery Cell Using Extended Kalman Filter", *IEEE Power and Energy Society* (*PES*) *General Meeting*, 2011 (*In Press*).

[67] A. Hussein, N. Kutkut and I. Batarseh "A Hysteresis Model for a Lithium Battery Cell with Improved Transient Response", *IEEE 26th APEC*, pp. 1790-1794, 2011.